Compact XUV and X-Ray sources from laser-plasma interactions: theoretical and numerical study

Dissertation

zur Erlangung des akademischen Grades
doctor rerum naturalium (Dr. rer. nat.)

seit 1558

vorgelegt dem Rat der Physikalisch-Astronomischen Fakultät der Friedrich-Schiller-Universität Jena

von M. Sc. Stefan Tietze
geboren am 15.12.1989 in Osterode am Harz

Gutachter

1. Prof. Dr. Matt Zepf
   Friedrich-Schiller-Universität Jena
   Institut für Optik und Quantenelektronik

2. Prof. Dr. Brendan Dromey
   Queen's University Belfast
   School of Mathematics and Physics

3. Prof. Dr. Stefan Karsch
   Ludwig-Maximilians-Universität München
   Fakultät für Physik

Datum der Disputation: 04.11.2021

Zusammenfassung

Diese Arbeit befasst sich mit der Erzeugung hoher Harmonischer durch Reflexion eines ultrakurzen und hochintensiven Laserpulses von einem Plasma mit überkritischer Dichte. Durch dieses Verfahren, genannt Surface High Harmonic Generation (SHHG), wird es möglich, kompakte Quellen für kohärente Strahlung im Bereich des extremen Ultravioletten (XUV) und für Röntgenstrahlung zu entwickeln. Die Ergebnisse in dieser Arbeit werden vorwiegend durch ein- und zweidimensionale Particle-In-Cell (PIC) Computersimulationen gewonnen, die durch analytische Modelle überprüft werden.

Das Hauptaugenmerk in dieser Dissertation liegt auf der Erzeugung isolierter Pulse und der Steigerung der Erzeugungseffizienz, die einige der wichtigsten Herausforderungen der SHHG darstellen. Es wird gezeigt, dass von einem aus mehreren Zyklen bestehenden einfallenden Puls ein einzelner Attosekundenpuls (AP) erzeugt werden kann, wenn die Phase zwischen der Trägerfrequenz und der Einhüllenden in Abhängigkeit der Dichte und des Dichtegradienten richtig gewählt wurde. Ein analytisches Modell liefert die Interpretation der Ergebnisse der PIC-Simulationen.

Die räumliche Separation von AP kann durch den Attosecond Lighthouse Effect erreicht werden. Zu stark ausgeprägte Eindellungen der Plasmaoberfläche können diesen Effekt jedoch zunichte machen. Mithilfe von PIC-Simulationen wird ein experimentelles Resultat erklärt, wo dies der Fall war. Weiterhin wird gezeigt, dass der räumliche spektrale Chirp mit der Tiefe der Eindellung zusammenhängt.

Die Effizienz von SHHG kann stark gesteigert werden, wenn man den Laserpuls nach der Reflexion von der ersten Plasmaoberfläche auf ein zweites Plasma lenkt. Für die Effizienz ist die relative Phase zwischen den Harmonischen auf der Oberfläche des zweiten Plasmas entscheidend. Diese relative Phase verändert sich selbst bei der Ausbreitung im Freiraum durch die Gouy-Phase. Um den Effizienzgewinn zu maximieren, wurde eine Parameterstudie mithilfe von PIC-Simulationen durchgeführt, um die optimale Distanz zwischen den beiden Plasmen zu finden.

Abstract

In this thesis the generation of high order harmonics of ultrashort and high intensity laser pulses from solid density plasmas, so called surface high harmonic generation (SHHG), is studied. With SHHG, a compact source of coherent XUV and X-Ray radiation becomes possible. The results are obtained numerically using 1D and 2D Particle-In-Cell (PIC) computer simulations, which are supported by analytical models.

This work focusses on two main issues of SHHG to date, pulse isolation and generation efficiency. It is shown that a single attosecond pulse (AP) can be obtained from a few-cycle incident laser pulse by choosing a suitable carrier-envelope phase (CEP), depending on the density and shape of density gradient of the target. An analytical model providing an interpretation of the results obtained from PIC simulations is presented.

Spatial isolation of APs can be achieved using the attosecond lighthouse effect, but surface denting is detrimental to the separation of APs. PIC simulations are used to explain an experimental result, where a separation of pulses was not possible due to surface denting. Furthermore it is shown that the angular spectral chirp corresponds to the depth of the surface denting.

The efficiency of SHHG can be enhanced greatly by reflecting the beam coming from a first target off a second target. Of major importance for the efficiency is the relative phase between harmonics on the surface of the second target. The relative phase changes even when propagating in free space due to the Gouy phase. To maximize the efficiency gain, a parametric study using PIC simulations has been performed to find the optimal distance between two targets.

Contents

1. Introduction **3**

2. Theoretical Background **7**

2.1. Basics of plasma physics 7

2.2. Particle-In-Cell (PIC) simulations 8

2.2.1. The PIC algorithm 9

2.2.2. Experimental Data and PIC simulations 11

2.2.3. Effect of numerical dispersion on SHHG simulations 13

2.3. Gaussian Pulses 16

2.4. Gouy Phase 16

2.5. Spatio-Temporal Couplings (STC) 18

2.6. Single Particle Motion in a relativistic Laser Pulse 20

2.7. High Harmonic Generation from solid targets 23

2.7.1. Coherent Wake Emission (CWE) 24

2.7.2. Relativistic Oscillating Mirror (ROM) 25

2.7.3. Surface Denting 27

2.7.4. Gating of Single Attosecond Pulses 34

3. Density and Scalelength Dependent Carrier-Envelope Phase Effects in Attosecond Pulse Generation **37**

3.1. Sub-relativistic case 38

3.2. Relativistic case 42

3.3. Ultra-relativistic case 44

3.4. Consequences for SHHG with few-cycle laser pulses 46

3.4.1. Preplasma 47

3.5. Conclusions 48

4. Angular streaking of an attosecond pulse train **51**

4.1. PIC simulations of the Attosecond Lighthouse 51

4.2. Spectral Properties of the Attosecond Lighthouse 55
4.3. Angular Streaking 56
4.4. Conclusions 60

5. Efficiency enhancements and propagation effects in multipass high harmonic generation 63
5.1. Gouy Phase effect on multicolour Gaussian beams 64
5.1.1. Influence on the waveform 66
5.1.2. Linear compensation 67
5.2. Methods 68
5.2.1. PIC Simulations 68
5.2.2. Modelling the Gouy Phase in 1D PIC simulations 70
5.3. Results 71
5.4. Parameter Scan 73
5.5. Conclusions 75

6. Conclusion 77
6.1. Outlook and Future Work 78

A. Appendix 81
A.1. Ion acceleration with the TNSA mechanism 81
A.1.1. Ring-Like structures 82

B. Bibliography 85

C. Table of commonly used symbols 95

D. Relativistic Units 97

E. List of Publications 99

F. Ehrenwörtliche Erklärung 101

G. Acknowledgements 103

1. Introduction

It is a long standing challenge in various disciplines of the natural sciences - biology, chemistry, physics - to explore the structure of proteins, molecules or even probe the time resolved electron distribution in atoms, on the length scale of 1 Å = 10^{-10} m and 1 as = 10^{-18} s [1–3]. To be able to resolve such ultrashort length- and timescales, it is necessary to use radiation with wavelengths smaller than the structures and pulses shorter than the timescale of the processes to investigate. Another potential application of such pulses, requiring ultra-intense radiation with wavelengths as small as possible to break the Schwinger limit, is the probing of the quantum vacuum with an all-optical setup, which has recently been proposed [4–10]. Coherent ultrashort and ultraintense pulses of electromagnetic radiation with wavelengths in the range of extended violet (XUV) and X-Rays (< 40 nm) have the potential to fulfil these requirements.

Often, these experiments are performed as pump-probe experiments with an additional need for a high-power laser system in the optical regime. The availability of facilities which are able to provide the infrastructure for those kind of experiments is very limited. Currently, Free Electron Lasers (FEL) are the only readily available instruments to provide such radiation to scientific users. Due to the need to accelerate electrons to high energies in the range of 10^{10} eV, they need huge structures and are expensive to build. The newest FEL in Germany, called XFEL, uses a 3.4 km long tunnel from the state of Hamburg to the state of Schleswig-Holstein, at a total cost of 1.22 billion euro [11].

Naturally, beamtime at such facilities is limited and therefore the need arises for smaller, more cost-effective solutions which are able to provide XUV and X-Ray radiation with similar properties. There are proposals which evolve around replacing parts of the conventional FEL with optical or plasma components. The acceleration stage could be replaced by Laser Wakefield Acceleration (LWFA) of electrons in an underdense plasma, providing much stronger field gradients in the range of 100 GV/m [12]. Recently it has been proposed to replace the conventional undu-

lator by a plasma undulator, providing higher photon yield and again shortening the undulator length that is needed [13]. While all these proposals are very promising, technical obstacles have still to be solved until an all-optical plasma based FEL is shown to work.

Another purely laser-plasma based way of generating coherent XUV and X-Ray pulses in a tabletop setup is the generation of high order harmonics of the fundamental laser frequency from the surface of an initially non-transparent, overdense plasma target, called Surface Higher Harmonic Generation (SHHG) [14]. In first experiments with nanosecond CO_2 laser pulses, higher orders of the laser fundamental wavelength have been generated from laser-plasma interactions [15, 16]. In this experiments, the dimensionless laser amplitude[1] $a_0 = \frac{eE}{m_e \omega_L c}$ was $a_0 \approx 1$. With the advent of the chirped pulse amplification (CPA) [17], high power laser pulses in the femtosecond regime became available. The first "modern" SHHG experiments, which showed that this method is able to produce short bursts of coherent XUV radiation, were performed independently by [18–20] with a laser pulse intensity of 10^{17} W/cm^2. In the following years, the achievable laser intensities increased significantly and the laser-plasma interaction was investigated theoretically and numerically with Particle-In-Cell (PIC) simulations [21]. Several models have been proposed to describe harmonic generation mechanism for different parameter regimes, most notably Coherent Wakefield Emission (CWE) [22, 23], the Relativistic Oscillating Mirror (ROM) [4, 24, 25] and most recently Coherent Synchrotron Emission (CSE) [26, 27]. Together with PIC simulations [25, 28], these models helped explain experimental results [29] and informed novel experimental setups.

The long term goal is to provide a table top XUV light source, which is suitable for pump-probe experiments. The results presented in this thesis should provide important steps towards this goal. The thesis is dedicated to investigate possible routes for optimizing the properties of the generated XUV radiation and enhancing the efficiency of the harmonic generation process utilising PIC simulations guided by analytical considerations and models to explain the underlying physics. The PIC simulations are either performed with the 1-dimensional, 3 velocity components (1D3V) code PICWIG [30] or the 2D code EPOCH [31]. The assumed laser pulse intensity is close to that already available at present facilities or which will be available in the near future [32].

This thesis is structured as follows: In chapter 2, the basics to mathematically

[1] See Appendix for the definition of commonly used symbols

describe laser-plasma interactions are presented and the state of the art literature on SHHG is reviewed. In chapter 3, the possibility to gate a single attosecond pulse from a few-cycle incident laser pulse by choosing a appropriate carrier-envelope phase (CEP) is discussed. Another gating method is discussed in chapter 4, where the attosecond lighthouse effect is used to separate individual APs spatially. The implications of surface denting for the pulse separation are discussed in detail. One possible method to enhance the efficiency of the harmonic generation process is using multiple passes. Chapter 5 investigates the importance of optimizing the target distance between the passes.
In a collaboration with G. A. Becker, PIC simulations supporting experiments for ion acceleration with target normal sheath acceleration (TNSA) have been performed [33]. These results are summarized in appendix A.1.

2. Theoretical Background

2.1. Basics of plasma physics

In this thesis, the focus is on the simulation of ultraintense laser pulses interacting with a plasma. Yet, the exact definition of a plasma is not straightforward. In the following section, the main properties of a plasma and analytic and numerical approaches to describe the behaviour under the influence of an electromagnetic field are discussed.

A plasma consists of fully or partly ionized atoms, with electrons being able to move freely [34]. The number density can be within a wide range - from gaseous to solid density, depending on how the plasma was formed. On a macroscopic scale, the plasma is initially electrical neutral. It acts as a nearly perfect conductor, but distinct from metals, the ions are not fixed in a grid, but can move freely as well. Ion motion is generally slower than the electron motion due to the higher inertia. Plasma can be produced in a wide variety of ways - from astrophysical plasmas, electrical discharges to ultraintense laser pulses. Although in all cases, the underlying physics is broadly similar, the approaches to compute the temporal evolution from a given set of initial conditions differ vastly.

Here, the focus will be on plasmas generated by the interaction with a ultraintense, ultrashort laser pulse with an initially solid target. The main numerical tool used to simulate this kind of interaction are Particle-In-Cell (PIC) simulations, which are discussed in detail in section 2.2. Before turning to the simulations, some basic equations governing the time evolution of a plasma shall be discussed first.

An important quantity to describe the plasma is the plasma frequency, which is directly dependent on the density

$$\omega_p = \sqrt{\frac{n_e e^2}{m_e \epsilon_0}} \quad , \tag{2.1}$$

where n_e is the electron number density, e the elementary charge, m_e the electron

mass and ϵ_0 the dielectric constant. Intuitively the plasma frequency is the oscillation frequency of the electrons, if they are displaced from their equilibrium position. In laser-plasma interactions, the main interest is in the time-evolution of the plasma under the influence of an external electromagnetic field. Computing the full trajectory of every single particle is neither possible nor desirable. Instead, the collective behaviour of the plasma on a macroscopic scale is of interest. One possibility to describe these macroscopic quantities is the Vlasov-Equation

$$\frac{\partial f_j}{\partial t} + \mathbf{v} \cdot \nabla f_j + \frac{1}{m_j} \left(\mathbf{F}_{\text{ext}} + q_j \left(\mathbf{E} + \mathbf{v} \times \mathbf{B} \right) \right) \cdot \nabla_v f_j = 0 \quad , \tag{2.2}$$

where f_j is the phase-space distribution function for each particle species ($j = \{e, i\}$ for electrons and ions) with charge q_j, $\mathbf{F}_{\text{ext}}$ the external field and $\mathbf{E}$ and $\mathbf{B}$ the internal electric and magnetic fields induced by the charged particles. Together with Maxwell's equations (see equations 2.3-2.6 in the next section) they form a set of self-consistent partial differential equations. By solving this equation in the 6-dimensional phase space for every species, one could in principle calculate the time-evolution of the plasma response to the external field. In practice, solving a 6-dimensional partial differential equation is only possible for a very limited number of special cases. Particle-In-Cell (PIC) simulations are a way to circumvent this obstacle by discretising the distribution function with so-called macro-particles and solving the electromagnetic fields on a grid. It is thus an approximate solution to the Vlasov-Equation. In the next section, PIC simulations and their limitations are discussed in detail.

2.2. Particle-In-Cell (PIC) simulations

Particle-In-Cell (PIC) simulations are widely used in the plasma physics community [21]. Many important publications in the plasma physics field in recent years use them - with this thesis being no exception -, either relying on them exclusively or to explain experimental observations or estimate parameters. Latest simulations on the fastest super-computers available to the scientific community aim at simulating full experiments.

While extensive computer simulations are certainly the future, it is important to remain vigilant about the pitfalls computer simulations and in particular PIC simulations bring with them. These can be either principle limitations of the un-

derlying model or numerical limitations which can be circumvented by using the right method. To detect these limitations, it is important to understand the PIC algorithm and to cross-check the results with analytic theories and experiments, wherever possible. The aim of this chapter is to provide convincing evidence that the results of the PIC simulations with the codes PICWIG1D and EPOCH shown in this thesis are indeed correct. Firstly, by explaining the PIC algorithm in detail and secondly by comparing a PIC simulation with actual experimental data obtained at the JETI200 laser facility in 2017. A third part will discuss the effect of numerical dispersion on SHHG simulations and how to mitigate it.

2.2.1. The PIC algorithm

The aim of PIC simulations is to solve Maxwell's equations and the equations of motion of particles self-consistently. This is an initial value problem with a given distribution of charged particles and electromagnetic fields. The time-evolution of the fields and particles are computed in discrete timesteps. In addition, the boundary conditions for the simulation box have to be given for all times and can be used to inject a laser pulse into the simulation box. While all electromagnetic fields are computed on a discrete grid, the particles move freely inside the simulation box and have continuous coordinates $\mathbf{x} = (x, y, z)$ and momenta $\mathbf{p} = (p_x, p_y, p_z)$.
Inherent to this model are some principle limitations of PIC simulations one needs to be aware of. The grid resolution limits the highest frequency which can be resolved in the simulation. According to the Nyquist-Shannon sampling theorem [35], the sampling frequency (i.e. the number of grid points per wavelength) has to be at least twice the frequency of the signal (i.e. oscillations of the electromagnetic field). In order to obtain any physically meaningful results, the grid must be fine enough to resolve the highest frequency of interest in the simulation. For simulations of an underdense plasma, this is usually the laser frequency. For simulations of solid density plasma which are relevant here, the highest frequency is usually the plasma frequency $\omega_p \propto \sqrt{n}$ with n the number density of the plasma.
The other principle limitation is with regard to particles. The macro-particles in the simulation are collisionless and are not treated as point particles, but rather as finite sized particles having a shape that can span across multiple cells and a weight w, giving the fraction of a physical particle they represent. It is therefore better to view particles in PIC simulations as a discretization of the density distribution rather than actual physical particles.

Due to their finite size, particles cover at least a volume spanning as wide as the Debye length of $\lambda_D = \frac{\nu_{\text{thermal}}}{\omega_p}$, where ν_{thermal} is the thermal frequency. This implies that any scales smaller than the Debye length are not covered by the simulations. In combination with the valid assumption that the typical scale L of the plasma simulated here is much larger than the Debye length, the collision cross-section and frequency are much smaller compared with point particles and the assumption of a collisionless plasma is therefore justified [21]. As is shown in the next section, the macroscopic behaviour of the plasma is still reproduced very well.

There are multiple particle species in every simulation, which differ in charge and mass to be able to represent electrons and different types of ions. The electromagnetic fields are governed by Maxwell's equations and only computed on a discrete grid with a spacing Δx, Δy, Δz.

$$\nabla \cdot \mathbf{E} = \frac{\rho}{\epsilon_0} \tag{2.3}$$

$$\nabla \cdot \mathbf{B} = 0 \tag{2.4}$$

$$\frac{\partial \mathbf{B}}{\partial t} = -\nabla \times \mathbf{E} \tag{2.5}$$

$$\frac{\partial \mathbf{E}}{\partial t} = c^2 \nabla \times \mathbf{B} + \frac{\mathbf{j}}{\epsilon_0} \tag{2.6}$$

The temporal and spatial derivatives are discretized to compute the fields at time $t + \Delta t$ from the fields and currents at time t. This is often accomplished with the Yee solver [36], but more sophisticated approaches have been developed to avoid numerical dispersion [37] (see also section 2.2.3). Note that the first two Maxwell's equations are only constraints, which are solved once in the beginning to provide the correct initial values. The time-evolution is purely based on the latter two equations, ensuring that the continuity equation

$$\frac{\partial \rho}{\partial t} + \nabla \mathbf{j} = 0 \tag{2.7}$$

is conserved at all times.

This requires the particles to be mapped to the grid using their particle shape. From the particle distribution, the (charge) density distribution and the current

distribution are computed and used as sources in the Maxwell solver.

$$\mathbf{j} = \sum_{i=0}^{N} q_i w_i \mathbf{v}_i \delta\left(\mathbf{x} - \mathbf{x}_i\right) \tag{2.8}$$

$$\rho = \sum_{i=0}^{N} q_i w_i \delta\left(\mathbf{x} - \mathbf{x}_i\right) \tag{2.9}$$

After this step, the particles are advanced according to the newly computed electromagnetic fields. As the particles are allowed to move freely, the electromagnetic field has to be interpolated from the nearest grid points i and $i+1$ at the particle position x_p:

$$E(x_p) = \frac{x_{i+1} - x_p}{\Delta x} E_i + \frac{x_p - x_i}{\Delta x} E_{i+1} \tag{2.10}$$

Finally, the new particle positions are calculated by solving the equations of motion

$$\frac{\mathrm{d}\mathbf{p}_i}{\mathrm{d}t} = q_i \left(\mathbf{E} + \mathbf{v} \times \mathbf{B}\right) \tag{2.11}$$

$$\frac{\mathrm{d}\mathbf{x}_i}{\mathrm{d}t} = \frac{\mathbf{p}_i}{\gamma_i m} \tag{2.12}$$

and the cycle begins anew.
The essential steps are summarized in figure 2.1. It is important to note that every other addition to PIC codes that has recently been proposed, including ionization, collisions or QED effects like pair production for instance, are not part of this self-consistent cycle and sit "on top". Therefore, one has to be very careful about the inherent limitations these additions have.

2.2.2. Experimental Data and PIC simulations

This attempt to compare simulation data to actual experiments will be limited to a qualitative study. At this point, it is generally not possible to predict the quantitative result of an experiment by computer simulations except for specific types of experiments like Laser-Wakefield-Acceleration (LWFA) or Plasma-Wakefield-Acceleration (PWFA) [38]. Deviations between experiment and PIC simulations have been reported by others [39] as well. This has several reasons:

- **Experimental uncertainties:** Especially the exact laser parameters are not known and can vary from shot to shot. The temporal and spatial profile in focus is not necessarily Gaussian.

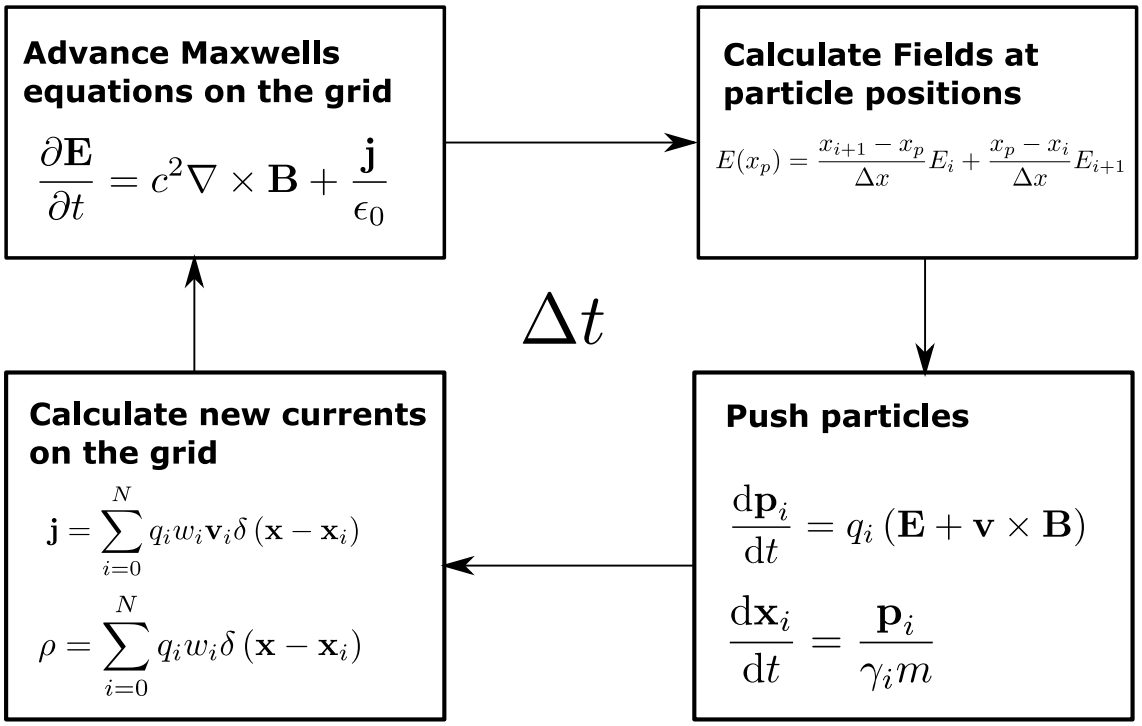

Figure 2.1.: Main stages of the Particle-In-Cell algorithm.

- **Numerical limitations:** The simulations here are limited to 2D, which gives a different focusing behaviour of a Gaussian beam. The accuracy is limited by the resolution, which is limited by computational resources.
- **Principle limitations:** The core PIC algorithm only covers a collision-less, pre-ionized plasma, which is usually a good approximation, but does not cover the complete plasma dynamics. Line emissions and ionization are not included in the self-consistent solution.

That being said it is still interesting to benchmark a PIC simulation against an experiment at least once, where the parameters are quite well known. The experimental data shown here has been obtained at the JETI200 laser facility in 2017 by *Li Lu et. al.*, who kindly gave permission to reproduce it here. The laser parameters were in this case a duration of $\tau = 23$ fs, energy of $E = 3.6$ J before compressor and a FWHM laser spot size on target of 4 μm. This translates to an intensity of $I = 3 \cdot 10^{20} \frac{\mathrm{W}}{\mathrm{cm}^2}$ or $a_0 = 13$. Strictly speaking, this is the average intensity over the FWHM area of the focal spot, while the peak intensity will be higher. But for a qualitative comparison, the difference should be negligible.
In figure 2.2, the integrated spectrum from the experiment is compared to the results

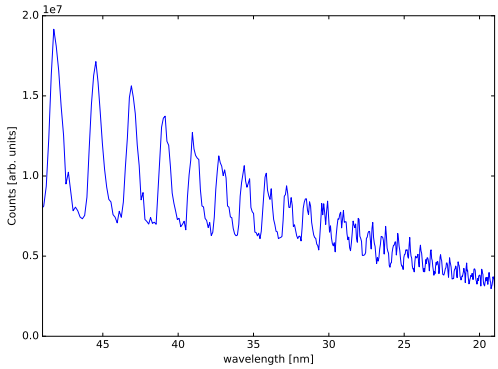

(a) 2D EPOCH PIC simulation for comparison with the parameters $a_0 = 13$, $\tau = 23fs$, $n = 200n_c$, $L_p = \lambda_0/10$.

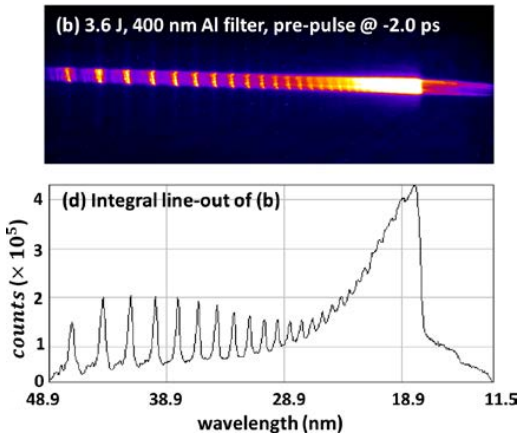

(b) Experimental SHHG data provided by Li Lu et. al. obtained at the JETI200 laser facility at the Helmholtz Institute in Jena with an optimised pre-pulse delay at 2.0 ps before the main pulse. The full beam energy is 3.6 J before compressor.

Figure 2.2.: Comparison between 2D PIC simulation **(a)** and actual experimental data **(b)**. In general, the simulation is able to reproduce the harmonic spectrum as seen in the experiment. The experimental spectrum deviates from the simulation for wavelengths shorter than 28.9 nm due to the aluminium filter transmission.

of a PIC simulation. Both plots show the same range of wavelength between 49 nm and 19 nm. The obvious difference is that the harmonic intensity appears to be increasing towards shorter wavelengths. This is due to the aluminium filter before the detector being more transmissive for shorter wavelengths [40] and not an actual increase in intensity. In the wavelength range where the results are comparable, the PIC simulation is in qualitatively good agreement with the experiment.

2.2.3. Effect of numerical dispersion on SHHG simulations

A laser pulse propagating in vacuum shows no dispersion, as the dispersion relation is $\omega = c\,|k|$. Consequently, in that case the phase and group velocity are both equal to the speed of light, $v_{ph} = v_g = c$. The electromagnetic fields in a PIC simulations are computed on a grid with a certain spacing, Δx, Δy and Δz, and for discrete timesteps Δt. Depending on the numerical method used to solve Maxwell's equations, this finite grid can introduce an artificial numerical dispersion [37, 41].

This is due to the fact that the grid has a limited resolution, which defines the smallest wavelength and the highest frequency it can resolve. Different frequencies travel with slightly different velocities across the grid, i.e. slower or even faster than the speed of light. It can be treated like a dispersive medium with a dispersion relation given in dependence of Δt, Δx and Δy. For the common Yee grid [36] the grid dispersion relation is [41]

$$\frac{\sin\left(\frac{1}{2}\omega\Delta t\right)}{c\Delta t} = \frac{\sin\left(\frac{1}{2}k_x\Delta x\right)}{\Delta x} + \frac{\sin\left(\frac{1}{2}k_y\Delta y\right)}{\Delta y} + \frac{\sin\left(\frac{1}{2}k_z\Delta z\right)}{\Delta z} \tag{2.13}$$

The dispersion is the lowest along the grid diagonals and the highest along the grid axes. This is not favourable for many laser-plasma simulations, as the incident laser and the generated radiation usually propagate along an axis.

This unphysical behaviour has been noticed first in LWFA simulations [42]. Numerical Cherenkov radiation appears, when electrons in the simulation travel faster than the phase velocity of the grid. Its adverse effects are not limited to LWFA simulations, but affect SHHG simulations as well.

To avoid the numerical dispersion effects of the original Yee scheme, a method using higher-order finite difference time domain (FDTD) Maxwell solvers has been developed, which uses optimized coefficients to minimize the numerical dispersion along the grid axes [37, 42]. One trade-off of this scheme is the increased computational load, both due to the higher order stencils and a smaller time step.

A good compromise is the “min. 3” stencil from [37], which will be used from here on. A comparison between two spectra obtained from SHHG PIC simulations using the EPOCH code [31] with the original Yee stencil and the optimized stencil is shown in figure 2.3. Both simulations were run with exactly the same parameters, in particular with the same spatial resolution of 400 cells per μm. It can be clearly seen that the harmonic lines above the 30th harmonic are bent to the left, i.e. that those harmonics are emitted under a different angle than the fundamental and lower orders. This behaviour is not seen with the nearly dispersion free optimized stencil.

With lower resolutions than 400 cells per μm, this bend becomes even more pronounced, which leads to the conclusion that it is most likely an unphysical numerical artefact. From the two graphs one can estimate at which resolution this numerical effect becomes visible. The 30th harmonic of a 800 nm laser pulse corresponds to a wavelength of 27 nm. The grid resolution of 400 cells per μm corresponds to a $\Delta x = 2.5$ nm, which is about 1/10 the wavelength and far above the Nyquist-

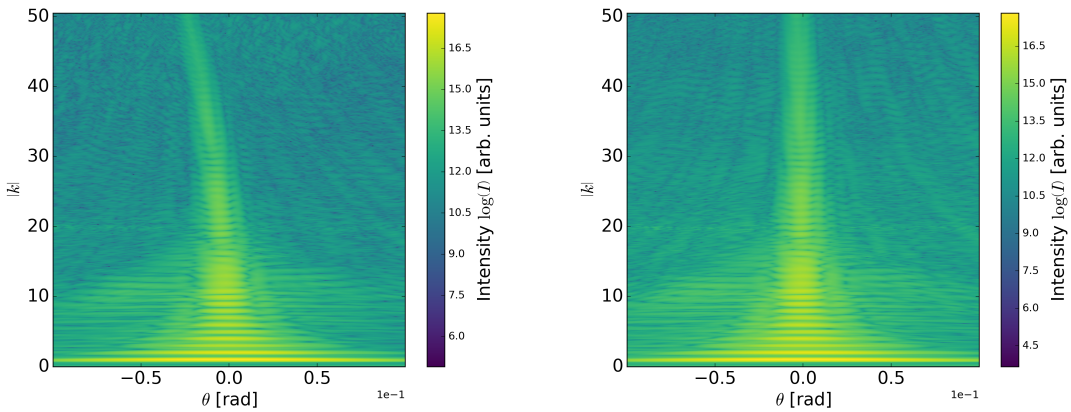

(a) Yee stencil (b) Optimized stencil "min. 3"

Figure 2.3.: Effect of numerical dispersion on a SHHG spectrum. Both simulations are run with the same parameters: $a_0 = 10$, $\tau = 5$ fs, 5 μm spotsize, $n = 100n_c$, no preplasma, 400 cells per μm resolution.

Shannon limit. In conclusion, PIC simulations with a Yee stencil can only be fully trusted up to 1/10 of the grid resolution. The optimized stencil improves this resolution boundary considerably.

While the Yee scheme can be used for 1D PIC simulations as well, there is an obvious better choice in this special case. One can separate the fields into forward and backward propagating waves, one pair for each polarization (see equations 2.14), which can then be advanced simply by moving them in the appropriate direction, if the timestep is equal to the grid spacing: $\Delta t = \Delta x/c$. Numerically, this is just a copy operation and any numerical dispersion can be avoided.

$$\begin{aligned} P_+ &= \frac{1}{2}(E_y + B_z) \\ P_- &= \frac{1}{2}(E_y - B_z) \\ M_+ &= \frac{1}{2}(E_z + B_y) \\ M_- &= \frac{1}{2}(E_z - B_y) \end{aligned} \tag{2.14}$$

Here, P and M are the two different polarizations, where the $\pm$ index denotes the propagation direction. The standard E and B fields can be recovered by superposition of the P and M fields.

2.3. Gaussian Pulses

A Gaussian pulse, or some other spatially confined pulses, can be described by separating the slowly varying envelope $v(r)$ from the fast oscillating term associated with propagation.

$$E_y(\mathbf{r}, t) = v(\mathbf{r}, t) \exp\left(i(kz - \omega t)\right) \tag{2.15}$$

Usually, the envelope is described in the paraxial approximation, which is valid if $k_x^2 + k_y^2 << k_z^2$. For a Gaussian beam propagating in z direction with x and y as transverse coordinates it reads

$$v(x, y, z) = A_0 \frac{1}{\sqrt{1 + \left(\frac{z}{z_r}\right)^2}} \exp\left[-\frac{x^2 + y^2}{w_0^2 \left(1 + \left(\frac{z}{z_r}\right)^2\right)}\right] \exp\left[i\frac{k}{2}\frac{x^2 + y^2}{z\left(1 + \left(\frac{z_r}{z}\right)^2\right)}\right] \exp(i\varphi) \tag{2.16}$$

where $\varphi = \arctan\left(-z/z_r\right)$ is the Gouy phase and $z_r = \pi w_0^2/\lambda_0$ the Rayleigh length. The focus position in this coordinate system is at $z = 0$. Naturally, this equation is derived for a 3D geometry, where the pulse propagates in z and has transverse components in x and y. Plasma physics simulations, especially Particle-In-Cell (PIC) simulations of surface high harmonic generation (SHHG) are often run in 2D, as they are computationally expensive. It is therefore important to note that the behaviour of Gaussian pulses is different in 2D geometry. The paraxial equation in 2D for a Gaussian pulse propagating along the x axis reads

$$v(x, y) = \frac{A_0}{\sqrt[4]{1 + \left(\frac{x}{x_0}\right)^2}} \exp\left[-\frac{y^2}{w_0^2 \left(1 + \left(\frac{x}{x_0}\right)^2\right)}\right] \exp\left[i\frac{y^2}{2x\left(\frac{x_0 w_0^2}{2x^2} + \frac{1}{k}\right)}\right] \exp\left(i\frac{\varphi}{2}\right) \tag{2.17}$$

There are some differences to the 3D case. In particular, the intensity falloff is slower ($\propto 1/z$ vs $\propto 1/z^2$), the Gouy phase is only half the value and the focus is a line focus rather than a point focus. Only the beam waist evolves in the same way ($\propto \exp\left(-1/z^2\right)$).

2.4. Gouy Phase

The Gouy Phase is an axial phase shift which exists only in spatially confined beams such as Gaussian beams [43] passing through a focus. It has been first described by

M. Gouy in 1891 [44]. The effect of the Gouy phase is best visualized by comparing a focused beam to a plane wave, which naturally does not have a Gouy phase. As it is shown in figure 2.4, both the plane wave and the Gaussian beam are in phase at the focus position. Propagating about one Rayleigh length before or after the focus, the Gaussian beam shows a phase shift of $\pm\pi/2$ with relation to the plane wave, amounting to a total phase shift of π while passing through the focus.
A closer look at the origin of the Gouy phase reveals that this value is only true for Gaussian beams in three dimensions. The general expression to calculate the Gouy

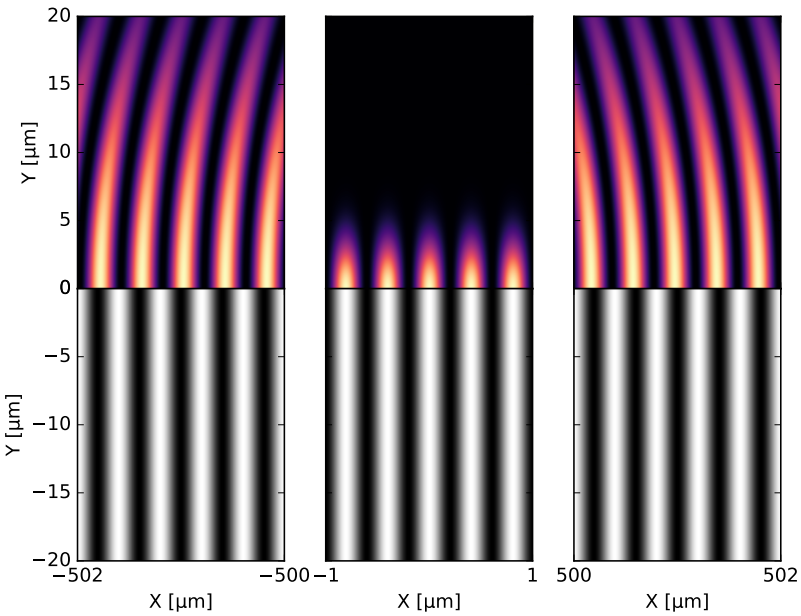

Figure 2.4.: Graphical representation of the Gouy Phase. The effect of the Gouy phase can only be made visible by comparing a Gaussian (or any other spatially confined beam, top row) to a plane wave (bottom row). In focus (middle panels) both are in phase, as it can be seen from the intensity maxima lining up. About a Rayleigh length before and after the focus the phase is shifted by $\pm\pi/2$ compared to the focus, which amounts to the total phase shift of π for the Gouy phase in a 3D Gaussian beam.

phase for a given spatial envelope function $F(k_x, k_y)$ is [43]

$$\varphi = -\frac{1}{k}\int \left(\left\langle k_x^2\right\rangle + \left\langle k_y^2\right\rangle\right) \mathrm{d}z \tag{2.18}$$

where $\left\langle k_{x,y}^2\right\rangle = \int\int_{-\infty}^{+\infty} k_{x,y}^2 \left|F(k_x, k_y)\right| \mathrm{d}k_x \mathrm{d}k_y$ are the expectation values of $k_{x,y}$. For

a Gaussian beam, it is $\left\langle k_{x,y}^2 \right\rangle = 1/w^2(z)$ and carrying out the integration from equation 2.18 gives rise to the well-known result $\varphi = -\arctan(z/z_r)$.
In 2D geometry, where the Gaussian beam is a cylindrical wave with a line focus instead of a spherical wave with a point focus, the Gouy phase shift is just half that value, $\varphi = -0.5 \arctan(z/z_r)$. This is intuitively clear from equation 2.18, as in two dimensions there is just one degree of freedom for the wave vector in contrast to two degrees of freedom in three dimensions.
Another way of looking at this could be the following: The magnitude of the wave vector $|k|$ is constant, as it is defined by the wavelength. A plane wave travelling in z direction has only one vector component in z, thus $k_z = k$. A Gaussian pulse (or any other spatially confined pulse) is always a superposition of many plane waves with slightly different wave vectors $\mathbf{k} = (k_x, k_y, k_z)$. Thus, the pulse has a finite spread of wave vector components in k_x and k_y. As the magnitude of the wave vector $|k|$ is fixed, this means that the k_z component must be smaller compared to the plane wave. This difference gives rise to the Gouy phase shift.

2.5. Spatio-Temporal Couplings (STC)

Usually, Gaussian pulses are treated in a way where the temporal and spatial components can be separated into independent functions, $E(\mathbf{r}, t) = E(\mathbf{r})E(t)$. This is no longer possible when spatio-temporal couplings (STC) are involved. Mathematically speaking, STCs introduce a mix-term $C\mathbf{r}t$ with a coupling parameter C, which defines the strength of the coupling. C is in general a complex number, where $\Re\{C\}$ corresponds to a coupling in amplitude and $\Im\{C\}$ to a coupling in phase.
The laser pulse can be described in the real space of (x, t) coordinates. Alternatively, any of the coordinates could be transformed to the frequency space using a Fourier transformation, yielding (x, ω), (k, t) and (k, ω) as possible coordinate systems. In each space, the coupling parameter takes on a different physical meaning.
In the other domains, the coupling parameter takes on other meanings [45]. In particular, in the (x, ω) domain, the coupling parameter $\Re\{R_{x\omega}\}$ corresponds to a spatial chirp (the frequency changes with the transverse spatial coordinate) and in the (k, ω) domain, $\Im\{S_{k\omega}\}$ corresponds to a angular spectral chirp (the frequency varies with the propagation direction) [45]. Especially the latter is important for the concept of the angular streaking, see chapter 4.
In (x, t) coordinates and in the most general form, a Gaussian laser pulse in time

and space can be described as

$$E(x,t) \propto \exp\left(Q_{xx}x^2 - Q_{tt}t^2 - 2Q_{xt}xt\right) \tag{2.19}$$

with Q_{xx}, Q_{tt} and Q_{xt} complex coefficients. If the coupling parameter $Q_{xt} \neq 0$, STCs are present. $\Re\{Q_{xt}\}$ corresponds to a coupling in amplitude. This creates a pulse front tilt (PFT), where the transverse position of the pulse centre depends on time (see figure 2.5, top panel). $\Im\{Q_{xt}\}$ corresponds to a coupling in phase and is responsible for a wave-front rotation, where the shapes of the wave-fronts are dependent on the transverse coordinate and time (WFR) [45] (see figure 2.5, bottom panel).

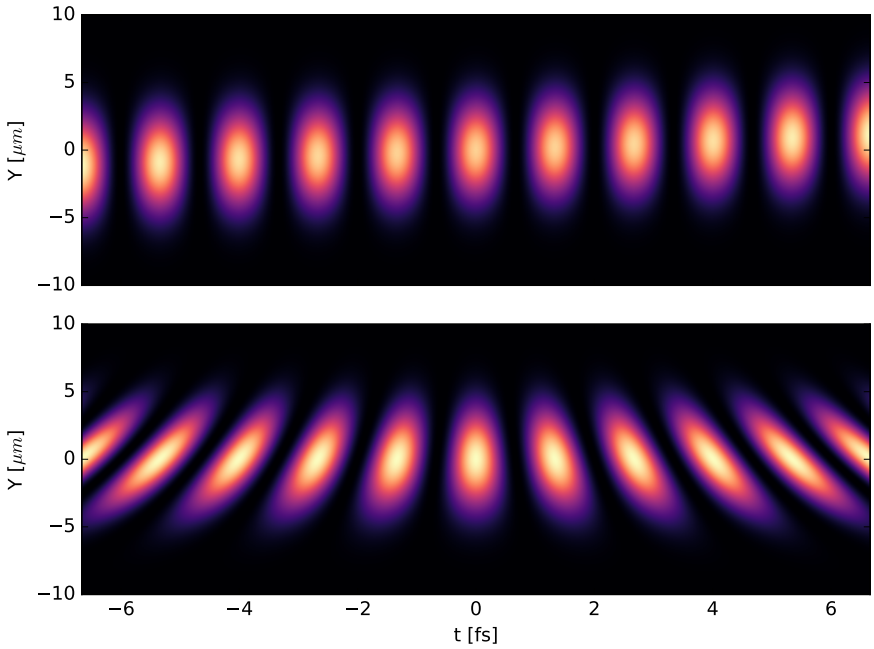

Figure 2.5.: A Gaussian pulse with pulse front tilt (PFT, top panel) compared to a Gaussian pulse with wave front rotation (WFR, bottom panel).

The well-known equation for a Gaussian pulse without STCs is obtained for $Q_{xx} = -\frac{1}{w^2(x)} - i\frac{\pi}{\lambda R(x)}$ and $Q_{tt} = \frac{1}{\tau^2}$ with $w(x) = w_0\sqrt{1+\frac{x}{z_R}}$ and $R(x) = x\left(1+\left(\frac{z_R}{x}\right)^2\right)$ the known functions for the evolution of the beam waist and radius of curvature [46]. Written in a more conventional notation, the coupling in amplitude in the focus of a monochromatic Gaussian laser pulse can be expressed as

$$\exp\left(-y^2/w_0^2 - t^2/\tau^2\right) \rightarrow \exp\left(-y^2/w_0^2 - t^2/\tau^2 + \zeta yt\right) \quad , \tag{2.20}$$

with ζ the coupling parameter. Likewise, a coupling in phase is achieved by introducing a coupling term to the imaginary part of equation 2.15.

$$\exp\left(i(kz - \omega t)\right) \rightarrow \exp\left(i(kz - \omega t + \xi y t)\right) \tag{2.21}$$

Equations for the coupling parameters out of focus can be derived using the Kostenbauder matrix formalism [47] (see also the example given in section 4.1). Both effects are not the same, but are related: a PFT before focus will be transformed to a WFR in focus and vice versa [48].

Experimentally, a PFT can be achieved by misaligning the compressor stage of a laser system, which will in turn generate a WFR in the laser pulse focus. Generally, this is something one wants to avoid, as it makes the pulse longer and decreases the achievable peak intensity in focus. For the attosecond lighthouse effect (see chapter 4) however, this is exploited to generate spatially separated attosecond pulses.

2.6. Single Particle Motion in a relativistic Laser Pulse

The motion of a single charged particle in an electric field is classically described by the Lorentz force. For an electron with charge $q = -e$ it reads in *cgs*-units

$$\frac{\mathrm{d}\mathbf{p}(x,t)}{\mathrm{d}t} = -e\mathbf{E}(x,t) + \frac{e}{c}\left(\mathbf{v}(x,t) \times \mathbf{B}(x,t)\right) \quad . \tag{2.22}$$

For low intensities, the velocity of the particle is much less than the speed of light, so that the $\mathbf{v} \times \mathbf{B}$ term can be neglected and the particle just moves along the electric field. With a stronger electric field, the particle's velocity will be eventually high enough to be comparable with the speed of light. At this point, the $\mathbf{v} \times \mathbf{B}$ term can no longer be neglected and the motion of the particle changes significantly. It is common to introduce the dimensionless laser amplitude

$$a_0 = \frac{eE_0}{mc\omega_L} \tag{2.23}$$

as a measure whether the interaction is relativistic. For values of $a_0 \geq 1.0$, the cycle-averaged kinetic energy of the electron becomes comparable to the rest mass

and the motion of the electron is relativistic. In terms of intensity this corresponds to $I[\mathrm{Wcm}^{-2}] = a_0^2 \lambda_L^{-2}\ [\mu\mathrm{m}^2]\ 1.37 \cdot 10^{18}\ [\mathrm{W} \cdot 10^8]$. For a central wavelength of 800nm, typical for a Titan-Sapphire laser system, the relativistic intensity is therefore $I = 2.14 \cdot 10^{18}\ \mathrm{Wcm}^{-2}$. The full equations of motion for a single particle can be derived using the Lagrange equation for the system.

For a charged particle in an external field, the relativistic Lagrangian is [49]

$$L = -mc^2\sqrt{1 - \frac{v^2}{c^2}} - e\phi - \frac{e}{c}\mathbf{v}\mathbf{A}, \tag{2.24}$$

where $\mathbf{A}(x,t)$ is the vector potential of the incident laser pulse. The scalar potential ϕ does not depend on $\mathbf{v}$ or $\mathbf{x}$ and can be neglected for the following considerations. The Euler-Lagrange equation connects the Lagrangian to the particle momentum. The canonical momentum is given by

$$\mathbf{P} = \frac{\partial L}{\partial \mathbf{v}} = -\frac{e}{c}\mathbf{A}(t,x) + \frac{m\mathbf{v}}{\sqrt{1 - \frac{v^2}{c^2}}} = \mathbf{p} - \frac{e}{c}\mathbf{A}(t,x). \tag{2.25}$$

To solve the equations of motion for the transverse components, the conservation of momentum is used. The Lagrangian does not depend upon the transverse coordinates y and z ($\frac{\partial L}{\partial y} = 0$ and $\frac{\partial L}{\partial z} = 0$), therefore, the transverse momentum is conserved.

$$\frac{\partial L}{\partial \mathbf{v}_\perp} = \mathbf{p}_\perp - \frac{e}{c}\mathbf{A}_\perp(t,x) = \mathrm{const.} \tag{2.26}$$

The constant is equal to the initial momentum. As the electron is assumed to be initially at rest, the transverse momentum equation reads

$$\mathbf{p}_\perp = \frac{e}{c}\mathbf{A}_\perp. \tag{2.27}$$

For the longitudinal component, conservation of energy is used to deduce a momentum equation. The relation between the Hamiltonian H and the Lagrangian L is

$$-\frac{\partial H}{\partial t} = \frac{\partial L}{\partial t} = -c\frac{\partial L}{\partial x} = -c\frac{\mathrm{d}p_x}{\mathrm{d}t}, \tag{2.28}$$

Integrating in time and substituting $H = E$, one retrieves

$$E - p_x c = mc^2 = \mathrm{const.} \tag{2.29}$$

or explicit form

$$E^2 = \left(mc^2 + p_x c\right)^2 . \tag{2.30}$$

Together with the relativistic energy conservation [49]

$$E^2 = \left(mc^2\right)^2 + c^2 \mathbf{p} \cdot \mathbf{p}, \tag{2.31}$$

one obtains

$$E^2 = (mc^2)^2 + (p_x c)^2 + (p_\perp^2 c)^2 = (mc^2 + p_x c)^2. \tag{2.32}$$

This equation is only valid if $p_x c = p_\perp^2/(2m)$. Therefore, the relativistically exact longitudinal momentum reads

$$p_x = \frac{p_\perp^2}{2mc}. \tag{2.33}$$

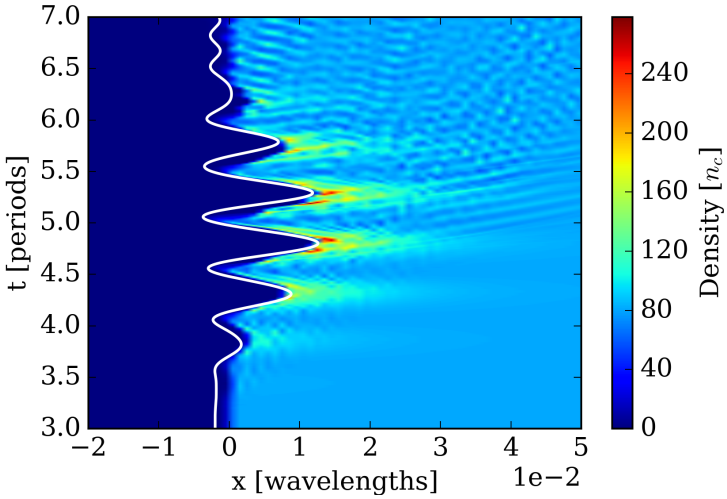

Figure 2.6.: Spatio-Temporal density evolution of the plasma surface, simulated with a 1D PIC simulation (colour scale) and the trajectory obtained from solving the equations of motion (equations 2.34-2.36) numerically (white line). The parameters are $a_0 = 5$, $n_e = 80 n_c$, linear polarization and normal incidence.

These equations are valid only for a single particle initially at rest interacting with a laser pulse in vacuum. The more common case is a laser pulse interacting with a pre-ionized quasi-neutral plasma slab. Here, the motion of a single particle at the surface of the plasma can be studied using a capacitor model. Assuming a quasi-neutral electron-proton plasma with electron density n_e in the positive half-space $x \geq 0$ and a laser pulse incident normally from the $-x$ boundary, the equations of

motion for a single electron on the surface are [50]

$$\frac{\mathrm{d}p_x}{\mathrm{d}t} = -\frac{v}{c}\frac{\partial \mathbf{A}(x,t)}{\partial x} - n_e x \tag{2.34}$$

$$\frac{\mathrm{d}x}{\mathrm{d}t} = \frac{p_x}{\gamma} \tag{2.35}$$

$$\mathbf{p}_\perp(x,t) = \frac{e}{c}\mathbf{A}(x,t) \quad . \tag{2.36}$$

Solving these equations numerically yields the trajectory of an electron on the surface of the plasma slab. For comparison, a 1D PIC simulation with a linearly polarized Gaussian laser pulse with $a_0 = 5$ normally incident on a step-like target with a density of $n_e = 80n_c$ has been performed. The spatio-temporal density evolution is shown in figure 2.6, together with the numerical solution of equation 2.34. The trajectory computed by the simple capacitor model follows closely the motion of the plasma surface obtained from the PIC simulation.

2.7. High Harmonic Generation from solid targets

In this section, the basic principles of high harmonic generation from solid targets irradiated by intense laser pulses are outlined. In this context, "intense" means an intensity $a_0 > 1$, where $a_0 = \frac{eA}{m_e c} = I\lambda^2/1.3 \times 10^{18}$ Wcm^{-2} μm^2. At this intensity, the motion of electrons in the electric field becomes relativistic and due to the non-linear plasma dynamics, high order harmonics of the laser frequency are generated in reflection and transmission. Due to the high laser intensities involved, it is common to model the solid target as a fully ionized non-collisional plasma [24, 25, 51]. Depending on the target density, laser intensity and preplasma scale length (or laser contrast), different interaction mechanisms prevail.

In this thesis, I will concentrate on the relativistic oscillating mirror (ROM) model, as this is the dominant mechanism for high intensity ($> 10^{18}$ Wcm^{-2}), high contrast and steep plasma gradient interactions [20, 52].

A competing process to ROM is Coherent Synchrotron Emission (CSE) [26, 27, 53, 54]. Instead of relying on the Doppler shift from an oscillating mirror, the XUV radiation is emitted by dense electron nanobunches periodically forming at the plasma-vacuum boundary. The process is most effective for very steep plasma gradients. In oblique incidence, it is difficult to distinguish between XUV emission from ROM and CSE, as it is emitted in the same specular direction and both can

occur over the course of the interaction depending on the evolution of the initial scale length. It has been shown both theoretically and experimentally [27] that it is possible to discern the processes in normal incidence. In this case, CSE can be observed in transmission behind the target, which rules out any emissions from the ROM mechanism. In this thesis, the focus will be on the XUV emission in reflection.

For completeness, coherent wake emission (CWE) is briefly discussed as well.

2.7.1. Coherent Wake Emission (CWE)

CWE is the dominant harmonic generation mechanism for intensities $a_0 \leq 1$, as the ROM harmonics need relativistic intensities to induce a Doppler shift on the reflected laser pulse [52].

Electron bunches from the plasma surface are pulled out into the vacuum by the electric field component of the incident laser pulse perpendicular to the target surface. When the field reverses, the electrons are pushed back into the plasma by electrostatic restoring forces, forming bunches of high charge density [55]. The bunches generated at different times have different excursion lengths. Those which move furthest away from the surface gain the most energy and have the highest velocity when they re-enter the plasma. Inside the plasma their velocity stays constant due to plasma screening. This leads to the crossing of trajectories inside the plasma with electron bunches which had a smaller excursion length [23, 52]. At the crossing points, the electron charge peaks for a short time $\tau_e \ll \tau_L$, exciting plasma oscillations with the local plasma frequency $\omega_p(x)$ [56], as long as $\tau_e \ll \frac{1}{\omega_p}$. The plasma frequency depends on the local density, which changes throughout the vacuum-plasma gradient. This leads to a rotating wave vector k of the plasma oscillations. Emission of high harmonics of the laser frequency happens each time when $\mathbf{k}$ is parallel to the surface (phase matching condition).

The principle upper limit of the generated frequencies is defined by the maximum target density: $\omega_p^{max} \propto \sqrt{n_{max}}$. For typical target densities of $100-400 n_c$, this upper limit is between the 10th and the 20th harmonic ($N_{\max} = \sqrt{n_e/n_c}$ [23]). Due to this limitations, CWE is not of interest for the laser-plasma interactions discussed in this thesis. Instead, the ROM mechanism described in the next section is the primary mechanism for the parameter range used here.

2.7.2. Relativistic Oscillating Mirror (ROM)

For high intensity laser pulses ($a_0 >> 1$), the ROM model can be used to explain the interaction [24, 52, 57]. The harmonics generated by ROM can be distinguished from harmonics generated by the CWE in two ways. All harmonics above the CWE cutoff have to be generated by the ROM mechanism and the ROM harmonics have a distinctly smaller divergence than CWE harmonics. The properties of the generated harmonics are mainly influenced by a set of laser and plasma parameters, in particular target density n and scalelength L_p, laser intensity a_0, polarization, duration τ and focus spotsize w_0.

The choice of the parameters is not independent of each other: The similarity parameter $S = n_0/a_0$ introduced by [58] defines a relation between the laser intensity and the plasma density, where the interaction dynamics is similar, as the trajectories of the plasma electrons are similar [59]. Likewise, L_p and a_0 both influence the amount of surface denting (see section 2.7.3) one can expect during the interaction. As all these parameters are coupled in one way or another, a complete parametric study is difficult, even more as no closed analytic description exist for the whole process.

In this section, the mechanism is explained for the simple case of a step-like plasma. The influence of different preplasma scale lengths is investigated in section 2.7.3 for surface denting and in section 3 with regard to the isolation of individual attosecond pulses.

A laser pulse with $a_0 >> 1$ and a duration in the range of a few $\tau \simeq 10$ fs is incident on an overdense target with a steep plasma gradient. The plasma acts as a nearly perfect mirror, but due to the relativistic intensities a nonlinear interaction between the laser pulse and the plasma results in the generation of high order harmonics. In oblique incidence, the electromagnetic field pulls the electrons away from the target across the plasma-vacuum boundary. The ions remain stationary due to their higher inertia. When the field reverses, the electrostatic restoring force between the ions and the electrons pulls the electrons back towards the target until the field reverses again. These two opposite forces cause the surface electrons to oscillate with velocities close to the speed of light. The laser pulse is reflected from this oscillating mirror, which causes the pulse to be Doppler shifted and the pulse fronts are steepened. Due to this process, the reflected pulse contains high order harmonics of the fundamental laser frequency. This macroscopic picture of the process is convenient to explain the process, however in the ultra-relativistic case one has to take into account individual electron trajectories on a microscopic level, which are responsible for the emission

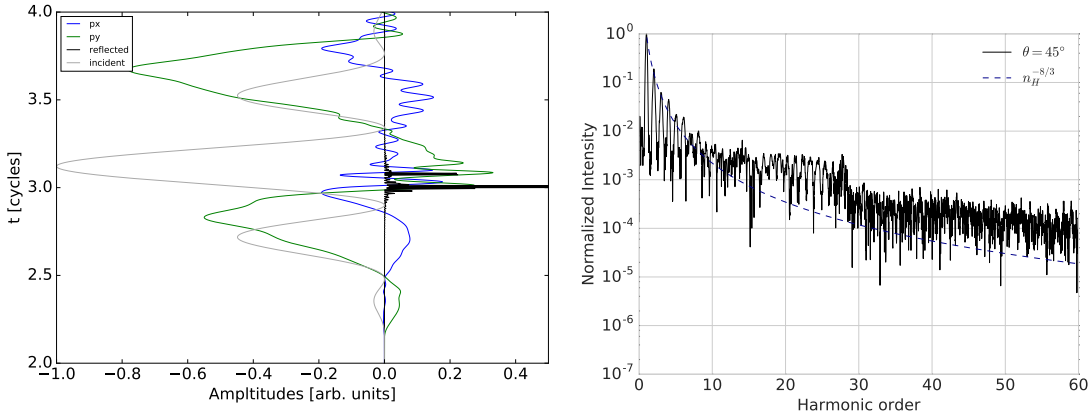

(a) (b)

Figure 2.7.: ROM harmonic generation process for a few-cycle laser pulse for an angle of incidence of $\theta = 45°$. **(a)** The momentum averaged over all particles p_x and p_y is shown alongside the generated APs. The APs are generated when $p_y = 0$ and p_x shows a maximum towards the incident laser pulse. **(b)** Typical harmonic spectrum from SHHG, $a_0 = 10$, $n = 200n_c$, $\tau = 4$ cycles, p-polarization and normalized to the fundamental. The harmonic intensity is slightly above the scaling law $I \propto n_H^{-8/3}$, which is expected for these parameters [56].

of attosecond pulses.

In normal incidence, the cause for the high harmonic generation remains the same, but the forces act slightly differently. Only the $\mathbf{v} \times \mathbf{B}$ force of the laser pulse, not the electric field itself accelerate the electrons in the longitudinal direction. They are pushed inwards into the target and are accelerated towards the laser pulse by the electrostatic restoring force. The emission of a attosecond pulse (AP) happens, when the electron momentum towards the laser pulse ($-p_x$) has a maximum and the p_y momentum switches sign. Snapshots of this process from 2D PIC simulations are shown in figure 2.8 and a video of the whole process is available online[1]. This condition is usually met multiple times during a laser pulse. Methods to gate a single AP from a few-cycle laser pulse are described in section 2.7.4.

A typical harmonic spectrum is shown in figure 2.7b. It is interesting to note, that for normal incidence, the spectrum only consists of odd harmonics, while there are all harmonics present in oblique incidence. The reason behind this is explained by equations 2.27 and 2.33. In normal incidence, the $\mathbf{v} \times \mathbf{B}$ force causes the electrons to oscillate with twice the frequency of the electric field. Consequently, all even

[1] https://tietze.xyz/phd/SurfaceHarmonicsDetail.mp4

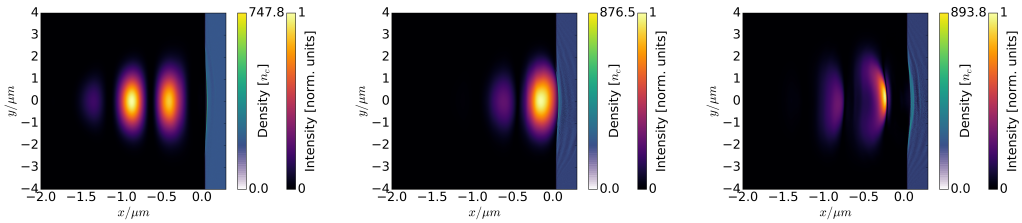

(a) t = 37.3 fs (b) t = 39.5 fs (c) t = 40.5 fs

Figure 2.8.: Three stages of surface high harmonic generations for normal incidence. Intensity of the laser pulse is displayed in red-yellow colour scale, electron density in blue-green colours. **(a)** The incident pulse pushes surface electrons inward. **(b)** Due to the restoring force, the electrons are accelerated towards the laser pulse and create high harmonics. **(c)** The reflected laser pulse has a distorted waveform, thus containing high harmonics. Parameters: $a_0 = 20$, pulse duration (FWHM) $\tau = 3$ fs, spotsize (FWHM) in focus 2 μm, p-polarization, initial electron density $n = 81n_c$, no preplasma.

harmonics are cancelled out because of destructive interference between the half cycles. The spectrum shows a characteristic falloff with a power-law of $\omega^{-8/3}$ [56]. In contrast to CWE harmonics, there is no cut-off frequency. In principle, the spectrum can extend to very high orders, if the incident laser intensity is high enough. A closer look at the spectral peaks reveals that not every harmonic is at the exact integer multiple of the fundamental frequency. The reason for this unequal spacing [60] is the surface motion during the laser-plasma interaction. As the plasma surface moves inward due to the laser pressure (see section 2.7.3), APs are generated at different depths, leading to a slight delay and thus to an irregular spectrum. It is important to note that each individual AP has a continuous spectrum. It is the interference of multiple APs which leads to the harmonics in the spectrum. A broad spectrum leads to ultrashort attosecond pulses, as both are connected by a Fourier transform. Therefore, it is of interest to generate a spectrum which extends to high harmonics at high intensities. As the available laser pulse intensity is limited, other techniques have been proposed to enhance the harmonic yield, for example using two colour laser fields [61] or multiple passes (see chapter 5).

2.7.3. Surface Denting

The incident laser pulse causes an oscillatory motion of the surface, with electron jets being pulled out into the vacuum and pushed back inside the plasma during one

cycle. On top of this oscillating motion, the plasma surface is pushed inside by the ponderomotive force of the laser pulse,

$$\mathbf{F}_p = -m_e c^2 \nabla \left(1 + \langle \mathbf{A} \rangle^2\right)^{1/2} \quad , \tag{2.37}$$

where $\langle \mathbf{A} \rangle$ is the cycle-averaged vector potential of the incident laser pulse [62]. This can be seen as a cycle-averaged motion of the plasma surface away from the driving laser pulse. This effect is called surface denting and can affect the high harmonic generation. One has to distinguish between the electron and ion denting. Initially, only the electrons will be pushed inward; the ions follow due to the electrostatic potential on a longer time scale. As the interaction is confined to the short time frame of the laser pulse duration, the main contribution comes from the electron denting. Where it does make a difference, the ion denting will be discussed in the next sections.

Temporal Denting

The temporal surface denting increases over the course of the laser pulse and depends on the temporal shape of the incident pulse only. Therefore, it can be studied with 1D PIC simulations for electron denting and short time scales. At long time scales, the process becomes turbulent [63].
The evolution of the electron density is shown in figure 2.9. At the beginning, the preplasma is steepened and the cycle-averaged critical surface moves inwards with increasing laser intensity. After the peak intensity has passed, the velocity of the inward motion decreases, but does not stop completely. This is because of the ion motion, which becomes relevant on longer time scales in addition to the electron motion. [64]. Due to the motion of the reflective surface away from the incident laser pulse, this leads to a red shift of the harmonics generated later during the pulse. This is visible in the spectrum as a double line structure. The red-shifted part of the radiation appears as a weaker spectral line between the main harmonic lines, as visible in figure 2.10b.
In figure 2.9, a spatio-temporal plot of the density evolution during an interaction with a laser pulse is shown. In addition, as white crosses, the emission points of attosecond pulses are displayed. To determine the emission points from the PIC simulation, the following algorithm has been used:

- An 2D array containing the field amplitudes for every spatial grid point and

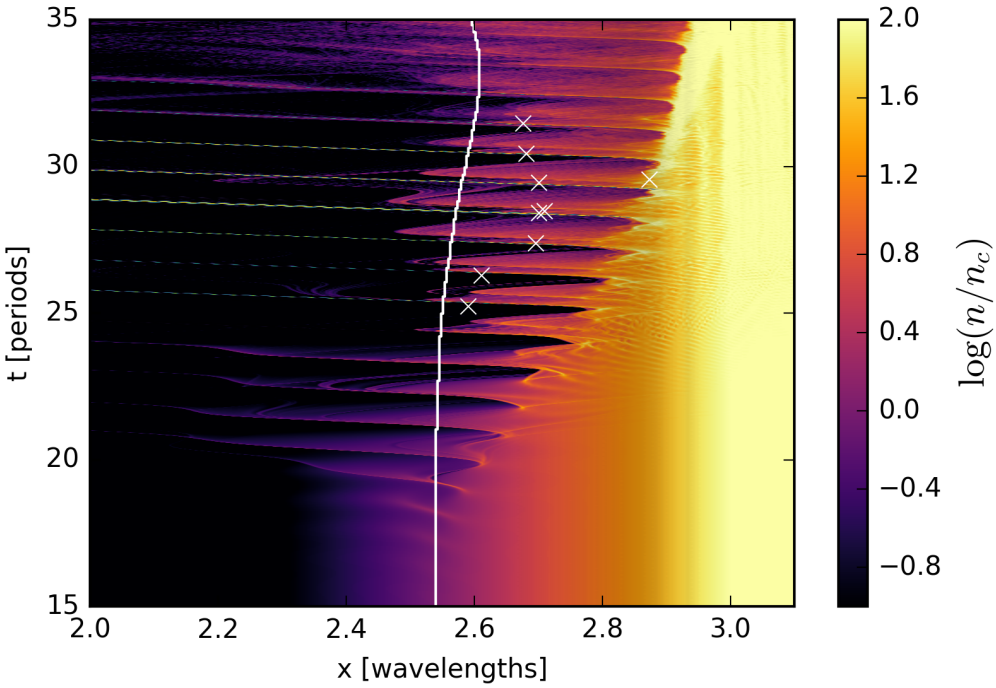

Figure 2.9.: Electron density in logarithmic scale (colours with colour bar), critical ion density ($n_0 = n_c$) surface (white line) and emission points of attosecond pulses (white crosses, computed with the algorithm described in the main text) with the generated AP emissions (green-yellow line). Due to the laser pressure, the initial electron surface is pushed inwards, while the ion density remains largely in place. It is interesting to note that the emission points of the attosecond pulses do not follow the denting of the bulk density, nor the ion motion on the longer time scale. Parameters for the simulation: $a_0 = 8$, $\tau = 8$ cycles (FWHM), angle of incidence $\theta = 45°$, $n_0 = 100n_c$, preplasma scale length $L = 0.8\lambda_L$.

every time step is obtained from the 1D simulation.

- A Fourier transformation in time is performed and a bandpass filter from the 20th to 100th harmonic is applied.

- The time coordinate is transformed from t to retarded time $t + x$. In this coordinate system, the fields propagate along a line parallel to the x axis, as opposed to a 45° angle in the t - x coordinate system. This aids the following computation.

- Each row in the array now corresponds to a light-like path and each AP emis-

sion is stored in one row of the array. The field amplitudes are converted to intensities and a moving average is applied.

- For each row it is checked whether the maximum intensity is above a threshold of at least 10% of the maximum harmonic intensity to exclude any numerical noise. If the row contains a AP, the position where the intensity exceeds a certain threshold of the maximum intensity in that row (in this case, $0.8 \cdot I_{\max}$ was chosen). This position is taken as the emission point of the AP.

- It has been checked that the algorithm is robust against variations of the two threshold parameters. Still, one outlier is detected by the algorithm, which does not have any physical implications.

As expected, APs are always emitted when electron bunches are accelerated towards the laser pulse, but do not follow the denting of the bulk density. While there is a displacement from the second to the third attosecond pulse, the generation depth remains almost constant from there on. The emission points even shift slightly back towards the original surface position. After the peak intensity at the centre of the laser pulse has passed, the laser intensity and hence the laser pressure is lower for later times. Due to the onset of ion motion at that point, the emission points do not reach their original position again.

Spatial Denting

The other significant effect of surface denting is the formation of a curved concave surface. The harmonics reflected from the surface have curved wavefronts and are therefore focused to a position depending on the surface curvature [5, 65]. To investigate the effect of the spatial surface denting, 1D simulations are not sufficient anymore. Instead, a number of 2D simulations have been performed. The laser parameters in this case were $\lambda_L = 800$ nm, $a_0 = 8.0$, $\tau = 25$ fs, a FWHM spotsize of 4μm and the laser is propagating in positive x-direction. The maximum target density was $100n_c$ with a preplasma scale length of $L_p = \lambda_L/10$, rotated by 45° with regard to the incident laser. The target is displayed in figure 2.10 in rotated coordinates

$$x' = x \cdot \cos\theta + y \cdot \sin\theta \tag{2.38}$$

$$y' = y \cdot \cos\theta - x \cdot \sin\theta \tag{2.39}$$

with $\theta = 45°$. The effect of this focusing can be seen in the spectrum (figure 2.10b for a surface which looked like figure 2.10a during the peak of the laser pulse).

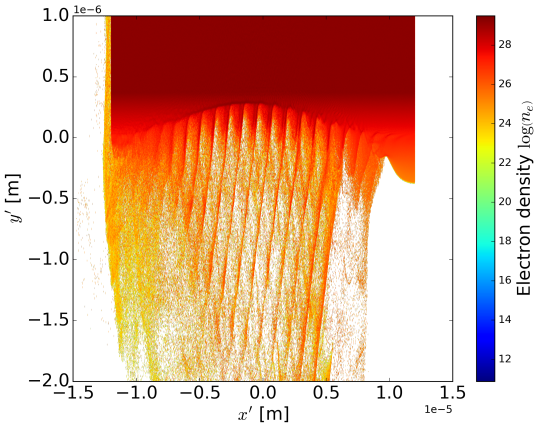

(a) Electron density plot of the initially flat target at the peak of the laser pulse in the rotated coordinate system. Surface denting is clearly visible.

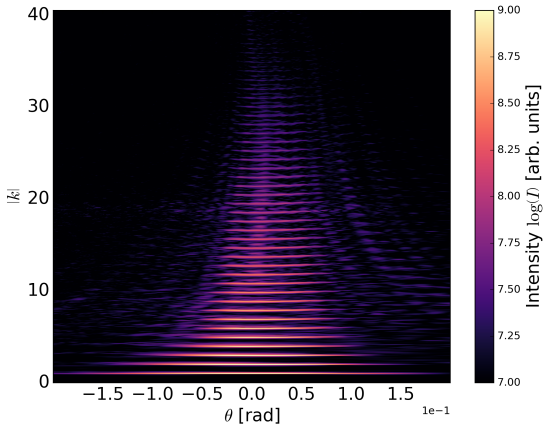

(b) Spectrum of the pulse reflected from the initially flat target. The divergence of the ROM harmonics above the CWE cutoff is nearly constant.

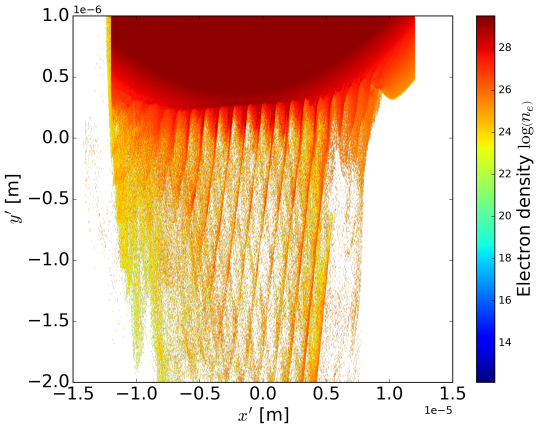

(c) Electron density plot of the preformed target (parameters $D = 100 \cdot 10^{-9}$, $y_s = 2\mu m$, $w_d = 5$) at the peak of the laser pulse in the rotated coordinate system. The preformed density gradient balances the ponderomotive forces of the laser pulse, so the reflective surface remains flat.

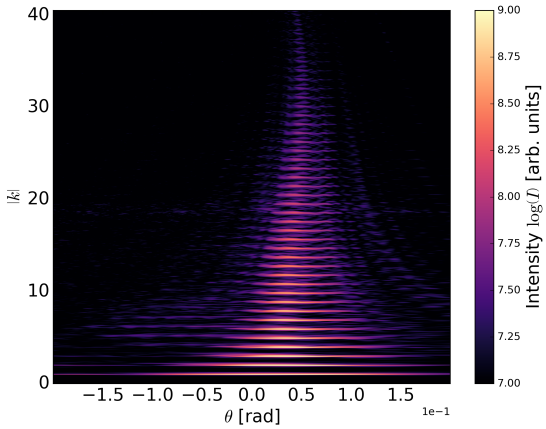

(d) Spectrum of the pulse reflected from the preformed target. The divergence of the ROM harmonics above the CWE cutoff is much smaller and decreases with the wavelength.

Figure 2.10.: Electron density at the peak of the pulse and spectrum obtained after the interaction for a flat surface (**(a)** and **(b)**) and a preformed target (**(c)** and **(d)**). Parameters: $\lambda_L = 800nm$, $a_0 = 8.0$, $\tau = 25fs$, FWHM spotsize of $4\mu m$, maximum target density of $100n_c$ with a preplasma scale length of $L_p = \lambda_L/10$.

The ROM harmonics above the CWE cutoff have an almost constant divergence [65], which is also larger than the divergence expected from a flat surface. The constant divergence of the ROM harmonics can be explained as follows: While the divergence of each harmonic n should scale as $\Theta_n \sim \lambda_n/D_n$ (with D_n the spotsize) under the assumption that they are emitted from the surface with planar wavefronts, the harmonics are instead focused to wavelength dependent spotsizes as they are created with different wavefront curvatures [65]. This leads to a constant divergence far away from the target.

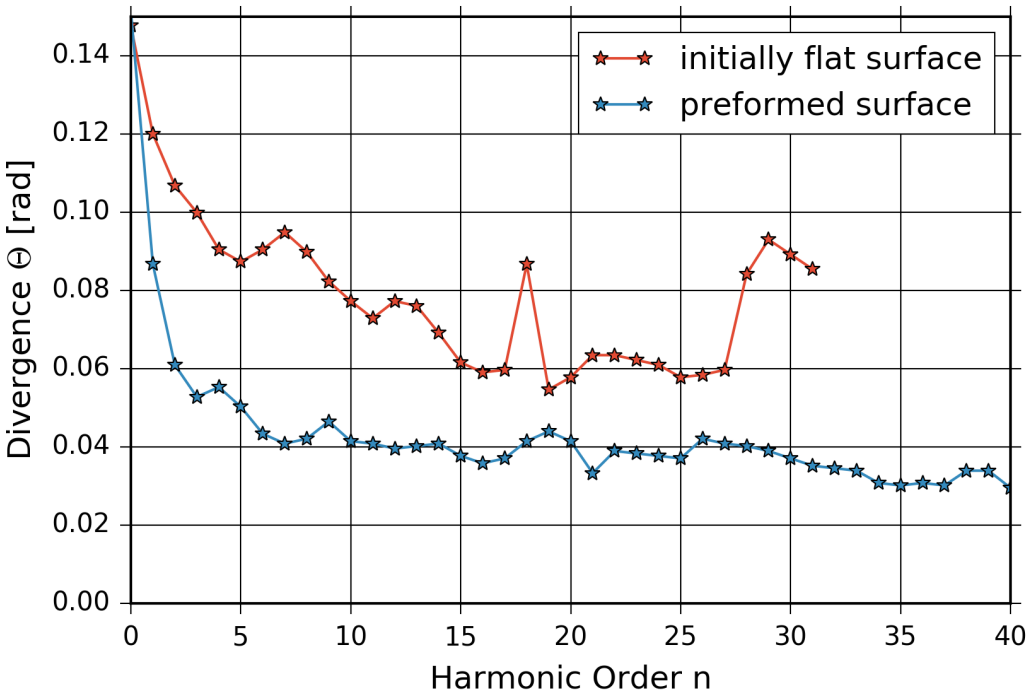

Figure 2.11.: Divergences of the harmonics shown in the spectra in figure 2.10 in dependence of the harmonic order n. In the case of the preformed target, the harmonic divergence is decreasing steadily. In the case of the initially flat target, from the 15th harmonic on the divergence does not decrease further. The data is only shown up to the 30th harmonic, as the low intensity prevented the extraction of any meaningful data above this point. Oscillations in both cases are due to numerical noise in the simulation.

While this coherent harmonic focusing [5] is favourable for some applications, for others like the attosecond lighthouse effect surface denting can have a detrimental effect. The constant, but broad divergence of the ROM harmonics can significantly

reduce the ability to spatially separate individual APs (see chapter 4). Mitigating the effect of surface denting on the divergence can be done in different ways, either by using a super-gaussian laser pulse or by pre-shaping the plasma surface [65]. Here, the latter is discussed in more detail. The exact shape of the induced curvature on the target depends on the spatial profile of the laser intensity. For a Gaussian pulse, it has been shown that the curvature is to good approximation parabolic [60]. Therefore, it is plausible to try a parabolic transverse density distribution to compensate for the surface denting. The preplasma of the target is modelled as an exponential ramp

$$n(x) = n_{max} \exp((\tilde{x} - x_c)/L_p)$$

where

$$x_c = L_p \log(n_{max}/n_c)$$

is the distance between n_{max} and n_c. For a flat target, it is simply $x = \tilde{x}$. To introduce the desired curvature to compensate for the denting, the x coordinate is transformed as

$$\tilde{x} = x - D(y - y_s)^2 (w/w_d)^{-2} \tag{2.40}$$

where w is the target width, y_s an offset in y-direction and D and w_d free parameters defining the curvature.

By performing many 2D simulations, the best combination of parameters for the laser parameters used appeared to be $D = 100 \cdot 10^{-9}$, $y_s = 2\mu m$, $w_d = 5$. A comparison between an initially flat target and a preformed is shown in figure 2.10. First of all, it can be seen from the electron density plot (figure 2.10c), that the surface indeed remained flat throughout the interaction. It is important to note that the target itself is not curved, but it is sufficient that the density gradient has a curvature. The flat surface is confirmed by the properties of the spectrum obtained after the interaction (figure 2.10d). As the harmonics are not focused any more, the divergence of the ROM harmonics are much smaller than in the case with denting and the divergence is not constant, but decreases to shorter wavelengths (figure 2.11).

For completeness, the ion density is shown in figure 2.12. The density distribution largely resembles the initial distribution. Inside the density gradient, where the electron-vacuum-surface is located, charge has built up and so the ion density also shows an imprint from the electron surface denting. Similar to the electron density, it can be seen from figure 2.12b that a preformed plasma can be used to produce a

flat surface during the interaction.

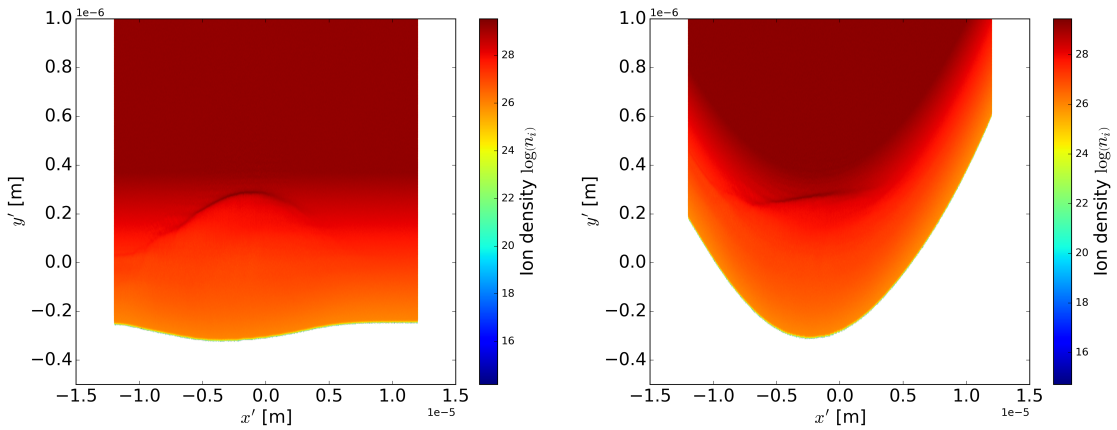

(a) (b)

Figure 2.12.: Ion density at the peak of the pulse for a initially flat surface **(a)** and a preformed target ($D = 100 \cdot 10^{-9}$, $y_s = 2\mu m$, $w_d = 5$) **(b)**. As expected, the ions stay in place due to their higher inertia. Only where the electron-vacuum surface is located (see figure 2.10c), the ion density is increased. The white area around the target represents a density of 0. Parameters: $\lambda_L = 800nm$, $a_0 = 8.0$, $\tau = 25fs$, FWHM spotsize of $4\mu m$, maximum target density of $100n_c$ with a preplasma scale length of $L_p = \lambda_L/10$.

2.7.4. Gating of Single Attosecond Pulses

In order to drive the SHHG generation using the ROM mechanism, a laser pulse with an intensity of at least 10^{18} W/cm^2 is needed. To the present date, all laser systems which can provide such an intensity produce a laser pulse with at least a few cycles [32]. In general, a multi-cycle incident laser pulse will lead to the generation of a train of APs. For possible future applications of those APs, it would be beneficial to be able to isolate a single AP from the pulse train, for example to facilitate time-resolved pump-probe experiments [51].

Therefore the need arises for gating techniques, which allow the separation of APs either in time or space. Several techniques have already been proposed and shown to work in experiments.

Polarization Gating [30, 66, 67] relies on the fact that only a linearly polarized laser pulse can generate harmonics [25]. In circular polarization, the target is pushed inwards by the ponderomotive force, but no fast oscillations with the laser frequency

occur. By superimposing two circularly polarized laser pulses, one clockwise, one anti-clockwise, it is possible to create a short linearly polarized gate, which limits the harmonic generation process to a few cycles of a many-cycle laser pulse [68]. The downside of this scheme is that only a small fraction of the incident pulse energy contributes to the harmonic generation process.

With the attosecond lighthouse effect, it is possible to separate APs in space. By introducing a WFR in focus, the individual APs are emitted under different angles, allowing a spatial separation far away from the target [48, 69]. The attosecond lighthouse is discussed in more detail in chapter 4 in the context of angular streaking.

Intensity gating relies on a few-cycle pulse, which is still intense enough to drive SHHG. Such pulses are already available and have been shown to generate pulse trains as short as two or three individual APs [70]. In the next chapter, it is explained how such few-cycle pulses are able to produce a single AP by carefully choosing the carrier-envelope phase (CEP) of the incident pulse.

3. Density and Scalelength Dependent Carrier-Envelope Phase Effects in Attosecond Pulse Generation

The SHHG using the ROM mechanism is able to generate intense and ultrashort ($\approx 1-10$ as) XUV pulses, which would potentially enable pump-probe experiments with a purely laser driven radiation source. To perform time resolved XUV imaging, it would be highly beneficial to generate isolated APs from SHHG sources. Current laser facilities are able to provide few-cycle laser pulses which are intense enough for SHHG [32, 70], but even a few-cycle laser pulse will lead in general to the generation of a attosecond pulse train. The demand leads to the development of different techniques for temporal pulse isolation [51, 67]. In this chapter, it is shown that the number of APs generated from an incident few-cycle laser pulse depends on the carrier-envelope phase (CEP) of the incident pulse and the density and form of the plasma gradient of the target. It is demonstrated that with the right CEP, it is possible to generate an isolated AP from a four-cycle incidence pulse.

It is important to note that the shape of a few-cycle pulses changes significantly with the CEP [71]. The two extreme cases, separated by a CE phase difference of $\pi/2$, are shown in figure 3.1. The shape with a single maximum in the centre of the pulse is called a "cosine" pulse, while the so-called "sine" pulse has two peaks of equal strength. Intuitively, one would assume that a "cosine" pulse would be better suited to generate a single bright AP. Counter-intuitively, for SHHG the sine pulse is able to produce an isolated AP. To understand this effect, the interaction of the laser pulse with the plasma target is studied by examining the fields at the plasma-vacuum boundary for the sub-relativistic, relativistic and ultra-relativistic case.

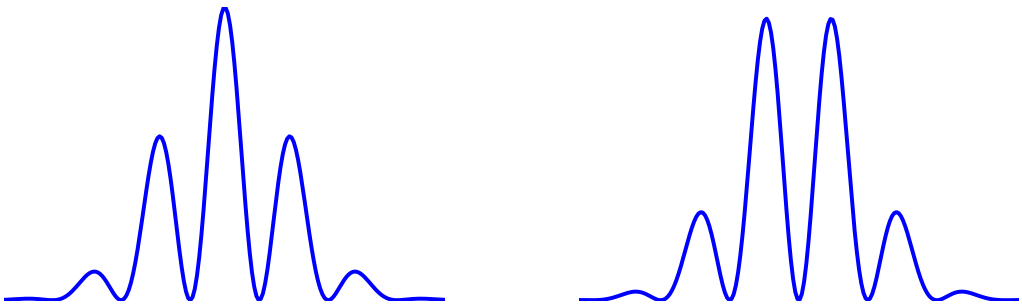

(a) "cosine" pulse (b) "sine" pulse

Figure 3.1.: Two possible shapes of the intensity over time of few-cycle pulses.

3.1. Sub-relativistic case

An incident electromagnetic wave is reflected from a conductor, i.e. a metal or a plasma, at the vacuum surface. The reflected wave has a phase shift of π with regard to the incident wave [72]. In case of a theoretical perfect conductor with infinite electron density, the skin depth of the evanescent wave is infinitely short and the incident and reflected field at the surface will cancel completely. For a realistic conductor with a certain fixed density n_e (i.e. a plasma), the evanescent field depends on the electron density as $\propto \exp(-1/\omega_p)$. As a result, the reflected wave has a phase shift slightly different from π and the fields at the surface do not cancel exactly anymore.

Here, the field at the surface of the plasma in case of a static position of the plasma-vacuum boundary and a laser pulse in normal incidence is derived. This is also the field which acts on the surface electrons for low incident intensities ($a_0 < 0$). The case of relativistic intensities is investigated with the help of PIC simulations in the following sections. For this analytic model, a pre-ionized overdense ($n_e \gg n_c$, with n_c the critical density) plasma slab occupying the positive half-space ($x \geq 0$) is assumed. The plasma slab acts as a perfect conductor, which reflects a linearly polarized relativistic laser pulse incident normally from the negative half-space.

For the following derivation, relativistic units [1] are used. On the vacuum-plasma boundary the incident wave is given by $A_{\text{inc}} = -a_0 \sin(t - x + \varphi_0)$, the reflected wave by $A_{\text{refl}} = -a_r \sin(t + x + \varphi_r)$ and the evanescent wave by $A_{\text{t}} = -a_t \sin(t + \varphi_t) f(x)$ Here, $f(x)$ is the function describing the decay of the evanescent wave inside the

[1] See appendix for an exact definition of units.

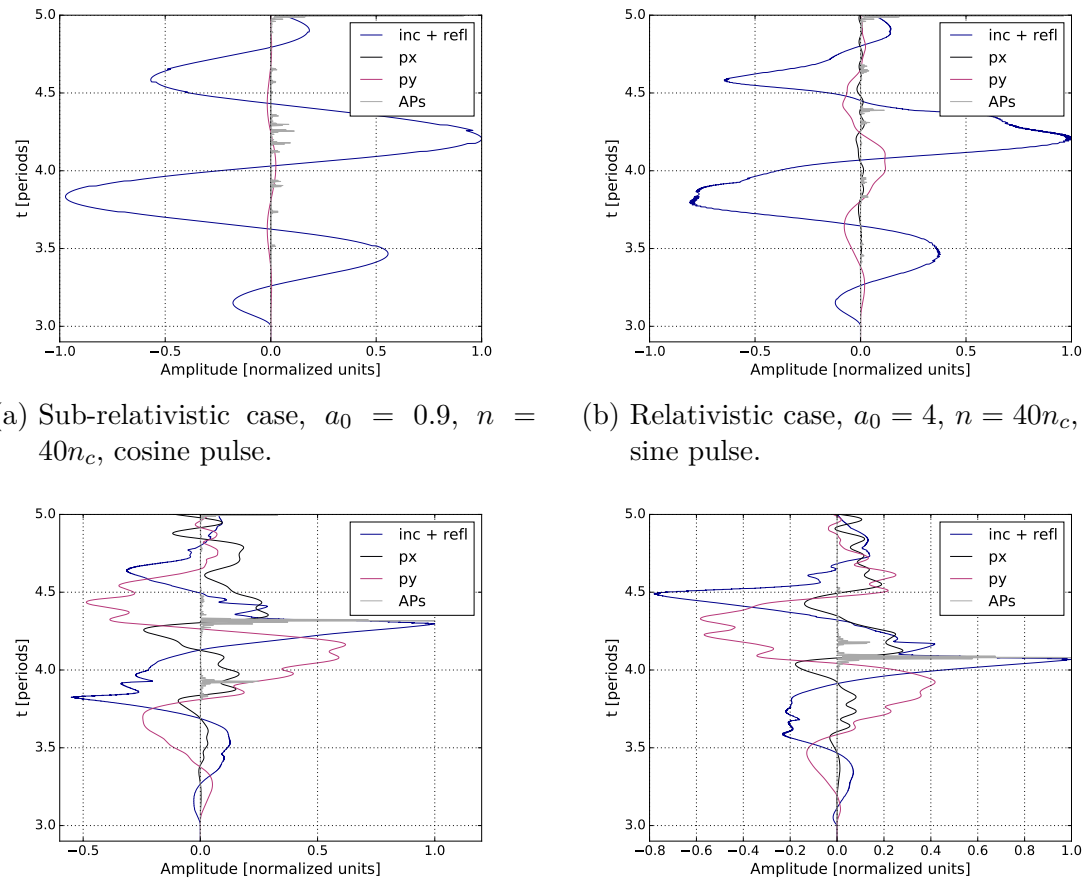

(a) Sub-relativistic case, $a_0 = 0.9$, $n = 40n_c$, cosine pulse.

(b) Relativistic case, $a_0 = 4$, $n = 40n_c$, cosine pulse.

(c) Ultra-Relativistic case, $a_0 = 20$, $n = 80n_c$, cosine pulse.

(d) Ultra-Relativistic case, $a_0 = 20$, $n = 80n_c$, sine pulse.

Figure 3.2.: To understand the different regimes (sub-relativistic, relativistic and ultra-relativistic), it is instructive to visualize the superposition of the incident and reflected field at the plasma-vacuum boundary, the generated attosecond pulses as well as the particle momentum in one figure.

plasma, which is derived later. The boundary condition at the surface yields

$$-a_0 \cos(t - x + \varphi_0) + a_r \cos(t + x + \varphi_r) = -a_t \cos(t + \varphi_t) f(x) \tag{3.1}$$

for the electric and

$$a_0 \cos(t - x + \varphi_0) - a_r \cos(t + x + \varphi_r) = -a_t \sin(t + \varphi_t) f'(x) \tag{3.2}$$

for the magnetic field, where $f'(x) = \dfrac{\mathrm{d}f(x)}{\mathrm{d}x}$. After subtracting the two equations,

"3.2 - 3.1", one arrives at the equation

$$a_0 \cos\left(t - x + \varphi_0\right) = a_t \sin\left(t + \varphi_t\right)\left(f(x) - f'(x)\right) \quad . \tag{3.3}$$

With the relation $a\sin(x) - b\sin(x) = c\sin(x+\alpha)$ with $c = \pm\sqrt{a^2+b^2}$ and $\alpha = \arctan\left(-\frac{b}{a}\right)$, one can rewrite 3.3 as

$$a_0 \cos\left(t - x + \varphi_0\right) = a_t \sqrt{f^2(x) - \left(f'(x)\right)^2} \sin\left(t + \phi_t + \alpha\right) \tag{3.4}$$

with

$$\alpha = -\arctan\left(\frac{f'(x)}{f(x)}\right) \tag{3.5}$$

the relative phase between the incident field and the field at the boundary. Without loss of generality, one can choose the boundary to be at $x = 0$. One obtains the equation for the phase shift,

$$\phi = \arctan\left(\frac{f'(0)}{f(0)}\right) \quad . \tag{3.6}$$

To derive the function $f(x)$, one has to solve the wave equation

$$\frac{\partial^2 a}{\partial t^2} - \frac{\partial^2 a}{\partial x^2} = -n(x)a(x,t) \tag{3.7}$$

for $x > 0$, i.e. inside the plasma. The solution is obtained by applying a Fourier transform, yielding

$$\frac{\partial^2 \tilde{a}}{\partial x^2} = \left(n(x) - \omega^2\right)\tilde{a} \tag{3.8}$$

with $\tilde{a} = \int_{-\infty}^{\infty} a(x,t)\exp(i\omega t)\mathrm{d}t$. For a step-like density profile $n(x) = n_0\Theta(x_0)$ with the density step at x_0, (3.8) is easily solved with the continuity boundary condition at x_0. The specific solution of interest is

$$\tilde{a}(x) = \exp\left(-x\sqrt{n_0 - \omega^2}\right) \tag{3.9}$$

which leads to a phase shift of

$$\varphi = -\arctan\left(\sqrt{\omega_p^2 - 1}\right) \quad , \tag{3.10}$$

where $n_0 = \omega_p^2$ is substituted for the plasma frequency of the target.

To confirm this simple model, the field at the vacuum-plasma boundary has been obtained from 1D PIC simulations for different densities. The laser pulse peak amplitude in both simulations was $a_0 = 0.9$ to remain in the sub-relativistic regime. Due to the low intensity, the plasma surface remained approximately flat throughout the simulation and hence no harmonics are being generated.
There is a phase shift between the incident and reflected light, which depends on the density of the target (figure 3.3a). The superposition of incident and reflected field gives rise to CEP shift of approximately $\pi/2$ relative to the incident pulse for both densities, with the shift closer to $\pi/2$ for $200n_c$ as predicted by the model. The density dependent phase shift for typical target densities (in this case, $n = 40n_c$ and $n = 200n_c$) is sufficient to change the pulse shape from the incident cosine to a sine pulse for the combined incident and reflected fields. Note that negligible surface denting is present in this case.

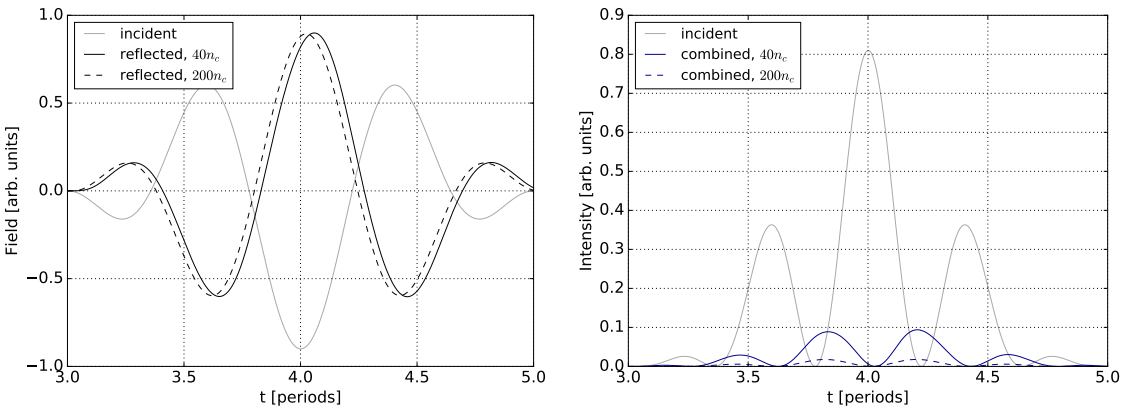

(a) (b)

Figure 3.3.: Fields **(a)** and intensity **(b)** of incident (grey), reflected (black) and combined (blue) field at the plasma-vacuum boundary for the non-relativistic case for two different densities ($40n_c$ and $200n_c$). In both cases, the intensity of the incident pulse was $a_0 = 0.9$, normal incidence.

3.2. Relativistic case

In the relativistic case, where $a_0 > 1$, but $a_0 \lesssim 10$ (this is the range for most experiments to date), the plasma-vacuum-boundary is no longer at a fixed position, but oscillates due to the non-linear laser-plasma interaction. In order to obtain the fields driving the electrons, the position of the critical density surface (white line in figure 3.4b), where the incident laser pulse is reflected, has been calculated and the incident as well as the reflected field obtained at these position in space and time.

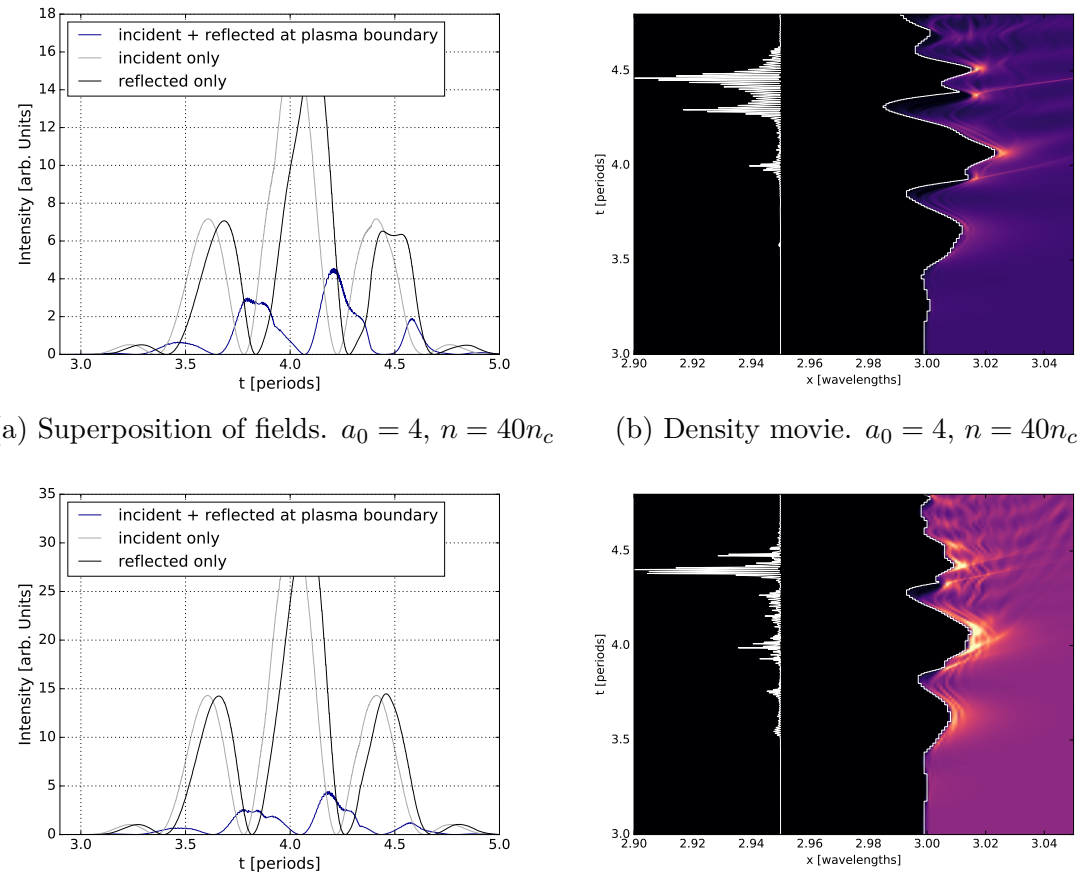

(a) Superposition of fields. $a_0 = 4$, $n = 40n_c$

(b) Density movie. $a_0 = 4$, $n = 40n_c$

(c) Superposition of fields. $a_0 = 5.65$, $n = 80n_c$

(d) Density movie $a_0 = 5.65$, $n = 80n_c$

Figure 3.4.: Simulations for the relativistic case. Superposition of incident + reflected pulse at the critical density (left) and evolution of the target density and position of the critical density (white line) throughout the simulation (right) for two different parameter sets, where $a_0/\sqrt{(1+n)} = \text{const.}$ The white line in the right column depicts the intensity of the filtered attosecond pulses.

The fields are shown in figure 3.4a. Compared to the non-relativistic case, the waveform, especially of the driving fields (blue), shows distortions. This is due to the non-linear interaction of the relativistic laser pulse with the plasma, which eventually leads to the emission of APs. The CE phase shift of the driving fields relative to the incident field is still clearly visible. This behaviour remains the same for different intensities and target densities, as long as the magnitude of the driving field, $a_0/\sqrt{(1+n)}$ stays approximately the same. In this regime, some low intensity APs are generated at the positions where $p_y = 0$, as the electrons gain momentum in p_x due to the $\mathbf{v} \times \mathbf{B}$ of the incident laser pulse and the electrostatic restoring force. However, the surface oscillation depth is still too shallow to generate intense APs.

3.3. Ultra-relativistic case

For even higher intensities with $a_0 \gg 1$, the interaction enters the ultra-relativistic regime. In this case, the driving field at the plasma-vacuum boundary is no longer sinusoidal, but highly distorted and does not clearly show a CE phase shift any more. This coincides with strong oscillations of the plasma surface due to the significant $\mathbf{v} \times \mathbf{B}$ force of the laser pulse at these intensities.

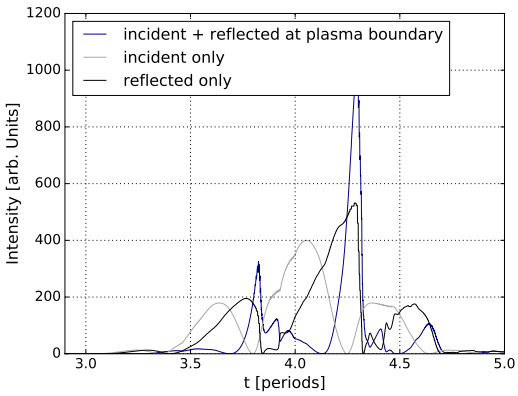

(a) Superposition of incident + reflected pulse at the critical density (white line in (3.5b)).

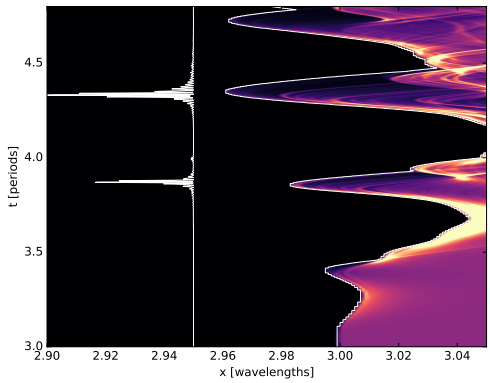

(b) Evolution of the target density and position of the critical density (white line) throughout the simulation.

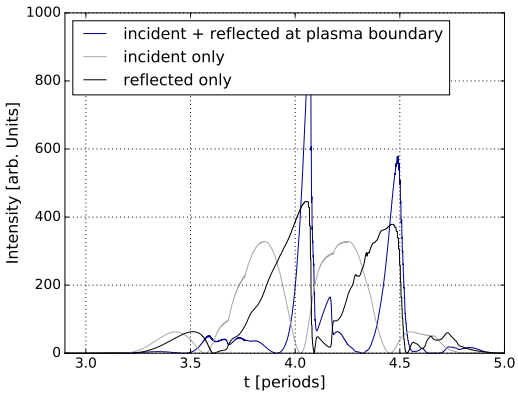

(c) Superposition of incident + reflected pulse at the critical density (white line in (3.5d)).

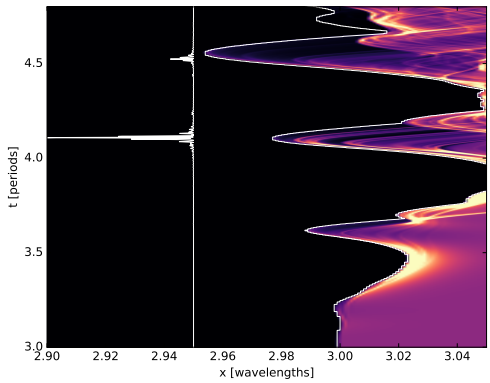

(d) Evolution of the target density and position of the critical density (white line) throughout the simulation.

Figure 3.5.: Simulation for the ultra-relativistic case with cosine incident pulse ((a) - (b)) and sine pulse ((c) - (d)). $a_0 = 20$, $n = 80n_c$, normal incidence

The APs are generated when electrons are accelerated towards the laser pulse by the electrostatic restoring force (when the momentum p_x towards the laser pulse

achieves its maximum). For the restoring force to accelerate the electrons, they have had to be pushed inward by the $\mathbf{v} \times \mathbf{B}$ in the (half-)cycle before. This creates a "memory effect", which requires two intense cycles in succession in order to produce one intense AP.

In a cosine pulse, the peaks adjacent to the maximum are intense enough, that two APs are generated during the interaction. The intensity of the incident pulse and thus the intensity at the plasma-vacuum-boundary is different at the two emission points, the intensity of the two APs is not completely equal, as one would expect if the effect would be purely because of the CEP shift. In case of the sine pulse, the contrast between the two main peaks and and trailing peaks is larger, hence only the two main peaks contribute to the AP generation and only one strong AP is generated.

3.4. Consequences for SHHG with few-cycle laser pulses

In this section, it is examined which consequences the previously described density dependent phase shift has for the generation of attosecond pulses (APs) in SHHG using few-cycle laser pulses. If not noted otherwise, the incident laser pulse in the simulations was linearly polarized, 4 cycles long and had a $\sin^2$ envelope, a peak amplitude of $a_0 = 20$ and an angle of incidence $\theta = 0°$ (normal incidence). The focus was on the XUV emission generated by the ROM mechanism, as this generates higher harmonics and, due to better behaved spectral phase [73], is predicted to result in shorter attosecond pulses than the Coherent Wakefield Emission [23] (CWE) process. The reflected pulse is filtered from $40\omega_L$ to $100\omega_L$.

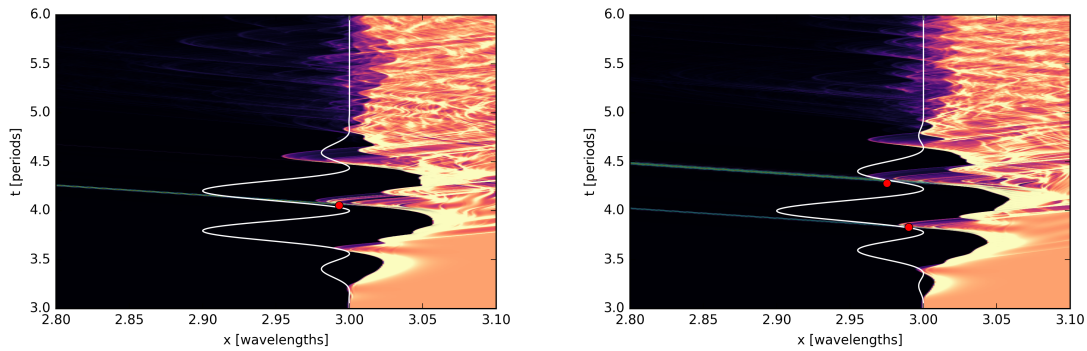

(a) sine pulse (b) cosine pulse

Figure 3.6.: Attosecond XUV pulses generated by a 3-cycle incident pulse with $a_0 = 20$ normally incident on a step-like target with $n_e = 80n_c$. The reflected XUV pulses have been filtered from the 40th to the 100th harmonic to exclude any CWE harmonics. The orange-purple colourscale shows the evolution of the target density, the yellow-green colour the emission of the reflected XUV pulses. Red dots denote the emission points of the APs. For reference, the incident pulse shape is shown as a white line. A single XUV pulse is generated only in case 3.6a, despite the incident pulse having two maxima.

For a step-like pre-ionized density profile with an electron density of $n_e = 80n_c$ the results are shown in figure 3.6. In figure 3.6 (b), the incident pulse was a cosine pulse of the type that is used to generated isolated attosecond pulses in gases (with one well defined maximum with two identical half cycles either side). Contrary to the expectation one might have from the gas target case, two bright XUV pulses

were obtained in reflection. Yet when a sine pulse was incident on the target, only a single attosecond pulse was emitted in the simulation (figure 3.6a)), contrasting with gas harmonics where this pulse shape leads to the emission of two identical attosecond pulses.

This behaviour can be understood as follows. The emission of a bright attosecond pulse occurs, when the longitudinal velocity of the electrons has its maximum. This coincides with the transverse electrical field changing sign [59]. According to equation 3.10, the expected carrier-envelope phase shift between the incident pulse and the oscillation of the surface electrons is for this target $\phi \approx 1.558 \approx \pi/2$, as explained in section 3.1. The same is true for the opposite case of a pulse with one distinct maximum, where two bright XUV pulses are emitted. This is counterintuitive from what is known from gas harmonics. Due to the low density of gases and the different harmonic generation process, this behaviour can only be observed in surface high harmonic generation.

3.4.1. Preplasma

In case of a linear density ramp in front of a region with constant density, simulations were performed to determine the optimal CEP for a given preplasma length. The optimal CEP value is defined by the best contrast between the main pulse, the pre pulse and the trailing pulse to achieve optimal isolation of the single attosecond pulse.

For two different preplasma scale lengths, $\lambda_L/10$ and $\lambda_L/5$, the reflected XUV pulse structures in dependence of the CEP value are shown in figure 3.7 (top row). One can see that the contrast between the main pulse and the leading and trailing pulses changes rapidly with the CEP. Depending on the scale length, different CEP values provide the best contrast. From the simulations, we determined that the best contrast is achieved for a CEP value of 1.2 for a scale length of $\lambda_L/10$ and 0.7 for a scale length of $\lambda_L/5$. For these values, depicted as red planes, the corresponding lineouts are shown below. Note that the interplay between CEP and the target density is complex, displaying many oscillations.

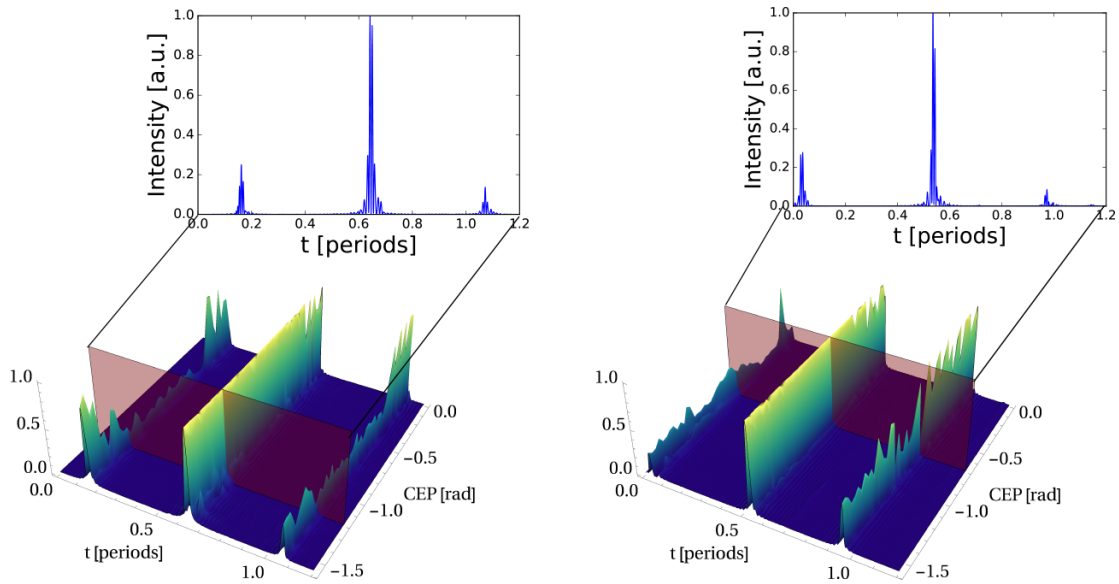

Figure 3.7.: Reflected radiation for different preplasma scale lengths and different CEP values of the incident 3-cycle, $a_0 = 20$ laser pulse. In the left panel, the scale length of the linear preplasma was $\lambda_L/10$, in the right panel $\lambda_L/5$. Each line parallel to the t axes is obtained from one PIC simulation and normalized to the maximum intensity obtained from that simulation. The optimum CEP values, 1.2 for a scale length of $\lambda_L/10$ and 0.7 for a scale length of $\lambda_L/5$, are shown as red planes and as lineouts below.

3.5. Conclusions

In conclusion, it has been shown analytically and with PIC simulations, that the ideal Carrier-Envelope-Phase required to generate single attosecond pulses from Relativistically Oscillating mirrors is non-trivial. When compared to harmonic generation from gaseous media, the behaviour is counterintuitive, in that a so-called sine-shaped incident laser pulse with two intensity maxima of equal strength produces a single attosecond pulse from a step-like overdense plasma target.

The reason for this behaviour across all intensity regimes is a phase shift between incident laser pulse and the electromagnetic field driving the motion of the surface electrons with higher order effects coming into play at highest intensities. This phase shift depends on the density of the plasma target and the length of the preplasma. Thus, the conditions for generating the brightest attosecond XUV pulse, namely a high transverse momentum of the electrons and a high velocity antiparallel to the incident pulse, are only met once during the interaction despite the incident pulse

exhibiting two equal intensity peaks.
For a plasma target with preplasma, a parameter scan using 1D PIC simulations have been used to determine the optimal CEP for a given preplasma length, showing complex interplay between the plasma oscillations and the driving laser. The results demonstrate that both CEP and plasma density distribution have to be carefully taken into account in experiments on generation of single attosecond pulses from the SHHG.

4. Angular streaking of an attosecond pulse train

It is an important problem to isolate a single attosecond pulse (AP) from a train of APs generated from surface high harmonic generation [51, 67]. As with current laser technology, it is impossible to create a single cycle laser pulse, which is still intense enough to drive high harmonic generation. Therefore, there is a need for techniques gating single APs.
In principle, two different approaches are possible: Either by temporal separation (discussed in chapter 3) or by angular or spatial separation. The attosecond lighthouse effect is a method to angularly separate attosecond pulses [48]. This is achieved by introducing a pulse front tilt (PFT) before focussing the incident laser pulse, which translates to a wave front rotation (WFR) in focus, where the target surface is located under an angle of 45°. In turn, the individual APs of a pulse train are emitted under different angles. Far away from the target, this can lead to a spatial separation. This effect has been demonstrated both theoretically [48] and experimentally [69]. In this chapter, the influence of spatial surface denting (see section 2.7.3) on the attosecond lighthouse effect is investigated.

4.1. PIC simulations of the Attosecond Lighthouse

As a first step, the laser pulse with the required spatial-temporal couplings (STCs) has to be implemented in the EPOCH PIC code [31]. Starting from the electric field with a pulse-front tilt before focus (see also section 2.5),

$$E(x,t) = E_0 \exp\left(-2\frac{x^2}{w_i^2} - 2\frac{t^2}{\tau^2} + 4\frac{\xi x t}{\tau^2}\right) \quad , \tag{4.1}$$

where w_i is the beam diameter before focus, τ the pulse duration and ξ the spatio-temporal coupling constant. Then, the focussing of the beam with a focal length f

is modelled using a Fourier transform in x, yielding a field $\tilde{E}(k,t)$. With the relation $k = k_L x_f / f$ with $k_L = 2\pi/\lambda_L$, one obtains [48]

$$\tilde{E}(x_f,t) \propto \exp\left(-2\frac{t^2}{\tau_f^2} - 2\frac{x^2}{w_f^2}\right)\exp\left(i4\frac{w_i\xi}{w_f\tau_f\tau}xt + i\omega_L t\right) \quad , \tag{4.2}$$

where $\tau_f = \tau\sqrt{1+(w_0\xi/\tau)^2}$ and $w_f = w_0\sqrt{1+(w_0\xi/\tau)^2}$ the pulse duration and beam waist in focus, respectively. Here, w_0 is the beam waist in focus without the STCs. The instantaneous propagation direction $\beta(t) = \dfrac{\partial\Im\{E(x_f,t)\}}{k_L\partial x_f}$ is time depended and taking the derivative with respect to time yields the wavefront rotation velocity [48]

$$\frac{\mathrm{d}\beta}{\mathrm{d}t} = v_r = \frac{w_i^2}{f\tau^2}\frac{\xi}{1+(w_i\xi/\tau)} \quad . \tag{4.3}$$

Note that ξ is measured in fs/mm, whereas v_r is measured in mrad/fs. The rotation velocity is maximized for a value of $\xi_0 = \tau/w_i$, as in this case the whole divergence angle is streaked during one pulse duration. This value is being used for all simulations in this chapter, except noted otherwise.

The difficulty in implementing this in EPOCH was the need for a analytic expression for the electromagnetic field at the boundary of the simulation box, which then leads to the desired field distribution in focus. Using the Kostenbauder matrix formalism [45, 47], one can derive the coefficients for the general envelope function $E(x,t) \propto \exp\left(Q_{xx}x^2 - Q_{tt}t^2 - 2Q_{xt}xt\right)$. These coefficients are known in focus, $Q_{\mathrm{xx}} = -\dfrac{1}{w_f^2}$, $Q_{\mathrm{tt}} = \dfrac{1}{\tau_f^2}$ and $Q_{\mathrm{xt}} = i\dfrac{\pi}{\lambda_L}v_r$. According to the formalism [45], the input parameter is then

$$Q^{\mathrm{in}} = i\frac{\lambda_L}{\pi}\begin{bmatrix} Q_{\mathrm{xx}} & Q_{\mathrm{xt}} \\ -Q_{\mathrm{xt}} & Q_{\mathrm{tt}} \end{bmatrix}^{-1} \tag{4.4}$$

and the ray-pulse matrix for a a focussing pulse propagating distance z in free space is [47]

$$K = \begin{bmatrix} A & B & 0 & E \\ C & D & 0 & F \\ G & H & 1 & I \\ 0 & 0 & 0 & 1 \end{bmatrix} = \begin{bmatrix} \frac{z}{R}+1 & z & 0 & 0 \\ \frac{1}{R} & 1 & 0 & 0 \\ 0 & 0 & 1 & 0 \\ 0 & 0 & 0 & 1 \end{bmatrix} \quad . \tag{4.5}$$

Put together, one can compute the output matrix as [45]

$$Q^{\text{out}} = \left(\begin{bmatrix} A & 0 \\ G & 1 \end{bmatrix} Q^{\text{in}} + \begin{bmatrix} B & E/\lambda_L \\ H & I/\lambda_L \end{bmatrix} \right) \cdot \left(\begin{bmatrix} C & 0 \\ 0 & 0 \end{bmatrix} Q^{\text{in}} + \begin{bmatrix} D & F/\lambda_L \\ 0 & 1 \end{bmatrix} \right)^{-1} \tag{4.6}$$

After carrying out this computation with a computer algebra system, the resulting coefficients can finally be obtained from entries of inverted Q^{out} matrix,

$$Q_{xx} = -\frac{1}{w_f^2(1+R(z))} - i\frac{\lambda z}{\pi w_f^2(1+R(z))} \tag{4.7}$$

$$Q_{tt} = \frac{1}{\tau_f} + \left(\frac{z v_r}{w_f}\right)^2 \frac{1}{1+R(z)} - i\frac{\pi z v_r^2}{\lambda(1+R(z))} \tag{4.8}$$

$$Q_{xt} = -\frac{z v_r}{w_f^2(1+R(z))} + i\frac{\pi v_r}{\lambda(1+R(z))} \tag{4.9}$$

where $R(z) = \left(\frac{\lambda z}{\pi w_f^2}\right)^2$.

To verify the simulation setup, a simulation with parameters similar to the ones in [48] has been performed. The resulting distribution of APs are displayed in figure 4.1. In order to be able to see the spatial separation of the APs, they need to be propagated for a significant distance ($\gg z_r$) from the target. As this is not feasible with PIC simulations due to computational constraints, the vacuum propagation technique outlined in [74] is used to obtain the spatial field distribution $240\mu m$ behind the target. After filtering for the high harmonics ($n > 20$), three distinct peaks separated by $2 - 4\mu m$ in the transverse direction can be detected, confirming the spatial separation of the APs.

One effect counteracting the separation is the divergence of the emitted APs. The divergence heavily depends on the depth of the surface denting (see section 2.7.3) and a large divergence has the potential to make it impossible to separate the individual pulses. The other factor with influence on the separation of the pulses is the wavefront rotation velocity v_r, which depends on the beam waist, pulse duration and the coupling constant ξ. In order to maintain the pulse separation, the divergence has to be smaller than the angular separation of the pulses. In [48], this condition is expressed as the equation

$$\frac{\Theta_n}{\Theta_L} \leq \frac{1}{\alpha N_c} \quad , \tag{4.10}$$

where Θ_n is the divergence of the n-ths harmonic, Θ_L the divergence of the incident

laser beam, N_c the number of optical cycles in the laser pulse and α a parameter controlling the required contrast between the APs. This puts a constraint on the maximum harmonic beam divergence of $\Theta_n \leq \frac{\Theta_L}{\alpha N_c}$. For a flat surface with no significant surface denting, the divergence decreases with increasing harmonic order n. Filtering for higher orders can therefore improve the contrast between the APs. As it can be seen from the simulations in section 2.7.3, the divergence of the high harmonics of interest ($n \geq 20$) is constant and much broader when surface denting is present, compared to the case without. It is therefore important to minimize the surface denting to increase the spatial contrast between individual APs.

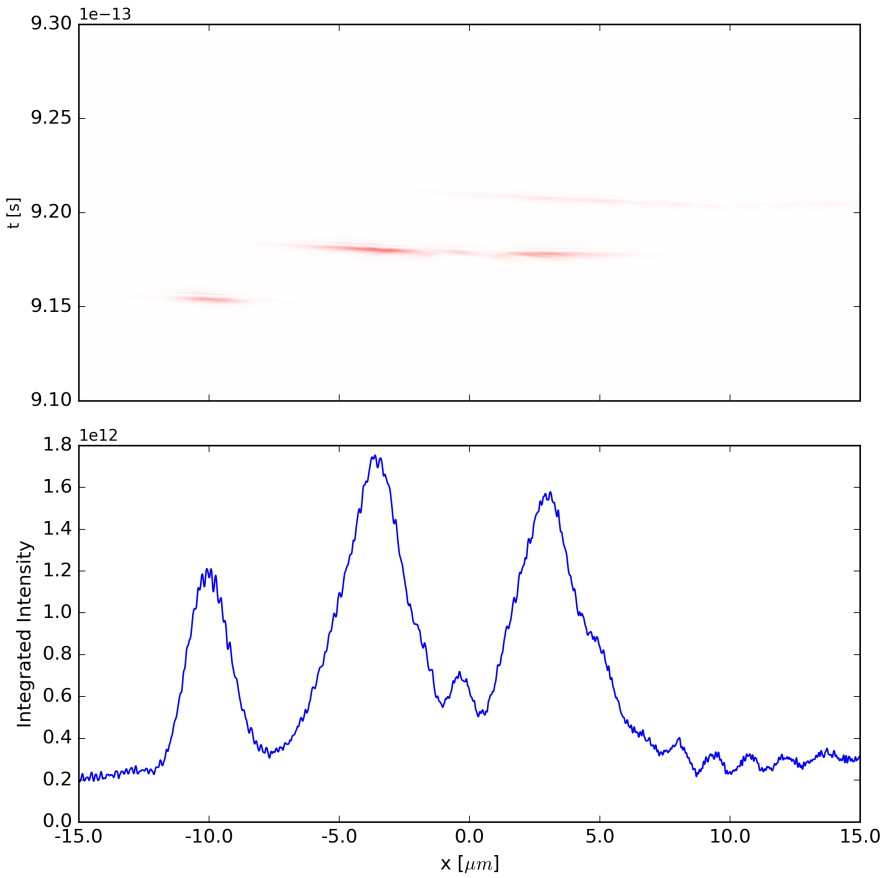

Figure 4.1.: Attosecond pulses, filtered from the 20th to 30th harmonic, obtained in the farfield ($240\mu m$) from the target. The top panel shows the spatial-temporal intensity distribution (colour), the lower panel the time integrated signal a detector would see. Three distinct peaks can be seen, spatially separated by $2 - 4\mu m$.

4.2. Spectral Properties of the Attosecond Lighthouse

The signature of the attosecond lighthouse effect is visible in the reflected spectrum. It can be used to infer properties of the laser-plasma interaction, especially the surface denting or preplasma which was present during the interaction. The spectrum

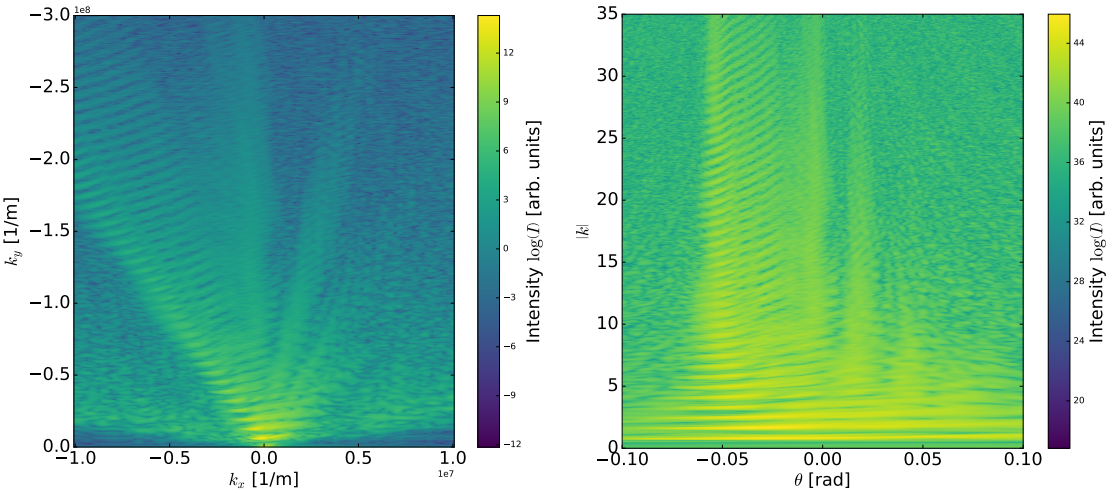

(a) k_x-k_y spectrum of the pulse shown in figure 4.1.

(b) Angular spectrum of the pulse shown in figure 4.1.

Figure 4.2.: The same spectrum viewed in two different spaces. **(a)** the k_x-k_y space directly obtained from a Fourier transform of the pulse from the simulation. **(b)** The angular spectrum obtained after a coordinate transform of **(a)** to polar coordinates.

shown in figure 4.2a is in the k_x-k_y space. This view is particularly useful to visualize which direction a pulse propagates in. A pulse propagating exactly along the y-axis would only have non-zero intensity for $k_x = 0$, with a small spread accounting for the divergence of the pulse. The k_y axis in that case would approximately be defined by central the wavelength ($k_y \approx 1/\lambda_0$).

In the present case, the pulse is mainly propagating in the $-y$ direction, but one can see that it splits into pulses propagating into different x directions ($k_x \neq 0$) for higher harmonics (higher k_y values). This is the effect of the attosecond lighthouse, and the pulses are the APs emitted under different angles. The angle relative to the main propagation direction is simply given by

$$\theta = \arctan\left(k_y/k_x\right) \quad . \tag{4.11}$$

This allows for a graphical check of the constraint given by equation 4.10. The divergence of the APs is visible in this picture as the angular width of the harmonics. If they are broad and overlap with those from the neighbouring AP, equation 4.10 is violated and they can not be distinguished any more as separate pulses far away from the target.

The spectrum obtained from spectrometers in experiments is often in terms of 'angle vs. wavelength'. A nonlinear coordinate transformation to polar coordinates can be used to reproduce this quantities from the k_x - k_y space pictured above:

$$\theta = \arctan(k_y/k_x) \tag{4.12}$$

$$|k| = \sqrt{k_x^2 + k_y^2} \tag{4.13}$$

For convenience, $|k|$ is then further normalized to the fundamental laser frequency $k = 2\pi/\lambda_L$, so it corresponds to multiples of λ_L. In figure 4.2b, the same spectrum as in figure 4.2a is shown in the transformed coordinates. Here, the APs propagating in different directions are visible as vertical lines for different values of θ.

4.3. Angular Streaking

This view is useful for comparisons with experimental data. Experiments conducted by C. Rödel and J. Bierbach at the JETi 40 laser facility in Jena[1] aimed at the angular streaking of the ROM generation process, used the attosecond lighthouse for a different purpose.

With the interaction parameters of the experiment, no separation of the pulses could be observed, but a tilt of the harmonics in the spectrum can be seen (see experimental spectrum in figure 4.3c). To provide an explanation of this result, 2D PIC simulations with a wide parameter range have been performed. They all confirmed the experimental observation, that no separation of APs occurred. The spectrum obtained from a simulation with the parameters $a_0 = 8$, $L_p = \lambda/10$, $n = 90n_c$, angle of incidence $\theta = 45°$ closely resembles the experimental spectrum (figure 4.3). From the simulation it can be concluded that the surface denting, which was not avoidable due to experimental constraints, plays a major role in the separation of the APs.

[1] C. Rödel *et al.*, to be submitted

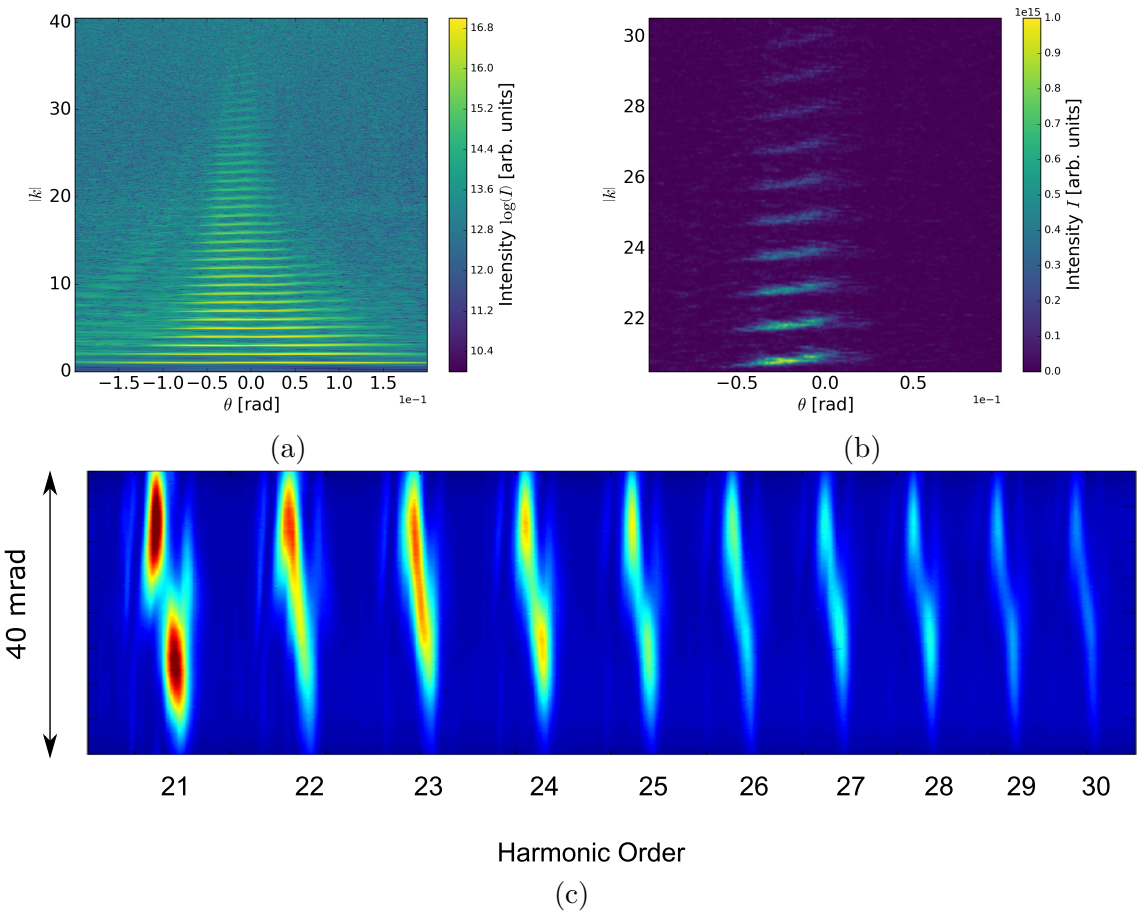

Figure 4.3.: Angular spectrum of the XUV pulse after the interaction with parameters close to the experiment ($a_0 = 8$, $L_p = \lambda/10$, $n = 90n_c$, $v_r = v_{r,\max}$, $\theta = 45°$, spotsize in focus of 1.8 μm). **(a)** full spectrum, logarithmic scale **(b)** spectrum of the 21th-30th harmonic, linear scale. **(c)** experimental spectrum, 21th-30th harmonic, linear scale, with $v_r = v_{r,\max}$ courtesy of *J. Bierbach, C. Rödel et.al.*

The simulated spectrum is shown in figure 4.3a and 4.3b. As the divergence is too broad, no traces of pulse separation are visible in the spectrum.

Nonetheless, it is interesting to examine the spectrum in detail, as it contains information about the depth of the temporal surface denting during the interaction. While the spatial surface denting only affects the divergence, the temporal surface denting leads to a frequency shift, resulting in a double-line structure (see section 2.7.3). The frequency shifts over the course of the pulse, as does the emission angle because of the wave-front rotation. This leads to different frequencies being emitted under different angles, hence the name angular streaking. In the angular spectrum, this

can be seen as a tilt of the harmonics, i.e. an angular spectral chirp. It depends on the wavefront rotation velocity as well as on the temporal surface denting. Both affect the slope of the tilt of the harmonics, where both a higher wavefront rotation velocity and the velocity of the inward moving surface contribute to the tilt.

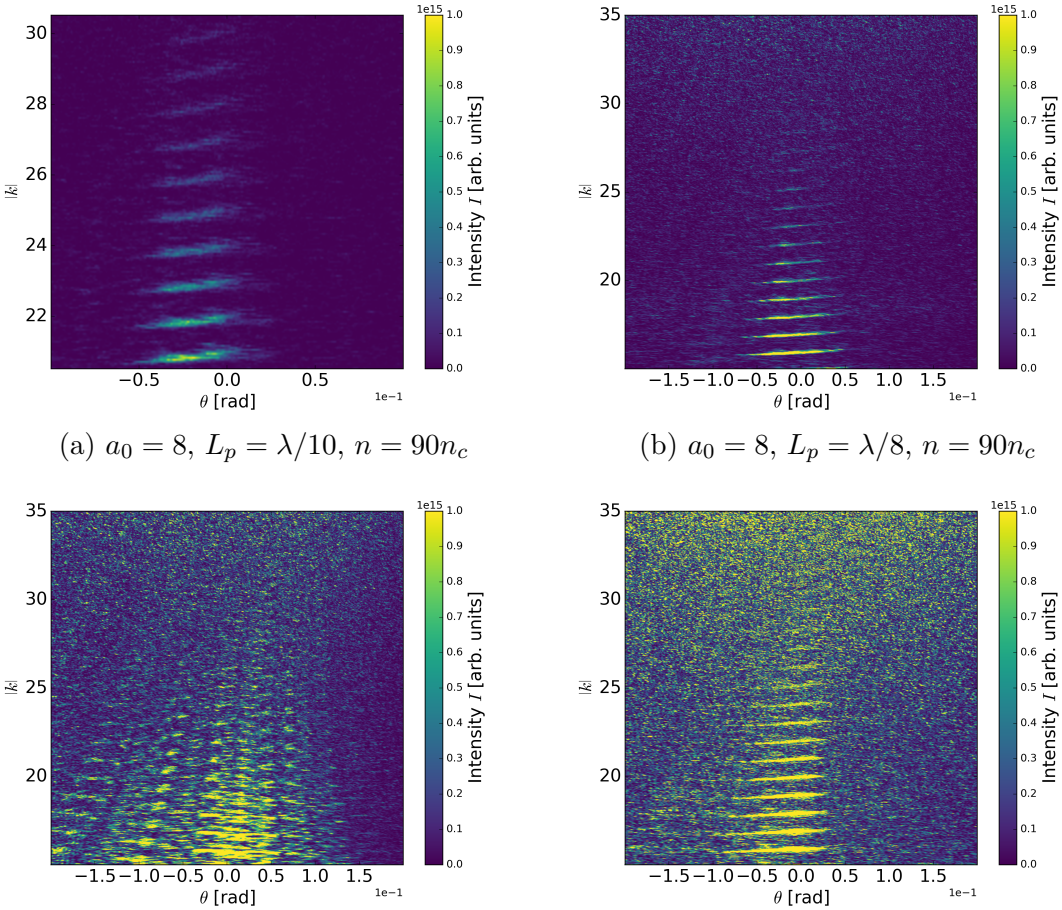

(a) $a_0 = 8$, $L_p = \lambda/10$, $n = 90n_c$

(b) $a_0 = 8$, $L_p = \lambda/8$, $n = 90n_c$

(c) $a_0 = 8$, $L_p = \lambda/5$, $n = 90n_c$

(d) $a_0 = 15$, $L_p = \lambda/10$, $n = 90n_c$

Figure 4.4.: Angular spectrum of the 15th-35th harmonic (linear scale) of the XUV pulse after the interaction with different parameters, each time with maximum wavefront rotation velocity. The tilt of the harmonics depends on the velocity of the reflective surface moving inward during the interaction, causing the surface denting.

If the maximum achievable wavefront rotation velocity is used, the angular spectral chirp can be used to deduce information about the velocity of the temporal surface denting. In order to investigate this, a parameter scan using 2D PIC simulations has been performed. The intensity a_0 and the scale length L_p are varied, so that different surface denting depths and velocities are achieved. The wavefront rotation

Simulation	a_0	L_p	Angular spectral chirp of 15th harmonic
(a)	8	$\lambda/10$	0.02 nm/mrad
(b)	8	$\lambda/8$	0.01 nm/mrad
(c)	8	$\lambda/5$	0.004 nm/mrad
(d)	15	$\lambda/10$	0.01 nm/mrad

Table 4.1.: Angular spectral chirp of the 15th harmonic in dependence of the interaction parameters, a_0 and L_p.

is always maximized with a value of $\xi_0 = \tau_i/w_i$. The spectra are shown in figure 4.4 and in addition, figure 4.5 shows the electron density distribution at the time when the peak of the laser pulse interacts with the target.

It is clearly visible that they differ significantly. In particular, the spectrum in figure 4.4c stands out. This is the simulation with the longest scale length ($L_p = \lambda/5$), showing the largest divergence. This is expected, as the long scale length leads to significant spatial surface denting.

In the other cases, the harmonic lines are well defined, as the harmonic generation in these cases is more efficient. The high harmonic generation was most efficient for $a_0 = 8$ and $L_p = \lambda/10$, with harmonics visible up to the 35th harmonic. In the other cases, the intensity dropped below the simulation noise level around the 25th harmonic. In all cases, the harmonics show an angular spectral chirp, which is different for every set of interaction parameters. To compare the angular spectral chirp across the simulations, the chirp of the 15th harmonic is measured, as it has still a well-defined harmonic line for all parameters considered here. For the cases **(a)** to **(d)** from figure 4.4 the results are shown in table 4.1. The highest angular spectral chirp was achieved for case **(a)** with the shortest preplasma length, leading to the highest velocity of the reflective surface moving inward. In case **(b)** and **(d)**, the angular spectral chirp is the same, despite differing preplasma lengths. The shorter preplasma length of **(d)** is compensated by a higher a_0, so a similar surface denting velocity is achieved. For long preplasma scale lengths in **(c)**, almost no angular spectral chirp could be measured. This can be explained as follows. A long preplasma gradient leads to a steepening of the plasma gradient already at low laser intensities. In the high intensity area of the laser pulse, which contributes most to the high order harmonics, the reflective surface barely moves further inward, leading to a small red shift of the harmonics and therefore to a small angular spectral chirp.

4.4. Conclusions

The attosecond lighthouse effect is a promising method to spatially separate single attosecond pulses in a pulse train by utilising an incident laser pulse with pulse front tilt before focus and wave front rotation in the focus. To be able to separate the pulses, one has to control the divergence of the harmonics by reducing the spatial surface denting. Surface denting increases the divergence of individual APs, which reduces the contrast between the pulses up to the point where no separation is possible anymore.

That was most likely the case in an experiment conducted at the JETI40 laser facility in Jena. PIC simulations were able to reproduce the experimental result and provided confirmation, that surface denting was likely the dominant effect.

Even if there is not any separation possible for the given interaction parameters, the attosecond lighthouse effect can still provide valuable insight into the laser-plasma interaction. With angular streaking, the velocity of the inward moving surface is encoded as an angular spectral chirp in the spectrum of the reflected APs. Here it is shown for the first time that this angular spectral chirp depends on the incident intensity a_0 and the preplasma scale length L_p and is thus a measure for the temporal surface denting velocity of an initially flat target.

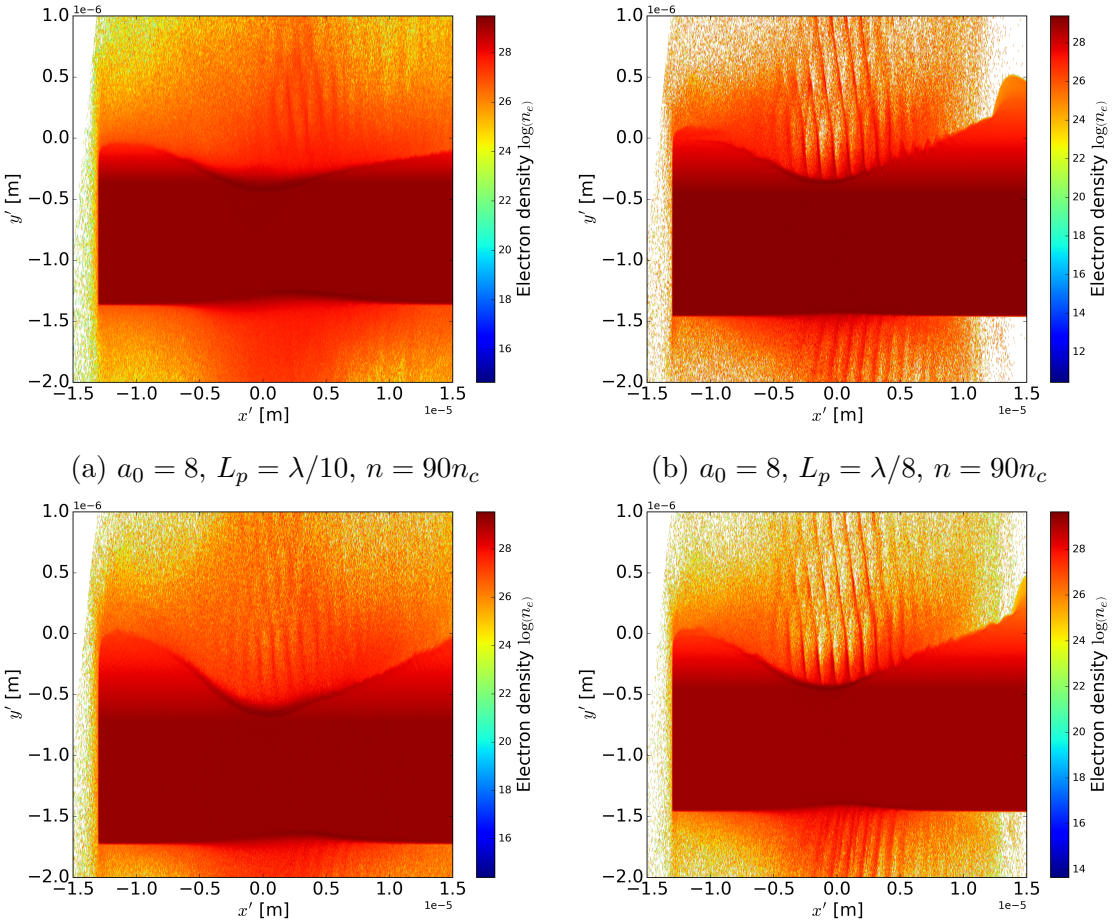

(a) $a_0 = 8$, $L_p = \lambda/10$, $n = 90n_c$

(b) $a_0 = 8$, $L_p = \lambda/8$, $n = 90n_c$

(c) $a_0 = 8$, $L_p = \lambda/5$, $n = 90n_c$

(d) $a_0 = 15$, $L_p = \lambda/10$, $n = 90n_c$

Figure 4.5.: Electron density snapshot of the target when the peak of the pulse interacts with the target for different parameter. The spatial denting is clearly visible in all cases. The simulations with a long preplasma length, especially in 4.5c, exhibit a particular large spatial surface denting depth, explaining the large divergence seen in figure 4.4c. The surface denting depth of 4.5b and 4.5d is almost identical, despite different interaction parameters. Note that the *temporal* surface denting can not be seen in this plots.

5. Efficiency enhancements and propagation effects in multipass high harmonic generation

A long standing challenge of harmonic sources is the efficiency of the high harmonic generation process, where SHHG performs well compared to other approaches. Still, only a tiny fraction of the incident laser intensity is converted into XUV attosecond pulses [14, 75, 76]. Of interest are especially the harmonics above the CWE cutoff with $n \geq 20$ ($\lambda = 40$nm or $E = hc\lambda^{-1} = 31$eV for a incidence wavelength of 800nm). Several methods have been proposed to enhance the generation efficiency, including structured targets [77] or using a mixture of the fundamental and the second harmonic of the incidence beam with a certain phase relation [78], which has been shown to work experimentally [61].

An advanced version of this scheme is to modify the waveform with more than one colour [79], which can be achieved by going over multiple passes [80]. The high order harmonics generated on the first target lead to a steepening of the waveform, which increases the generation efficiency on the second target. This step can in principle be repeated multiple times and with each iteration, the efficiency will increase until it reaches a plateau after 4-6 passes [80], depending on the similarity parameter $S = n_e / (a_0 n_c)$ [5].

The highest increase of efficiency for a ratio of $S = 20$ is seen for two passes, which is also the most feasible case for experiments because of its relative simplicity. Therefore this section concentrates on this case and a laser intensity of $a_0 = 10$ and target density of $n_e = 200 n_c$. These laser parameters are already available at facilities or will be in the near future [32]. All conclusions from this section can be applied to multiple passes in an analogous manner.

The waveform of a multicolour beam is not only defined by its high harmonics and their relative intensity, but also by their relative phase. This relative phase changes

with propagation in vacuum for a focussing beam because of the Gouy phase shift, first described in 1891 [44]. This leads to the conclusion that the distance of two targets in a multipass scheme is relevant for the achievable generation efficiency.
As the second harmonic is the dominant contribution, the effect is illustrated by considering the relative phase between two colours in section 5.1. In section 5.2 and 5.3 PIC simulations of a two-pass scheme are presented, highlighting the importance of choosing a distance where the phase is optimal for the interaction on the second target maximizing the harmonic generation efficiency.

5.1. Gouy Phase effect on multicolour Gaussian beams

Multicolour Gaussian beams are a superposition of Gaussian beams with different central wavelength λ_0, such as those generated during SHHG on overdense targets [24, 25, 51, 56, 57, 59, 81, 82]. Here, a beam with wavelength λ_0 and its second harmonic $\lambda_0/2$ is modelled, as the contribution of the second harmonic is the dominant one. Of course, higher harmonics contribute to the waveform as well and can be treated analogously. The impact of the Gouy phase on the waveform of the multicolour Gaussian pulse is explained here in this example to show the principle. The length of one cycle (2π in radians) is defined by the wavelength, but the different colours in the Gaussian beam are evaluated at the same absolute distance z from focus. This is important when calculating the relative phase between different colours.
The complete phase of a Gaussian beam on axis is $\varphi_\omega = \arctan(-z/z_{R,\omega}) + k_\omega z - \omega t$. The term $k_z - \omega t$ associated with the propagation of the beam increases linearly with z with a slope proportional to ω or in other words, the difference $k_{1\omega}z - \omega t - (k_{2\omega}z - 2\omega t)$ defines a point of constant phase relation between the 1ω and 2ω beam. This is clear intuitively: To propagate a distance $z - z_0$, a beam with a frequency of 2ω has to go through double the amount of cycles than a 1ω beam. Unwrapping the phase, that is undoing the restriction of the phase to the $[0, 2\pi]$ interval, the $k_z - \omega t$ term produces a linear curve, where the slope of the 2ω curve is twice as steep compared to the 1ω (see figure 5.1a).
As we are interested in the relative phase at an absolute z position for every time t, both propagation terms have to cancel each other. Therefore, to be comparable, one has to decide to measure the phase difference either in radians of the 1ω or 2ω

frequency. Here, it is given in terms of the 2ω beam, hence there has to be a factor 2 in front of $\varphi_{1\omega}$. The relative phase between the 1ω and 2ω component is thus $\Delta\varphi = 2\varphi_{1\omega} - \varphi_{2\omega}$ or

$$\Delta\varphi = 2\arctan\left(-z/z_{R,1\omega}\right) - \arctan\left(-z/z_{R,2\omega}\right) \tag{5.1}$$

where $z_{R,1\omega} = \pi w_0^2 \lambda_L^{-1}$ and $z_{R,2\omega} = \pi w_0^2 \left(\lambda_L/2\right)^{-1}$, assuming a common source size w_0 for both colours. For a fixed absolute propagation distance, the Gouy phase

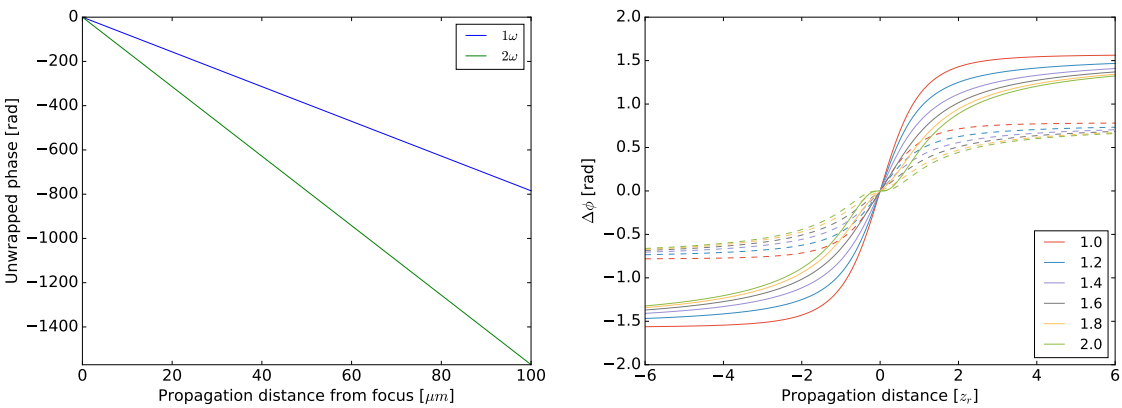

(a) Total unwrapped phase of a 1ω Gaussian beam vs. 2ω The slope of the phase of the 2ω beam is twice as steep compared with the 1ω beam.

(b) Relative phase between 1ω and 2ω for 2D (dashed lines) and 3D (solid lines) and for different 2nd harmonic source sizes $w_{2\omega} = w_{1\omega}/n$.

Figure 5.1.: Total phase and phase difference of a Gaussian two colour beam.

shifts for the individual wavelengths will be different and thus the relative phase between them will change while propagating. The evolution of the relative phase between a 1ω and 2ω Gaussian pulse in 2D and 3D with a focus at $z = 0$ is shown in figure 5.1b. Beginning in the focus with a relative phase of 0, the phase changes to $\pm\pi/2$ for 3D or $\pm\pi/4$ for 2D after a few Rayleigh lengths. The different colours represent different 2nd harmonic source sizes, $w_{2\omega} = w_{1\omega}/n$, with n the indicated number. Smaller source sizes reduce the steepness of the curve as well as reduce the asymptotic value for $z \to \pm\infty$. The blue curve for $n = 1.0$ corresponds to equation 5.1.

5.1.1. Influence on the waveform

The evolving relative phases will change the waveform dramatically while propagating in free space. The waveforms are shown in figure 5.2 for three different cases: in focus (figure 5.2(b)) and $1z_r$ (measured in terms of the wavelength of the fundamental) before and after the focus (figure 5.2(a) and (c)). As a result, a symmetrical waveform in focus changes to an asymmetric form out of focus.
It is known from experiments with 2-colour laser pulses, that the waveform and relative phase is crucial to the generation efficiency of surface high harmonics [61]. It is therefore a good assumption that this will also play a role in the enhanced harmonics generated in a multipass geometry [79, 80]. Here, the relative phase between harmonics generated on the first target is determined by the distance they need to travel until they hit the second target.
In addition to the waveform, the second important factor for the generation efficiency is the intensity reduction when propagating further away from the focus. However, as it is shown in section 5.3, the optimal waveform has a larger impact and outweighs the reduced intensity. We tested this assumption by conducting a wide range of 1D and 2D PIC simulations.

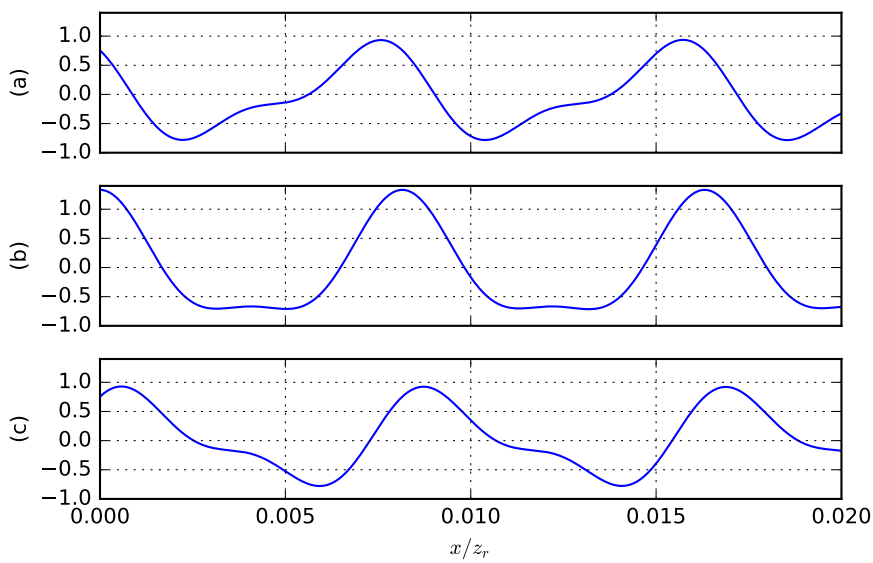

Figure 5.2.: Waveforms of a Gaussian beam mixing consisting of 1ω and 2ω components, $1z_r$ before focus (a), in focus (b) and $1z_r$ behind focus (c), where z_r is the rayleigh length of the 1ω Gaussian beam. Due to the Gouy phase change being different for 1ω and 2ω, the relative phase changes with propagation and thus the waveform.

5.1.2. Linear compensation

In general, it is not possible to compensate for this phase shift by adjusting the source size of 2ω beam due to the non-linearity of the arctan function. However, it is possible to compensate for the linear term in the Taylor expansion of $\arctan(x) = x + \mathcal{O}(3)$. With this approximation, equation 5.1 becomes

$$\Delta\varphi \approx 2z/z_R - z/z_{R,2\omega} \quad . \tag{5.2}$$

To cancel the linear term, the constraint $z_{R,2\omega} = z_R/2$ has to be fulfilled. This is possible with a 2ω source size of $w_{0,2\omega} = w_0/2$. With this linear compensation, it

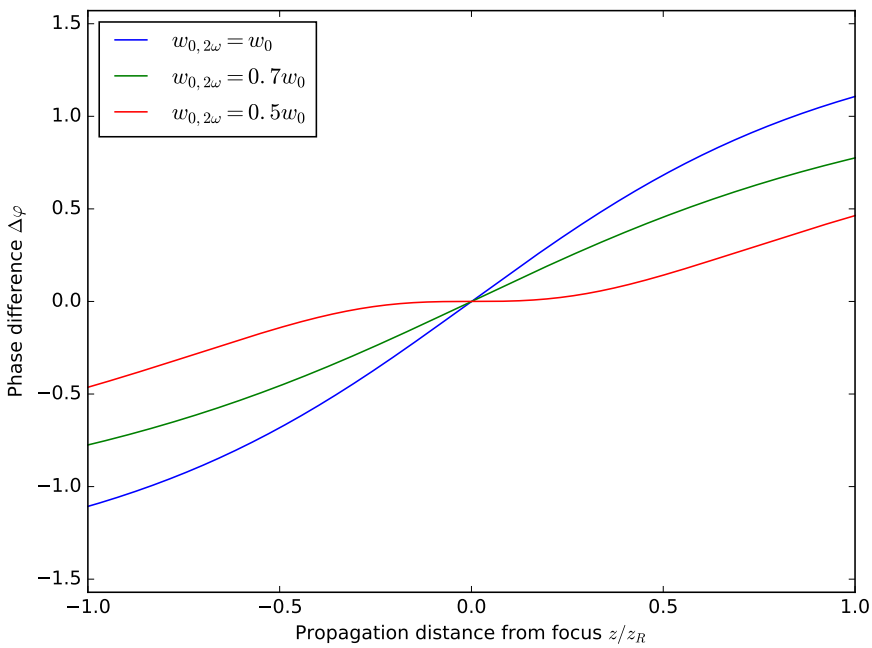

Figure 5.3.: Relative phase between 1ω and 2ω for a 2ω source size of w_0 and $w_0/2$. For the latter, the linear term cancels out and the phase difference is reduced close to the focus.

is possible to reduce the phase shift close to the focus in the range of $[-1z_R, 1z_R]$ to ± 0.5 radians opposed to ± 1.1 radians in the case of $w_{0,2\omega} = w_0$ (see figure 5.3). It is important to note that this linear compensation only works close to the focus and requires careful adjustment of the source size, which is unrealistic for real world experiments. For a beam with more than two colours, the calculation above would have to be performed for each individual colour and the source sizes adjusted accordingly.

5.2. Methods

5.2.1. PIC Simulations

The simulation setup (figure 5.4) consists of two targets A and B of an overdense ($n = 200n_c$, where n_c is the critical density for the fundamental laser pulse frequency) quasi-neutral plasma with a step-like density distribution. Target A is placed at the origin $(0, 0)$ of the coordinate system at an angle of $\theta = 45°$. The second target is placed at position $(0, -d)$ under an angle of $\theta = -45°$.
This target orientation is important to be able to achieve an enhancement at all. If the targets would both be aligned at the same $\theta = 45°$ angle, the harmonic intensity after the second pass would have been even lower than after the first pass and no enhancement would be possible. The reason for this is that one not only has to consider the intensity, but the orientation of the electric field. After reflection from target A, the shape of the pulse is asymmetric with the highest peaks in amplitude in the negative half of the cycle. Only if the second target is oriented correctly, these highest peaks of the electric field will pull the electrons outwards across the plasma-vacuum boundary and generate the enhanced harmonics.
A Gaussian laser pulse with the central wavelength λ_0 is injected at the $-x$ boundary. The laser pulse has a maximum amplitude of $a_0 = 10$, a FWHM duration of $\tau = 5$ cycles and is p-polarized. On target B, the laser pulse is still p-polarized, as the polarization remains the same after the reflection from target A. These laser and plasma parameters are varied in section 5.4. The laser pulse is focused at the origin $(0, 0)$, i.e. at the surface of target A.
During the interaction with target A, high harmonics are generated in reflection due to the relativistic oscillating mirror (ROM) [24, 25]. After propagating the distance d, the laser pulse, now containing high order harmonics next to its fundamental frequency, interacts with target B creating even more intense XUV pulses [80].
In 1D PIC simulations, the 2D geometry can be emulated by a Lorentz transform to the boosted frame, in which the laser pulse is incident normally on the target [24, 25, 83]. In this frame, the plasma moves with a velocity of $v_y = \sin\theta$ and the electric field is transformed as $E'_y = E_y \cos\theta$. As there is no focus in 1D, the laser pulse is injected at the boundary with the intensity it would have in focus in 2D or 3D. Between the targets, the intensity and the Gouy phase are modelled according to the paraxial approximation (see section 5.2.2). All 1D PIC simulations, conducted with the code PICWIG1D [50], had a length of $4\lambda_0$ with a resolution of 500 grid cells

per wavelength. The plasma slab had a thickness of $0.8\lambda_0$ and there were initially 500 macro-particles per grid cell.

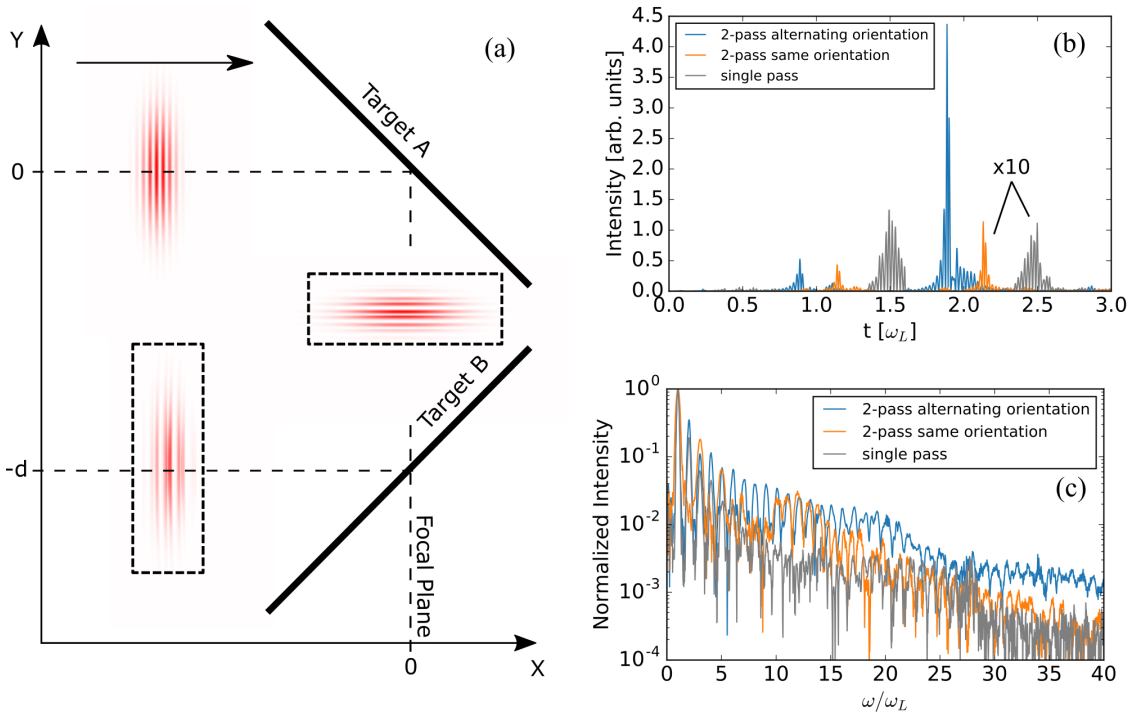

Figure 5.4.: **(a)** Simulation setup with two targets (not to scale), target A at an angle of $\theta = 45°$, target B at an angle of $\theta = -45°$. This orientation is important to be able to achieve an enhancement. The single colour laser pulse is initially propagating in $+x$ direction and is focused on target A. After being reflected off target A, it includes high order harmonics and hits target B after propagating the distance d. The pulse propagating in $-x$ direction contains the enhanced high order harmonics. Intensity plots of the laser pulse were taken from actual 2D PIC simulation. **(b)** Attosecond pulses obtained from 1D PIC simulations after the first target (grey, displayed 10 times larger to make it visible in the plot) and after the second target in the best case (blue). No enhancement is visible if the targets are in the wrong orientation (orange, also enlarged 10 times). **(c)** Spectrum of the pulses from (b).

All 2D PIC simulations have been performed with the code EPOCH [31]. The 2D PIC simulation for the first pass had a box size of $50\mu m \times 50\mu m$ with a resolution of 400 cells per μm. The laser pulse had a central wavelength of $800nm$ and a FWHM spotsize on target of $5\mu m$. The target thickness was $1.0\mu m$. Initially there were 20 macro-particles per grid cell. The pulse was retrieved after the first target and

propagated in free space to the distance needed using the method described in [74]. It was then inserted in another EPOCH simulation with a box size of $50\mu m \times 30\mu m$ and 400 cells per μm resolution. The target had the same properties as in the first pass, but was rotated by $\theta = -45°$.

The results are shown in terms of the attosecond pulse generation efficiency $\eta = I_{AP}/I_L$, where I_{AP} and I_L are the maximum intensities of the attosecond pulse (AP) and the incident laser respectively. The attosecond pulse is obtained by applying a highpass filter which cuts out everything below the 20th harmonic. For better comparison to the ordinary SHHG process with one pass, the axes are further normalized to the efficiency η_S of the single pass harmonics.

5.2.2. Modelling the Gouy Phase in 1D PIC simulations

Performing full scale 3D PIC simulations, especially of surface high harmonic generation in double reflection, would require a huge number of CPU-hours of computing time even for a single simulation, not to speak of simulating different parameters. Even the required resources for a parameter scan in 2D would have been substantial. As this was not feasible for this study, the effect of the Gouy phase was reproduced by artificially imposing the appropriate Gouy phase on the pulse after the first pass. The model was verified by imposing a 2D Gouy phase and comparing the results to full-scale 2D PIC simulations.

In 1D geometry, propagating pulses in free space show no diffraction and no phase shift. To model the free space propagation in higher dimensions between the two targets in a 1D PIC simulation, both the intensity and the phase had to be adjusted accordingly. The reflected pulse was obtained after the first target and, after a Fourier transform, the Gouy phase was artificially imposed on the pulse and used as input to the simulation of the second target. For each spectral component the Gouy phase was applied accordingly. This method was cross-checked with the model detailed in section 5.1. Likewise the intensity was reduced according to the paraxial approximation. Afterwards the pulse was injected into another simulation for the interaction with the second target.

5.3. Results

The resulting attosecond pulse generation efficiencies for different distances are shown in figure 5.5. The contributions of the intensity falloff due to diffraction and the Gouy phase are shown separately in figure 5.5(a) and (b). As one would expect, the intensity falloff (a) leads to a decreasing efficiency with larger distances. If one is taking into account the Gouy phase only (b), the efficiency reaches a maximum at about $0.2z_r$ (3D) and $0.5z_r$ (2D). The actual behaviour is the combination of both effects shown in (c).

This can be explained as follows: It is already known from 2-colour experiments [61], that the harmonic generation efficiency is only enhanced for a certain phase difference between the 1ω and 2ω component of the laser pulse. It is therefore sensible to assume that such a favourable phase relation also exists for a beam containing high order harmonics of the fundamental frequency. As the Gouy phase evolves differently for every frequency as outlined in section 5.1, the relative phase shift between the frequencies changes constantly with the propagation of the beam. The maximum efficiency is achieved at the distance, where the waveform is favourable for harmonic generation. This optimal distance between the two targets is not as close as possible, but in the range between $0.2z_r$ and $0.5z_r$. An enhancement, albeit smaller, can be expected for distances up to $1.0z_r$. For longer distances $z > z_r$, the effect of the decreased intensity becomes dominant and the efficiency is approaching 0.

As the beam propagates differently in 2D and 3D geometry, the harmonic generation efficiencies differ as well. Because the intensity falloff is slower in 2D, the efficiencies remain higher for longer distances. Furthermore, in the 2D case the Gouy phase lies in the range of $[-\pi/2, \pi/2]$, which is half the range of the 3D case and shifts the maximum efficiency slightly further out. However, the general shape with a maximum at a distance $< z_r$ and an asymptotic decay after the maximum remains the same for both 2D and 3D models.

To support this model, it is compared to full 2D PIC simulations (blue stars in figure 5.5(c)). While they qualitatively agree with the model, there are quantitative differences. This is expected [39], as the model only covers the Gouy phase and intensity falloff, but no other effects like source size shrinking, different divergence of the individual harmonics or coherent harmonic focusing [5]. When taking source size shrinking into account, the model predicts slightly lower efficiencies without

changing the shape of the curve. The effect of source size shrinking is shown in detail in figure 5.8.

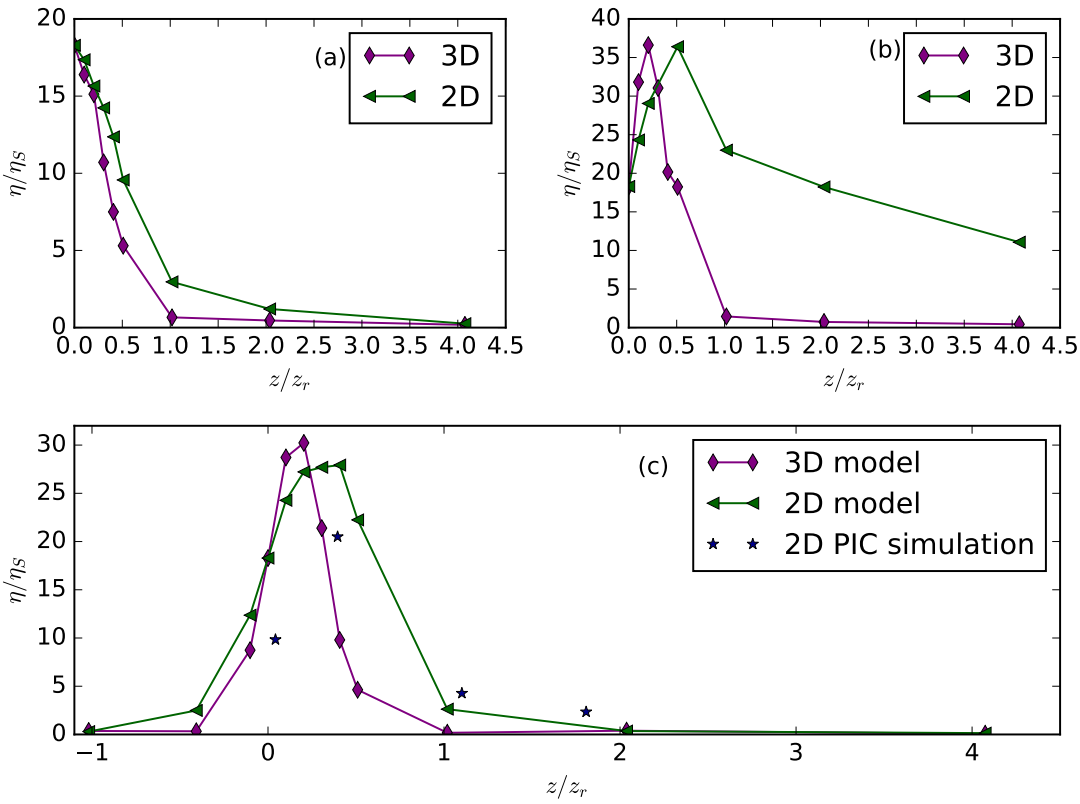

Figure 5.5.: Dependence of the harmonic generation efficiency $\eta = I_{AP}/I_L$ (normalized to the single pass efficiency η_S) on the distance between the two targets. The attosecond pulse is obtained by applying a highpass filter which cuts out everything below the 20th harmonic. Each data point corresponds to two 1D PIC simulation, one for the interaction with the first target, and one for the interaction with the second target. The pulse between the two targets has been modelled to reflect the intensity falloff only **(a)**, the Gouy phase shift only **(b)** and the combined effect of both **(c)**. The combined effect is also compared to full 2D simulations. Parameters for this scan: $a_0 = 10$, $n = 200n_c$, $\theta = 45°$.

The optimal distance of $0.2z_r$ predicted by the model can be challenging to achieve experimentally, as it requires two targets at very close distance to each other. There are two methods, how this length can be extended. By increasing the focal spot radius w_0, the rayleigh length z_r will increase with $\propto w_0^2$. While the fraction of the Rayleigh length for the optimal position stays the same, it would allow for a larger

actual distance between the targets. This comes with other challenges however, as the required intensity for SHHG may not be achievable with a large focus spot. In this case, refocusing of the harmonic beam between the targets could be a possibility. Using a parabolic mirror, the beam after target A could be reflected and refocused on target B. After reflection from the mirror the Gouy phase evolves in the opposite direction, reducing the relative phase shift between the colours. This would allow for arbitrary large physical distances between the targets, only limited by experimental constraints.

Positioning target B behind the focus of the refocused beam would be equivalent to negative distances between the targets, as also shown in figure 5.5(c). The model predicts in that case an even faster decreasing efficiency without a maximum, which suggests that this case should be avoided in experiments.

5.4. Parameter Scan

Until now, only one set of parameters ($a_0 = 10$, $n = 200n_c$, $\theta = 45°$, no scale length) has been used to show the principle. To investigate the influence of the various laser-plasma parameters on the optimal distance, more than 200 additional 1D PIC simulations have been conducted. For every set of parameters simulated there was a clear optimal distance which maximized the efficiency. Depending on the specific interaction parameters, the optimal distance varies slightly. As long as the similarity parameter $S = n_e/\left(a_0 n_c\right)$ [59] remains the same, the position of the optimal distance will not change, shown in figure 5.6a. If S is changed, e.g. for different a_0 at constant n, the optimal distance will vary between $0.1z_r$ and $0.36z_r$ for a range of $a_0 = 8 \ldots 20$ (corresponding to a $S = 25 \ldots 10$), as shown in figure 5.6b.

Introducing a preplasma scale length L_p, the absolute efficiency even for a single target is expected to increase [51]. A series of simulations for the experimentally relevant cases of $L_p = 0.05\lambda_0$ and $L_p = 0.1\lambda_0$ [60] have been conducted and the results are shown in figure 5.7. Compared to the case without preplasma, the optimal distance is shifted closer to the first target. The magnitudes differ as the single target efficiency used for normalization also increases with the addition of preplasma. The angle of incidence did not have a significant influence on the position of the optimal distance.

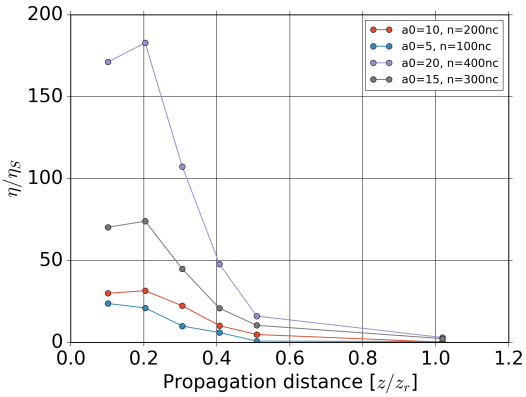

(a) Dependence of the optimal distance for different combinations of a_0 and n, where the ratio $S = n_e/(a_0 n_c)$ has been kept constant. Other parameters remain the same at $L_p = 0$, $\theta = 45°$, 3D case. The position of the maximum efficiency does not change.

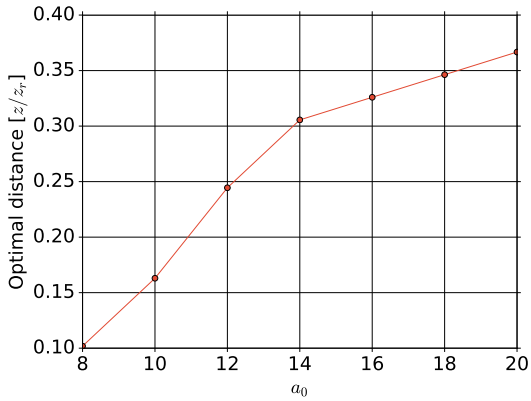

(b) Dependence of the optimal distance on the incidence laser intensity a_0. Other parameters remain the same at $n = 200n_c$, $L_p = 0$, $\theta = 45°$, 3D case.

Figure 5.6.: Results of the parameter scan.

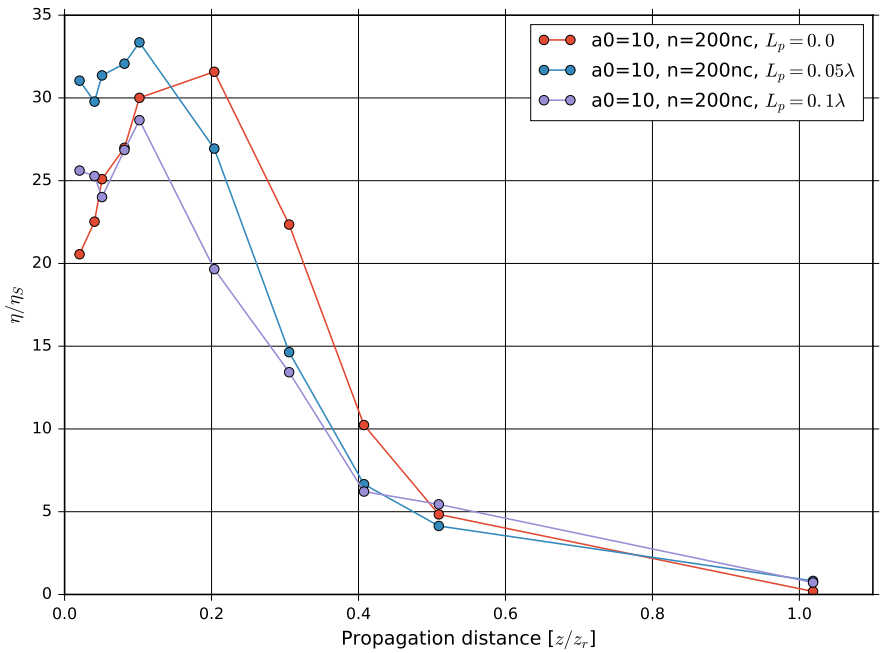

Figure 5.7.: Dependence of the harmonic generation efficiency $\eta = I_{AP}/I_L$ (normalized to the single pass efficiency η_S for a target with the same scale length) on the scalelength L_p of the targets. Other parameters remain the same at $a_0 = 10, n = 200n_c$, $\theta = 45°$, 3D case.

In this section, the focus of the incident laser pulse was always on the first target. Another possibility would be to focus the beam on the second target, where the first target would act as a plasma mirror also generating high order harmonics. In this setup, there is a further constraint on the distance between the two targets. The intensity on the out-of-focus first target must still be high enough to generate at least 10%, better $20-30\%$ of second harmonic intensity [84]. In case of a peak intensity of $a_0 = 10$ of the incident laser pulse, for the best second harmonic conversion efficiency the first target should not be more than $0.5z_r$ out of focus. Full 2D simulations were performed for this case and otherwise same parameters as the other simulations in this chapter. The highest efficiency gain of 8.5 was achieved for the first target at $0.3z_r$ in front of the focus, which is comparable to the efficiency where the focus was on the first target and the second target the same distance behind focus.

5.5. Conclusions

In summary the Gouy phase shift changes the relative phase between multiple colours in a Gaussian beam while propagating. This also changes the resulting waveform, which has implication for multipass high order harmonics generation. As the waveform changes with the propagated distance, there exists an optimal distance between the two targets, where the harmonic generation efficiency on the second target is maximized. This optimal distance depends on the exact geometry, laser and plasma parameters, but can be found for a broad range of parameters in the region between $0.1z_r$ and $0.5z_r$.

To find this distance, a series of 1D PIC simulations has been conducted, where the Gouy phase and intensity are modelled for propagation in 2D and 3D. These simulations are supported by full 2D PIC simulations. For the specific interaction parameters of $a_0 = 10, n = 200n_c$ and $L_p = 0$ used in this paper, it is found that the harmonic generation efficiency peaks at 30x for $0.2z_r$ or $0.5z_r$ for 3D and 2D propagation geometry, respectively. It is not optimal to just minimize the distance between the two targets, as one would assume purely from the intensity falloff alone. This highlights the importance to consider the difference in the evolution of the Gouy phase when comparing 2D PIC simulations and experiments.

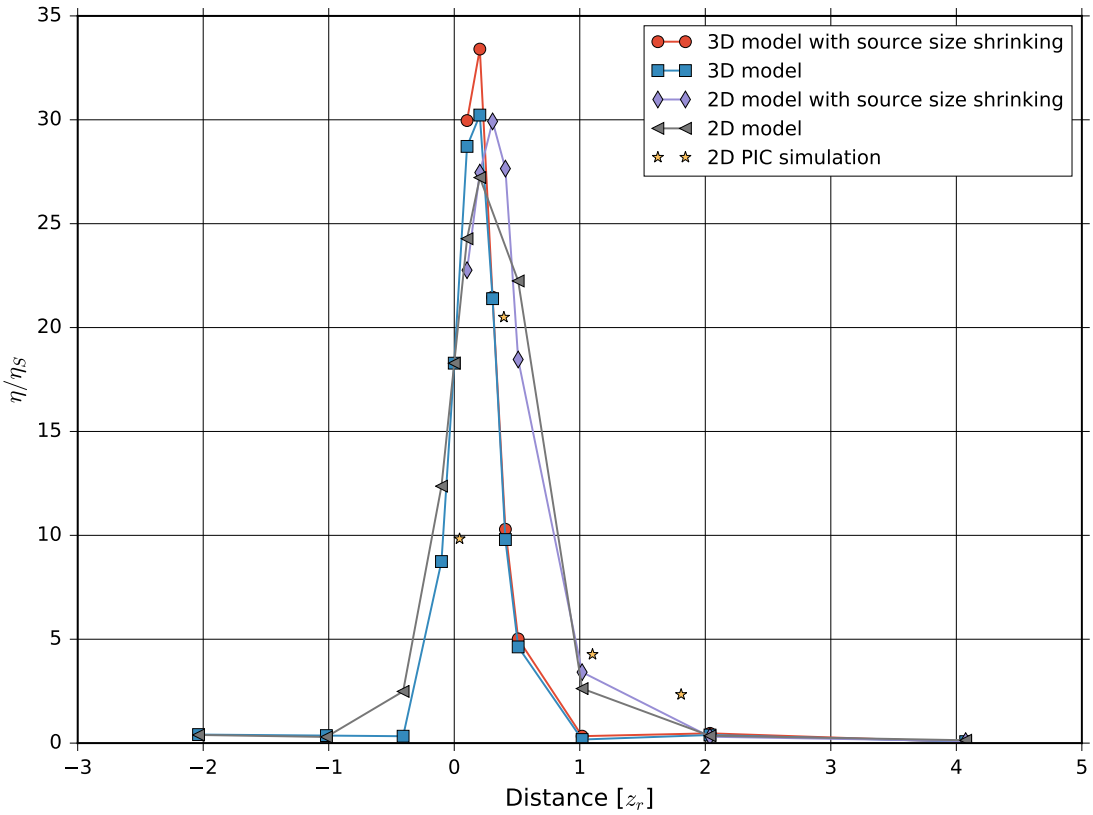

Figure 5.8.: Harmonic Generation efficiency of the two pass scheme normalized to the single pass efficiency η_s. The efficiency is shown in dependence of the propagation distance between the two targets. A clear enhancement can be seen for all cases if the distance is smaller than one Rayleigh length. While there is still an enhancement for the smallest distances, the highest efficiency is predicted for $0.2z_r$ (3D) and $0.5z_r$ (2D). Including source size shrinking into the model changes the optimum slightly, but not the overall trend. The full 2D simulations confirms the model qualitatively.

6. Conclusion

In this thesis, different ways to optimize the XUV emission form Surface High Harmonic Generation (SHHG) with regard to

- the temporal and spatial isolation of single attosecond pulses from a pulse train and
- the efficiency of the harmonic generation process

have been explored in order to facilitate potential applications. Towards this goal, controlling the laser and plasma parameters of the interaction and gaining a deeper understanding of how each parameter affects the produced XUV radiation has been crucial. The most important tools used in this study are extensive parameter scans with 1D and 2D PIC simulations guided by analytic models.
Different techniques for pulse isolation and efficiency enhancement have been discussed and analysed with regard to the optimal parameters and potential obstacles for future experiments have been identified.
In particular, for temporal pulse isolation intensity gating by controlling the CEP has been discussed. It has been shown for normal incidence, that there is a density dependent phase shift between the incident laser pulse and driving electromagnetic field. The phase shift depends on the exact shape of the density gradient and pre-plasma scale length at the target surface, but there is an optimal CE phase, where a single AP is generated from a 4-cycle incident pulse. For a step-like density distribution, an analytical solution exists. In that case, the CEP shift is approximately $\pi/2$ for a solid-density target. This shifts an incident sine shaped pulse to a cosine pulse and vice versa, which leads to the counter-intuitive conclusion that a sine shaped pulse should be used to generate an isolated AP.
For spatial separation, the influence of surface denting on the attosecond lighthouse effect has been investigated. It has been shown that surface denting increases the divergence of the generated APs, which reduces the contrast between the individual AP. If surface denting is not controlled, it can lead to a loss of separation between

the pulses. If a separation is not possible, information about the surface denting can be obtained from the spectrum. The angular chirp in the spectrum of the reflected APs depends on the incident intensity a_0 and the preplasma scale length L_p and is thus a measure for the surface denting depth of an initially flat target.
To enhance the conversion efficiency of the high harmonic generation process, the multipass scheme has been proposed recently. In this thesis, the influence of the distance between the targets on the efficiency has been investigated. Due to the Gouy phase, the relative phase between the multiple colours in a Gaussian beam changes while propagating. This effect also changes the waveform at the position of the second target, which has implications for the generation efficiency. It is found that there exists a non-trivial optimal distance, where the harmonic generation efficiency on the second target is maximized. It depends on the exact interaction parameters like incident intensity and preplasma scale length, but is found for a broad range of parameters in the region between $0.1z_r$ and $0.5z_r$.

6.1. Outlook and Future Work

The findings presented here provide valuable insight for possible future SHHG experiments. The laser parameters used in the simulations are close to the intensities and durations, which are already available at laser facilities, or will be in the near future [32]. Especially the multipass scheme from chapter 5 for two passes is of great interest for experimental realisation, as it promises an advantage in the efficiency of the harmonic generation process. With the results presented here, it can be made sure that experiments use the optimal target distance to achieve the maximum efficiency enhancement.
Still, there are plenty of open questions which await further investigation. The parameter space consisting of laser intensity, target density, preplasma scale length and distance between two or more targets is huge and needs considerable computational resources if explored with 2D PIC simulations. But 2D or even better 3D PIC simulations would be needed to study certain aspects like the effects of surface denting in multipass configurations in more detail. One could even experiment with preformed targets of different shapes to find a set of parameters which could increase the efficiency even further.
With the recent advances in computing power of the world's top 500 super computers [85], full simulation of complete experiments will become feasible for other

experiments than LWFA or PWFA [38]. Simulations of SHHG have been rarely performed in 3D due to their high computational demand [86], as the resolution has to be high enough to resolve the plasma frequency of the overdense plasma target. With the newest generations of super-computers available to scientists, it is feasible to study the interaction of a few-cycle laser pulse with a plasma target in 3D with attosecond time resolution. By incorporating more effects like collisions, ionization and even QED effects into PIC codes, quantitative predictions of experimental results comes within reach.

A. Appendix

A.1. Ion acceleration with the TNSA mechanism

The interaction of a laser pulse with relativistic intensity and a solid-density plasma does not only produce bursts of XUV radiation, but can also be used to accelerate protons to energies of several MeV in very short distances [62, 87–89]. The interaction geometry is not very different to SHHG, which makes it natural to investigate this phenomenon with the same kind of PIC simulations. The simulations presented in this chapter have been performed to support a support an experimental study in a collaboration with G. A. Becker [33].

An ultraintense laser pulse is incident normally on a thin foil target. Electrons at the illuminated front side gain energy and these hot electrons travel to the rear side, forming an electron sheath. The resulting electrostatic forces lead to an acceleration of the ions on the rear side. The most common model used to explain this effect is the target normal sheath acceleration (TNSA) [90]. In the following section, the main equations to approximately describe the TNSA mechanism are discussed. In the last two sections the simulations helping to explain two experimental results are presented.

The electron heating at the front side is driven by the ponderomotive force,

$$\mathbf{F}_p = -m_e c^2 \nabla \left(1 + \langle \mathbf{A} \rangle^2\right)^{1/2} \quad , \tag{A.1}$$

where $\langle \mathbf{A} \rangle$ is the cycle-averaged vector potential of the incident laser pulse. Any fast oscillations thus do not contribute to this force. Due to their lower mass, only electrons are accelerated at this stage. They gain energy and momentum normal to the surface of the target in the electromagnetic field of the incident laser pulse. There are multiple mechanism to describe the electron heating, mainly Brunel [55] heating and "$\mathbf{J} \times \mathbf{B}$" heating [91]. These hot electrons form a current towards the rear side of the target, as can be seen from the PIC simulation shown in figure A.1.

Due to their high temperature, they exit the target at the rear side and form an electron sheath. This creates a charge separation field, which accelerates the lighter ions (mainly protons), while the heavier ions remain in place and maintain the accelerating electrical field. On longer timescales $\gtrsim$ 1ps also the heavier ions are accelerated. Another acceleration mechanism, especially for very thin targets, is the

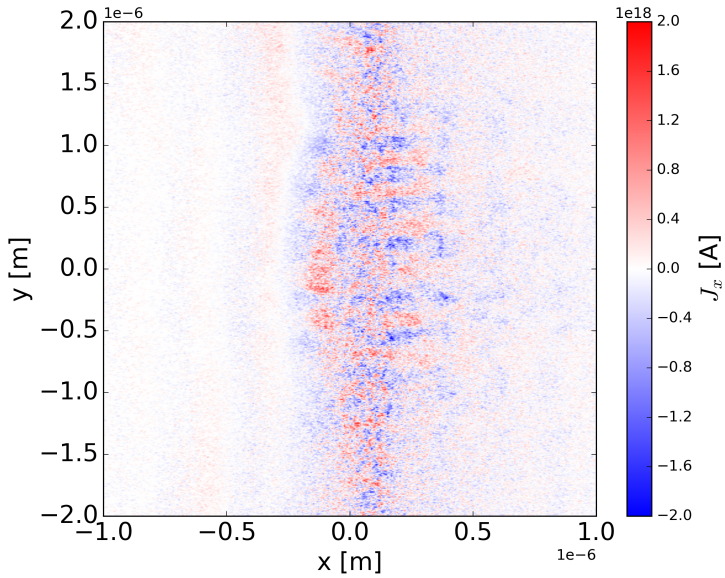

Figure A.1.: Electron current J_x inside the target during the interaction with the laser pulse. The hot electron current towards the rear side of the target as well as the return current can be seen as blue and red structures.

so called "Light sail". Due to the momentum gained, the effective plasma density is reduced by n_e/γ with $\gamma = \sqrt{1 + a_0^2}$. This self-induced relativistic transparency lets the laser pulse propagate deeper into the target and ultimately accelerate the electrons on the back side of the target. In both cases, the ion acceleration then happens on the rear side of the target. The electron sheath creates a strong charge separation field, which accelerates the ions in the same direction as the propagation direction of the laser pulse and normal to the target surface.

A.1.1. Ring-Like structures

In several independent ion acceleration experiments (see [33] and references therein) a ring-like structure (RLS) of the spatial proton distribution has been observed behind the target, with a clear explanation still missing. This behaviour is also

reproduced by 2D PIC simulations, which are used here to find the cause for the RLS. Note that due to their 2D nature, the RLS is observed as two distinct peaks at the same angle in both directions from the target normal. A Gaussian laser pulse with a wavelength of $\lambda_L = 515$nm, a pulse duration of $\tau = 140$fs, a FWHM focal spot of 3μm and an normalized intensity of $a_0 = 4.5$ was focused on the front surface of the target. The parameters resemble the POLARIS laser facility [92] with a frequency-doubled laser pulse, which are the same parameter as in the experiment. The target density was $90n_c$ in all cases, but the target width was varied between 100nm and 800nm. It consisted of a quasi-neutral plasma with protons and fully ionized carbon ions in a $1:1$ ratio. The front side of the target was always located at $x = 0$. A resolution of 200 cells per μm has been used. The RLS was visible in all cases. The spatial kinetic energy distribution of the protons is shown in figure A.2a. As expected, the protons in the centre part, where the electron sheath has expanded the furthest, gain the most energy. But the protons are not evenly distributed, but peak slightly off-axis, in the case for a 800nm thick foil at $\pm 5°$ (figure A.2d). At this positions, energies close to the peak energy ($\geq 0.98E_{\text{peak}}$) are achieved, but at a much higher particle count. The spatial energy distribution is shown in figure A.2c. This two-peak structure is the signature of the RLS in 2D.

Protons accelerated on the rear side of the target have a non-zero p_y momentum, pointing outward and thus leading to the off-axis acceleration (figure A.2b). The cause for this acceleration and thus the RLS are lateral electrical fields induced by the non-uniformity of the electron sheath. As the electrons in the centre expand further outward due to their higher temperature in this area, a bell-shaped electron sheath is created behind the target. As the charge distribution is not uniform along the y-axis, a E_y field component is induced, leading to the lateral acceleration and thus the RLS.

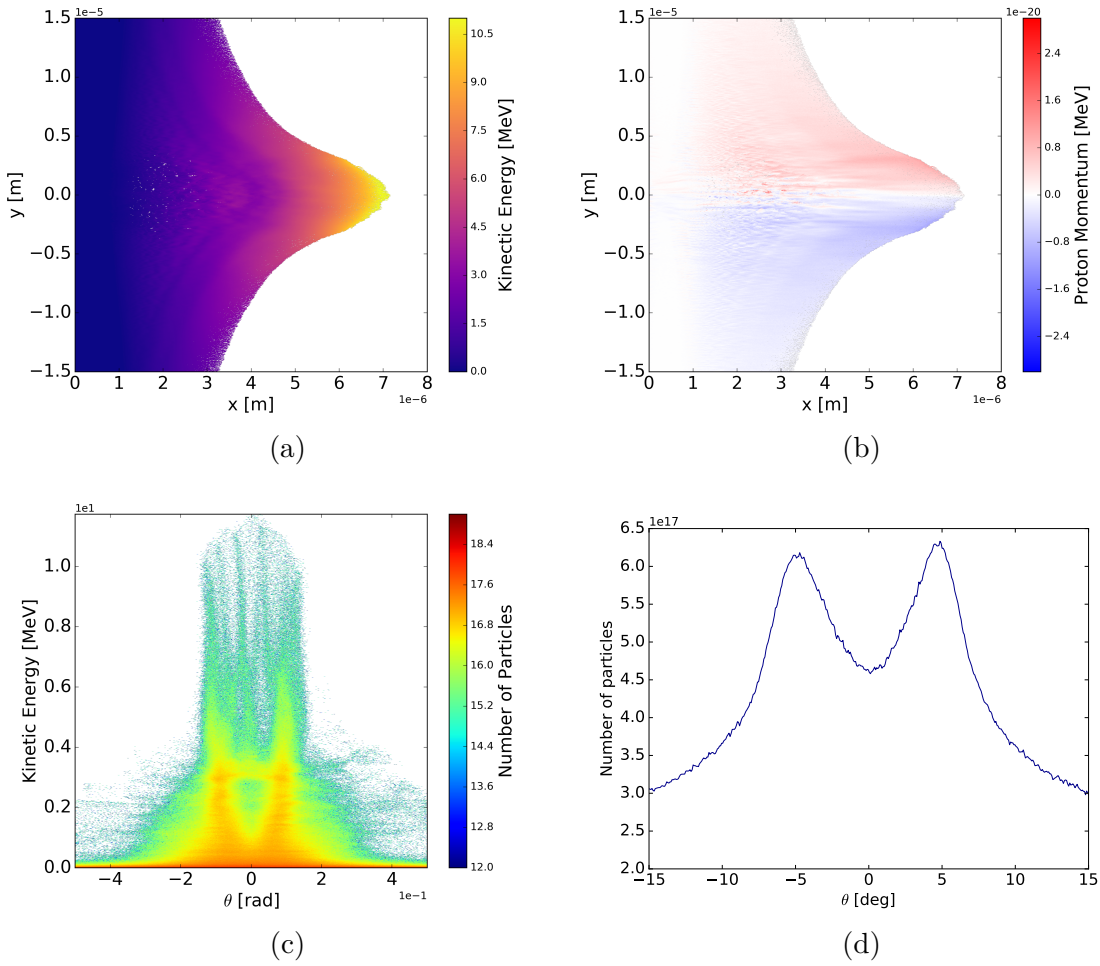

Figure A.2.: Results from a 2D PIC simulation for a TNSA experiment at the POLARIS laser facility ($\lambda_L = 515$nm, $\tau = 140$fs, $a_0 = 4.5$, 3μm FWHM spot size). **(a)** Spatial proton distribution, colour shows the energy in MeV. **(b)** p_y component of the proton momentum. **(c)** Proton energy distribution in dependence of the angle $\theta = \arctan(p_x/p_y)$. **(d)** Angular distribution of protons.

B. Bibliography

[1] M. Hentschel et al. "Attosecond metrology". In: *Nature* 414.6863 (Nov. 2001), pp. 509–513. ISSN: 0028-0836. DOI: 10.1038/35107000. URL: http://www.nature.com/articles/35107000.

[2] M Drescher et al. "Time-resolved atomic inner-shell spectroscopy". In: *Nature* 419.6909 (Oct. 2002), pp. 803–807. ISSN: 0028-0836. DOI: 10.1038/nature01143. URL: http://www.nature.com/articles/nature01143.

[3] Christoph Bostedt et al. "Linac Coherent Light Source: The first five years". In: *Reviews of Modern Physics* 88.1 (2016). ISSN: 15390756. DOI: 10.1103/RevModPhys.88.015007.

[4] S. Gordienko et al. "Relativistic Doppler Effect: Universal Spectra and Zeptosecond Pulses". In: *Physical Review Letters* 93.11 (Sept. 2004), p. 115002. ISSN: 0031-9007. DOI: 10.1103/PhysRevLett.93.115002. URL: https://link.aps.org/doi/10.1103/PhysRevLett.93.115002.

[5] S. Gordienko et al. "Coherent focusing of high harmonics: A new way towards the extreme intensities". In: *Physical Review Letters* 94.10 (2005), pp. 1–4. ISSN: 00319007. DOI: 10.1103/PhysRevLett.94.103903.

[6] Henri Vincenti. "Achieving Extreme Light Intensities using Optically Curved Relativistic Plasma Mirrors". In: *Physical Review Letters* 123.10 (2019), p. 105001. ISSN: 1079-7114. DOI: 10.1103/PhysRevLett.123.105001. URL: https://doi.org/10.1103/PhysRevLett.123.105001.

[7] Felix Karbstein and Elena A. Mosman. "X-ray photon scattering at a focused high-intensity laser pulse". In: *Physical Review D* 100.3 (2019), p. 33002. ISSN: 24700029. DOI: 10.1103/PhysRevD.100.033002. URL: https://doi.org/10.1103/PhysRevD.100.033002.

[8] Felix Karbstein et al. "Boosting Quantum Vacuum Signatures by Coherent Harmonic Focusing". In: *Physical Review Letters* 123.9 (2019), p. 91802. ISSN: 10797114. DOI: 10.1103/PhysRevLett.123.091802. arXiv: 1905.00858. URL: https://doi.org/10.1103/PhysRevLett.123.091802.

[9] Alexander Blinne et al. "All-optical signatures of quantum vacuum nonlinearities in generic laser fields". In: *Physical Review D* 99.1 (2019), p. 16006. ISSN: 24700029. DOI: 10.1103/PhysRevD.99.016006. arXiv: 1811.08895. URL: https://doi.org/10.1103/PhysRevD.99.016006.

[10] L Chopineau et al. "Plasma mirrors as a path to the Schwinger limit". In: (July 2020), pp. 1–7. arXiv: 2007.05325. URL: http://arxiv.org/abs/2007.05325.

[11] XFEL. *European XFEL - Facts and Figures*. URL: https://www.xfel.eu/facility/overview/facts_amp_figures/index_eng.html (visited on 12/03/2021).

[12] E. Esarey, C. B. Schroeder and W. P. Leemans. "Physics of laser-driven plasma-based electron accelerators". In: *Reviews of Modern Physics* 81.3 (Aug. 2009), pp. 1229–1285. ISSN: 0034-6861. DOI: 10.1103/RevModPhys.81.1229. URL: https://link.aps.org/doi/10.1103/RevModPhys.81.1229.

[13] S. G. Rykovanov et al. "Plasma Undulator Based on Laser Excitation of Wakefields in a Plasma Channel". In: *Physical Review Letters* 114.14 (Apr. 2015), p. 145003. ISSN: 0031-9007. DOI: 10.1103/PhysRevLett.114.145003. URL: https://link.aps.org/doi/10.1103/PhysRevLett.114.145003.

[14] B Dromey et al. "High harmonic generation in the relativistic limit". In: *Nature Physics* 2.7 (July 2006), pp. 456–459. ISSN: 1745-2473. DOI: 10.1038/nphys338. URL: http://www.nature.com/articles/nphys338.

[15] N. H. Burnett et al. "Harmonic generation in CO2 laser target interaction". In: *Applied Physics Letters* 31.3 (1977), pp. 172–174. ISSN: 00036951. DOI: 10.1063/1.89628.

[16] R. L. Carman, C. K. Rhodes and R. F. Benjamin. "Observation of harmonics in the visible and ultraviolet created in CO2-laser-produced plasmas". In: *Physical Review A* 24.5 (Nov. 1981), pp. 2649–2663. ISSN: 0556-2791. DOI: 10.1103/PhysRevA.24.2649. URL: https://link.aps.org/doi/10.1103/PhysRevA.24.2649.

[17] Donna Strickland and Gerard Mourou. "Compression of amplified chirped optical pulses". In: *Optics Communications* 56.3 (1985), pp. 219–221. ISSN: 00304018. DOI: 10.1016/0030-4018(85)90120-8.

[18] S. Kohlweyer et al. "Harmonic generation from solid-vacuum interface irradiated at high laser intensities". In: *Optics Communications* 117.5-6 (1995), pp. 431–438. ISSN: 00304018. DOI: 10.1016/0030-4018(95)00200-R.

[19] D. Von Der Linde et al. "Generation of high-order harmonics from solid surfaces by intense femtosecond laser pulses". In: *Physical Review A* 52.1 (1995), pp. 25–27. ISSN: 10502947. DOI: 10.1103/PhysRevA.52.R25.

[20] P. A. Norreys et al. "Efficient extreme UV harmonics generated from picosecond laser pulse interactions with solid targets". In: *Physical Review Letters* 76.11 (1996), pp. 1832–1835. ISSN: 10797114. DOI: 10.1103/PhysRevLett.76.1832.

[21] C.K Birdsall and A.B Langdon. *Plasma Physics via Computer Simulation*. Bristol, Philadelphia and New York: Adam Hilger, 1985. ISBN: 0070053715.

[22] U. Teubner et al. "Harmonic emission from the rear side of thin overdense foils irradiated with intense ultrashort laser pulses". In: *Physical Review Letters* 92.18 (2004), pp. 1–4. ISSN: 00319007. DOI: 10.1103/PhysRevLett.92.185001.

[23] F. Quéré et al. "Coherent Wake Emission of High-Order Harmonics from Overdense Plasmas". In: *Physical Review Letters* 96.12 (Mar. 2006), p. 125004. ISSN: 0031-9007. DOI: 10.1103/PhysRevLett.96.125004. URL: https://link.aps.org/doi/10.1103/PhysRevLett.96.125004.

[24] S. V. Bulanov, N. M. Naumova and F. Pegoraro. "Interaction of an ultrashort, relativistically strong laser pulse with an overdense plasma". In: *Physics of Plasmas* 1.3 (1994), p. 745. ISSN: 1070664X. DOI: 10.1063/1.870766. URL: http://link.aip.org/link/?PHPAEN/1/745/1.

[25] R. Lichters et al. "Short-pulse laser harmonics from oscillating plasma surfaces driven at relativistic intensity". In: *Physics Of Plasmas* 3.9 (1996), pp. 3425–3437. ISSN: 1070664X. DOI: 10.1063/1.871619.

[26] D. An Der Brügge and a. Pukhov. "Enhanced relativistic harmonics by electron nanobunching". In: *Physics of Plasmas* 17.3 (2010), pp. 1–7. ISSN: 1070664X. DOI: 10.1063/1.3353050. arXiv: 1002.3576.

[27] B. Dromey et al. "Coherent synchrotron emission from electron nanobunches formed in relativistic laser–plasma interactions". In: *Nature Physics* 8.11 (2012), pp. 804–808. ISSN: 1745-2473. DOI: 10.1038/nphys2439. URL: http://dx.doi.org/10.1038/nphys2439.

[28] N. M. Naumova et al. "Relativistic Generation of Isolated Attosecond Pulses in a λ 3 Focal Volume". In: *Physical Review Letters* 92.6 (Feb. 2004), p. 063902. ISSN: 0031-9007. DOI: 10.1103/PhysRevLett.92.063902. URL: https://link.aps.org/doi/10.1103/PhysRevLett.92.063902.

[29] I. Watts et al. "Dynamics of the Critical Surface in High-Intensity Laser-Solid Interactions: Modulation of the XUV Harmonic Spectra". In: *Physical Review Letters* 88.15 (Mar. 2002), p. 155001. ISSN: 0031-9007. DOI: 10.1103/PhysRevLett.88.155001. URL: https://link.aps.org/doi/10.1103/PhysRevLett.88.155001.

[30] S. G. Rykovanov et al. "Intense single attosecond pulses from surface harmonics using the polarization gating technique". In: *New Journal of Physics* 10 (2008). ISSN: 13672630. DOI: 10.1088/1367-2630/10/2/025025.

[31] T. D. Arber et al. "Contemporary particle-in-cell approach to laser-plasma modelling". In: *Plasma Physics and Controlled Fusion* 57.11 (2015). ISSN: 13616587. DOI: 10.1088/0741-3335/57/11/113001.

[32] Sergei Kühn et al. "The ELI-ALPS facility: The next generation of attosecond sources". In: *Journal of Physics B: Atomic, Molecular and Optical Physics* 50.13 (2017). ISSN: 13616455. DOI: 10.1088/1361-6455/aa6ee8.

[33] G. A. Becker et al. "Ring-like spatial distribution of laser accelerated protons in the ultra-high-contrast TNSA-regime". In: *Plasma Physics and Controlled Fusion* 60.5 (2018), pp. 1–9. ISSN: 13616587. DOI: 10.1088/1361-6587/aab319.

[34] J.A. Bittencourt. *Fundamentals of Plasma Physics*. Springer New York, 2013. ISBN: 9781475740301.

[35] C.E. Shannon. "Communication in the Presence of Noise". In: *Proceedings of the IRE* 37.1 (Jan. 1949), pp. 10–21. ISSN: 0096-8390. DOI: 10.1109/JRPROC.1949.232969. URL: http://ieeexplore.ieee.org/document/1697831/.

[36] Kane Yee. "Numerical solution of initial boundary value problems involving maxwell's equations in isotropic media". In: *IEEE Transactions on Antennas and Propagation* 14.3 (May 1966), pp. 302–307. ISSN: 0018-926X. DOI: 10.1109/TAP.1966.1138693. URL: http://ieeexplore.ieee.org/document/1138693/.

[37] Alexander Blinne et al. "A systematic approach to numerical dispersion in Maxwell solvers". In: *Computer Physics Communications* 224 (2018), pp. 273–281. ISSN: 00104655. DOI: 10.1016/j.cpc.2017.10.010. arXiv: 1710.06829. URL: https://doi.org/10.1016/j.cpc.2017.10.010.

[38] Lieselotte Obst-Huebl et al. "All-optical structuring of laser-driven proton beam profiles". In: *Nature Communications* 9.1 (2018). ISSN: 20411723. DOI: 10.1038/s41467-018-07756-z.

[39] P. Heissler et al. "Multi- µj harmonic emission energy from laser-driven plasma". In: *Applied Physics B: Lasers and Optics* 118.2 (2015), pp. 195–201. ISSN: 09462171. DOI: 10.1007/s00340-014-5968-x.

[40] S. Fuchs et al. "Sensitivity calibration of an imaging extreme ultraviolet spectrometer-detector system for determining the efficiency of broadband extreme ultraviolet sources". In: *Review of Scientific Instruments* 84.2 (2013). ISSN: 00346748. DOI: 10.1063/1.4788732.

[41] A. PUKHOV. "Three-dimensional electromagnetic relativistic particle-in-cell code VLPL (Virtual Laser Plasma Lab)". In: *Journal of Plasma Physics* 61.3 (Apr. 1999), pp. 425–433. ISSN: 0022-3778. DOI: 10.1017/S0022377899007515.

[42] R. Lehe et al. "Numerical growth of emittance in simulations of laser-wakefield acceleration". In: *Physical Review Special Topics - Accelerators and Beams* 16.2 (2013), pp. 1–8. ISSN: 10984402. DOI: 10.1103/PhysRevSTAB.16.021301.

[43] Simin Feng and Herbert G. Winful. "Physical origin of the Gouy phase shift". In: *Optics Letters* 26.8 (2001), p. 485. ISSN: 0146-9592. DOI: 10.1364/ol.26.000485.

[44] M. Gouy. "Sur La Propagation Anomale Des Ondes". In: *Annales de chimie et de physique* 6.24 (1891), p. 145.

[45] Selcuk Akturk et al. "The general theory of first-order spatio-temporal distortions of Gaussian pulses and beams". In: 13.21 (2005), pp. 1759–1763.

[46] A.E. Siegman. *Lasers*. University Science Books, 1986. ISBN: 9780935702118. URL: https://books.google.de/books?id=1BZVwUZLTkAC.

[47] A.G. Kostenbauder. "Ray-pulse matrices: a rational treatment for dispersive optical systems". In: *IEEE Journal of Quantum Electronics* 26.6 (June 1990), pp. 1148–1157. ISSN: 00189197. DOI: 10.1109/3.108113. URL: http://ieeexplore.ieee.org/document/108113/.

[48] H. Vincenti and F. Quéré. "Attosecond lighthouses: How to use spatiotemporally coupled light fields to generate isolated attosecond pulses". In: *Physical Review Letters* 108.11 (2012), pp. 1–5. ISSN: 00319007. DOI: 10.1103/PhysRevLett.108.113904.

[49] J.D. Jackson. *Classical Electrodynamics, Third Edition*. Wiley, 1999.

[50] S. G. Rykovanov et al. "Plasma surface dynamics and smoothing in the relativistic few-cycle regime". In: *New Journal of Physics* 13 (2011). ISSN: 13672630. DOI: 10.1088/1367-2630/13/2/023008. arXiv: 0908.3134.

[51] George D. Tsakiris et al. "Route to intense single attosecond pulses". In: *New Journal of Physics* 8.06 (2006), pp. 1–20. ISSN: 13672630. DOI: 10.1088/1367-2630/8/1/019.

[52] C. Thaury et al. "Plasma mirrors for ultrahigh-intensity optics". In: *Nature Physics* 3.6 (2007), pp. 424–429. ISSN: 17452481. DOI: 10.1038/nphys595.

[53] Daniel An Der Brügge and Alexander Pukhov. "Ultrashort focused electromagnetic pulses". In: *Physical Review E - Statistical, Nonlinear, and Soft Matter Physics* 79.1 (2009), pp. 1–5. ISSN: 15393755. DOI: 10.1103/PhysRevE.79.016603.

[54] B. Dromey et al. "Coherent synchrotron emission in transmission from ultrathin relativistic laser plasmas". In: *New Journal of Physics* 15 (2013). ISSN: 13672630. DOI: 10.1088/1367-2630/15/1/015025.

[55] F. Brunel. "Not-so-resonant, resonant absorption". In: *Physical Review Letters* 59.1 (July 1987), pp. 52–55. ISSN: 0031-9007. DOI: 10.1103/PhysRevLett.59.52. URL: https://link.aps.org/doi/10.1103/PhysRevLett.59.52.

[56] C. Thaury and F Quéré. "High-order harmonic and attosecond pulse generation on plasma mirrors: basic mechanisms". In: *Journal of Physics B: Atomic, Molecular and Optical Physics* 43.21 (2010), p. 213001. ISSN: 0953-4075. DOI: 10.1088/0953-4075/43/21/213001.

[57] U. Teubner and P. Gibbon. "High-order harmonics from laser-irradiated plasma surfaces". In: *Reviews of Modern Physics* 81.2 (2009), pp. 445–479. ISSN: 00346861. DOI: 10.1103/RevModPhys.81.445.

[58] S. Gordienko and A. Pukhov. "Scalings for ultrarelativistic laser plasmas and quasimonoenergetic electrons". In: *Physics of Plasmas* 12.4 (2005), pp. 1–11. ISSN: 1070664X. DOI: 10.1063/1.1884126.

[59] T. Baeva, S. Gordienko and A. Pukhov. "Theory of high-order harmonic generation in relativistic laser interaction with overdense plasma". In: *Physical Review E - Statistical, Nonlinear, and Soft Matter Physics* 74.4 (2006), pp. 1–11. ISSN: 15393755. DOI: 10.1103/PhysRevE.74.046404. arXiv: 0604228 [physics].

[60] M. Behmke et al. "Controlling the spacing of attosecond pulse trains from relativistic surface plasmas". In: *Physical Review Letters* 106.18 (2011), pp. 1–4. ISSN: 00319007. DOI: 10.1103/PhysRevLett.106.185002.

[61] M. Yeung et al. "Experimental observation of attosecond control over relativistic electron bunches with two-colour fields". In: *Nature Photonics* 11.1 (2017), pp. 32–35. ISSN: 17494893. DOI: 10.1038/nphoton.2016.239.

[62] Andrea Macchi, Marco Borghesi and Matteo Passoni. "Ion acceleration by superintense laser-plasma interaction". In: *Reviews of Modern Physics* 85.2 (May 2013), pp. 751–793. ISSN: 0034-6861. DOI: 10.1103/RevModPhys.85.751. URL: https://link.aps.org/doi/10.1103/RevModPhys.85.751.

[63] S. C. Wilks et al. "Absorption of ultra-intense laser pulses". In: *Physical Review Letters* 69.9 (1992), pp. 1383–1386. ISSN: 00319007. DOI: 10.1103/PhysRevLett.69.1383.

[64] H. Vincenti et al. "Optical properties of relativistic plasma mirrors". In: *Nature Communications* 5 (2014), pp. 1–9. ISSN: 20411723. DOI: 10.1038/ncomms4403. arXiv: 1312.1908.

[65] R. Hörlein et al. "Controlling the divergence of high harmonics from solid targets: A route toward coherent harmonic focusing". In: *European Physical Journal D* 55.2 (2009), pp. 475–481. ISSN: 14346060. DOI: 10.1140/epjd/e2009-00084-x.

[66] T. Baeva, S. Gordienko and A. Pukhov. "Relativistic plasma control for single attosecond x-ray burst generation". In: *Physical Review E* 74.6 (Dec. 2006), p. 065401. ISSN: 1539-3755. DOI: 10.1103/PhysRevE.74.065401. URL: https://link.aps.org/doi/10.1103/PhysRevE.74.065401.

[67] M. Yeung et al. "Dependence of laser-driven coherent synchrotron emission efficiency on pulse ellipticity and implications for polarization gating". In: *Physical Review Letters* 112.12 (2013), pp. 1–5. ISSN: 10797114. DOI: 10.1103/PhysRevLett.112.123902.

[68] P B Corkum, N H Burnett and M Y Ivanov. "Subfemtosecond pulses". In: *Optics Letters* 19.22 (Nov. 1994), p. 1870. ISSN: 0146-9592. DOI: 10.1364/OL.19.001870. URL: https://www.osapublishing.org/abstract.cfm?URI=ol-19-22-1870.

[69] Jonathan A. Wheeler et al. "Attosecond lighthouses from plasma mirrors". In: *Nature Photonics* 6.12 (2012), pp. 829–833. ISSN: 17494885. DOI: 10.1038/nphoton.2012.284.

[70] Olga Jahn et al. "Towards intense isolated attosecond pulses from relativistic surface high harmonics". In: *Optica* 6.3 (2019), p. 280. ISSN: 2334-2536. DOI: 10.1364/optica.6.000280. arXiv: 1808.01064.

[71] A. Baltuška et al. "Attosecond control of electronic processes by intense light fields". In: *Nature* 421.6923 (Feb. 2003), pp. 611–615. ISSN: 0028-0836. DOI: 10.1038/nature01414. URL: http://www.nature.com/articles/nature01414.

[72] M. Born et al. *Principles of Optics: Electromagnetic Theory of Propagation, Interference and Diffraction of Light*. Cambridge University Press, 1999. ISBN: 9781139643405.

[73] F. Quéré et al. "Phase properties of laser high-order harmonics generated on plasma mirrors". In: *Physical Review Letters* 100.9 (2008), pp. 1–4. ISSN: 00319007. DOI: 10.1103/PhysRevLett.100.095004.

[74] Alexander Blinne et al. "Efficient retrieval of phase information from real-valued electromagnetic field data". In: *Journal of Computational Physics: X* 1 (2019), p. 100019. ISSN: 25900552. DOI: 10.1016/j.jcpx.2019.100019. arXiv: 1801.04812. URL: https://doi.org/10.1016/j.jcpx.2019.100019.

[75] Paul Gibbon. "Harmonic generation by femtosecond laser-solid interaction: A Coherent "water-window" light source?" In: *Physical Review Letters* 76.1 (1996), pp. 50–53. ISSN: 10797114. DOI: 10.1103/PhysRevLett.76.50.

[76] Yu M Mikhailova, V T Platonenko and S G Rykovanov. "Generation of an attosecond X-ray pulse in a thin film irradiated by an ultrashort ultrarelativistic laser pulse". In: *Journal of Experimental and Theoretical Physics Letters* 81.11 (June 2005), pp. 571–574. ISSN: 0021-3640. DOI: 10.1134/1.2029946. URL: http://link.springer.com/10.1134/1.2029946.

[77] "Efficient picosecond x-ray pulse generation from plasmas in the radiation dominated regime". In: *Optica* 4.11 (Nov. 2017), p. 1344. ISSN: 2334-2536. DOI: 10.1364/OPTICA.4.001344. URL: https://www.osapublishing.org/abstract.cfm?URI=optica-4-11-1344.

[78] Matthew R. Edwards, Victor T. Platonenko and Julia M. Mikhailova. "Enhanced attosecond bursts of relativistic high-order harmonics driven by two-color fields". In: *Optics Letters* 39.24 (2014), p. 6823. ISSN: 0146-9592. DOI: 10.1364/ol.39.006823.

[79] Matthew R. Edwards and Julia M. Mikhailova. "Waveform-Controlled Relativistic High-Order-Harmonic Generation". In: *Physical Review Letters* 117.12 (2016), pp. 1–5. ISSN: 10797114. DOI: 10.1103/PhysRevLett.117.125001.

[80] Matthew R. Edwards and Julia M. Mikhailova. "Multipass relativistic high-order-harmonic generation for intense attosecond pulses". In: *Physical Review A* 93.2 (2016), pp. 1–5. ISSN: 24699934. DOI: 10.1103/PhysRevA.93.023836.

[81] A. Pukhov et al. "Relativistic high harmonics and (sub-)attosecond pulses: Relativistic spikes and relativistic mirror". In: *European Physical Journal D* 55.2 (2009), pp. 407–414. ISSN: 14346060. DOI: 10.1140/epjd/e2009-00187-4.

[82] C. Rödel et al. "Harmonic generation from relativistic plasma surfaces in ultrasteep plasma density gradients". In: *Physical Review Letters* 109.12 (2012), pp. 1–5. ISSN: 00319007. DOI: 10.1103/PhysRevLett.109.125002. arXiv: arXiv:1205.6821v1.

[83] A. Bourdier. "Oblique incidence of a strong electromagnetic wave on a cold inhomogeneous electron plasma. Relativistic effects". In: *Physics of Fluids* 26.7

(1983), pp. 1804–1807. ISSN: 10706631. DOI: 10.1063/1.864355. URL: https://aip.scitation.org/doi/10.1063/1.864355.

[84] M. J.V. Streeter et al. "Relativistic plasma surfaces as an efficient second harmonic generator". In: *New Journal of Physics* 13 (2011). ISSN: 13672630. DOI: 10.1088/1367-2630/13/2/023041.

[85] TOP500. *TOP500 List - November 2020 — TOP500*. 2020. URL: https://top500.org/lists/top500/list/2020/11/ (visited on 01/03/2021).

[86] M. Geissler et al. "3D simulations of surface harmonic generation with few-cycle laser pulses". In: *New Journal of Physics* 9 (2007). ISSN: 13672630. DOI: 10.1088/1367-2630/9/7/218.

[87] R. A. Snavely et al. "Intense high-energy proton beams from petawatt-laser irradiation of solids". In: *Physical Review Letters* 85.14 (2000), pp. 2945–2948. ISSN: 00319007. DOI: 10.1103/PhysRevLett.85.2945.

[88] E. L. Clark et al. "Measurements of energetic proton transport through magnetized plasma from intense laser interactions with solids". In: *Physical Review Letters* 84.4 (2000), pp. 670–673. ISSN: 10797114. DOI: 10.1103/PhysRevLett.84.670.

[89] E. L. Clark et al. "Energetic heavy-ion and proton generation from ultraintense laser-plasma interactions with solids". In: *Physical Review Letters* 85.8 (2000), pp. 1654–1657. ISSN: 00319007. DOI: 10.1103/PhysRevLett.85.1654.

[90] S. C. Wilks et al. "Energetic proton generation in ultra-intense laser-solid interactions". In: *Physics of Plasmas* 8.2 (2001), pp. 542–549. ISSN: 1070664X. DOI: 10.1063/1.1333697.

[91] W. L. Kruer and Kent Estabrook. "JXB heating by very intense laser light". In: *Physics of Fluids* 28.1 (1985), pp. 430–432. ISSN: 10706631. DOI: 10.1063/1.865171.

[92] Marco Hornung et al. "54 J pulses with 18 nm bandwidth from a diode-pumped chirped-pulse amplification laser system". In: *Optics Letters* 41.22 (2016), p. 5413. ISSN: 0146-9592. DOI: 10.1364/ol.41.005413.

C. Table of commonly used symbols

Parameter	Description
$a_0 = \dfrac{eE_0}{mc\omega_L}$	laser pulse intensity
τ	laser pulse duration
ω_L	central laser frequency
$\lambda_0 = \dfrac{2\pi c}{\omega_L}$	central laser wavelength
L_p	preplasma scale length
n_0	maximum bulk target density
$\omega_p = \sqrt{n_0}$	plasma frequency
$z_R = \pi w_0^2/\lambda_0$	Rayleigh length

Table C.1.: Laser and plasma parameters

D. Relativistic Units

Where it is stated explicitly, relativistic units are used. This means setting $m_e = c = e = 1$ and in particular:

- vector potential field amplitude: $a = \frac{eA}{m_e c}$,
- time: $t = \omega_L t'$,
- momentum: $p = \frac{p'}{m_e c}$,
- coordinate: $x = \frac{x'}{\lambda_L}$
- plasma density: $n = \frac{n'}{n_c}$.

The primed quantities are in SI units.

E. List of Publications

- S. Tietze, M. Zepf, S. G. Rykovanov and M. Yeung
  Propagation effects in multipass high harmonic generation from plasma surfaces
  In: New J. Phys. 22 093048 (2020)

- A. Blinne, S. Kuschel, S. Tietze, M. Zepf
  Efficient retrieval of phase information from real-valued electromagnetic field data
  In: Journal of Computational Physics: X 1 (2019) 100019, arXiv:1801.04812

- G.A. Becker, M.B. Schwab, R. Lötzsch, S. Tietze *et al.*
  Characterization of laser-driven proton acceleration from water microdroplets
  In: Sci Rep 9, 17169 (2019)

- G.A. Becker, S. Tietze, S. Keppler, J. Reislöhner *et al.*
  Ring-like spatial distribution of laser accelerated protons in the ultra-high-contrast TNSA-regime
  In: Plasma Phys. Control. Fusion 60 055010 (2018)

F. Ehrenwörtliche Erklärung

Ich erkläre hiermit ehrenwörtlich, dass ich die vorliegende Arbeit selbständig, ohne unzulässige Hilfe Dritter und ohne Benutzung anderer als der angegebenen Hilfsmittel und Literatur angefertigt habe. Die aus anderen Quellen direkt oder indirekt übernommenen Daten und Konzepte sind unter Angabe der Quelle gekennzeichnet.

Bei der Auswahl und Auswertung folgenden Materials haben mir die nachstehend aufgeführten Personen unentgeltlich geholfen:

1. Prof. Dr. Matt Zepf
2. Prof. Dr. S. G. Rykovanov
3. Dr. Mark Yeung

Weitere Personen waren an der inhaltlich-materiellen Erstellung der vorliegenden Arbeit nicht beteiligt. Insbesondere habe ich hierfür nicht die entgeltliche Hilfe von Vermittlungs- bzw. Beratungsdiensten (Promotionsberater oder andere Personen) in Anspruch genommen. Niemand hat von mir unmittelbar oder mittelbar geldwerte Leistungen für Arbeiten erhalten, die im Zusammenhang mit dem Inhalt der vorgelegten Dissertation stehen.

Die Arbeit wurde bisher weder im In- noch im Ausland in gleicher oder ähnlicher Form einer anderen Prüfungsbehörde vorgelegt.

Die geltende Promotionsordnung der Physikalisch-Astronomischen Fakultät ist mir bekannt.

Ich versichere ehrenwörtlich, dass ich nach bestem Wissen die reine Wahrheit gesagt und nichts verschwiegen habe.

Ort, Datum Unterschrift d. Verfassers

G. Acknowledgements

First and foremost, I would like to thank my supervisors Prof. Dr. Matt Zepf and Prof. Dr. Sergey Rykovanov for offering me to write my thesis in their workgroup. Without their knowledge, insight and helpful discussion this thesis would not have been possible.
I would like to thank the whole workgroup for enriching discussions and insightful seminars over the past 5 years.
Furthermore, I would like to thank Prof. Dr. Matt Zepf and Dr. Mark Yeung for making my stay at the Queen's University Belfast possible. I will never forget your hospitality and patience in explaining the Irish culture to me!
Special thanks go to my colleagues and former colleagues Andreas, Dominik, Carola, Alex, Stephan, Felipe, Harsh, David and Vasily. Without you, my time as a PhD student wouldn't have been nearly as much fun!
Even more special thanks go to my girlfriend Christin, who supported me especially during the last stages of my thesis.
Last but not least I would like to thank my parents for their everlasting support during the entire time of my studies. Danke Mama und Papa!